The chemical composition of solar-type stars and its impact on the presence of planets

Patrick Baumann

München 2013

The chemical composition of solar-type stars and its impact on the presence of planets

Patrick Baumann

Dissertation

der Fakultät für Physik
der Ludwig-Maximilians-Universität
München

durchgeführt am
Max-Planck-Institut für Astrophysik

vorgelegt von
Patrick Baumann
aus München

München, den 31. Januar 2013

Erstgutacher: Prof. Dr. Achim Weiss
Zweitgutachter: Prof. Dr. Joachim Puls
Tag der mündlichen Prüfung: 8. April 2013

Zusammenfassung

Wir untersuchen eine mögliche Verbindung zwischen den relativen Elementhäufigkeiten in Sternatmosphären und der Anwesenheit von Planeten um den jeweiligen Stern. Um zuverlässige Ergebnisse zu erhalten, untersuchen wir ausschließlich sonnenähnliche Sterne und führen unsere spektroskopischen Analysen zur Bestimmung der grundlegenden Parameter und der chemischen Zusammensetzung streng differenziell und relativ zu den solaren Werten durch. Insgesamt untersuchen wir 200 Sterne unter Zuhilfenahme von Spektren mit herausragender Qualität, die an den modernsten Teleskopen gewonnen wurden, die uns zur Verfügung stehen.

Mithilfe der Daten für 117 sonnenähnliche Sterne untersuchen wir eine mögliche Verbindung zwischen der Oberflächenhäufigkeit von Lithium in einem Stern, seinem Alter und der Wahrscheinlichkeit, dass sich ein oder mehrere Sterne in einer Umlaufbahn um das Objekt befinden. Für jeden Stern erhalten wir sehr exakte grundlegende Parameter unter Benutzung einer sorgfältig zusammengestellten Liste von Fe I- und Fe II-absorptionslinien, modernen Modellatmosphären und Routinen zum Erstellen von Modellspektren. Die Massen und das Alter der Objekte werden mithilfe von Isochronen bestimmt, was zu sehr soliden relativen Werten führt. Bei jungen Sternen, für die die Isochronenmethode recht unzuverlssig ist, vergleichen wir verschiedene alternative Methoden. Die Lithiumhäufigkeiten erhalten wir, indem wir die das Absorptionsdoublet mit einer Wellenlänge von 6708 Å synthetisieren. Aufgrund unserer Ergebnisse können wir einen Zusammenhang zwischen Lithiumhäufigkeit und der Anwesenheit von Planeten ausschließen. Auf der anderen Seite können wir zeigen, dass frühere Ergebnisse, die eben einen solchen Zusammenhang nahelegten, auf systematischen Fehlern bei der Auswahl der Objekte basier-

ten.

Um das Auftreten einiger Objekte mit überraschend hohen Lithiumhäufigkeiten in der ersten Objektgruppe zu untersuchen, werten wir die Daten für 76 weiterentwickelte Sterne aus. Hierbei benutzen wir dieselben Methoden wie im ersten Teil. Wir zeigen, dass die meisten Sterne dieser Gruppe tatsächlich Sterne sind, die die Hauptreihe verlassen haben, und dass ihre durchschnittliche Lithiumhäufigkeit deutlich höher ist als bei Hauptreihensternen. Allerdings kann über den Grund für diesen Anstieg bisher nur spekuliert werden, wir stellen aber mögliche Erklärungen vor.

Als Testfall für größere Datenmengen untersuchen wir Temperaturabhängige Trends in der Elementverteilung von α Centauri A. Wir untersuchen die Häufigkeiten von 20 chemischen Elementen in seiner Photosphäre auf der Basis mehrerer sehr hochwertiger optischer Spektren. Laut neuerer Veröffentlichungen könnte ein Fehlen von Elementen mit hohen Kondensationstemeraturen im Vergleich zu flüchtigen ein Hinweis auf Gesteinsplaneten sein. α Centauri A zeigt tatsächlich einen noch stärkeren Abfall an Häufigkeiten mit steigender Kondensationstemperatur als die Sonne, weswegen wir α Centauri A als heißen Kandidaten auf der Suche nach erdähnlichen Exoplaneten sehen.

Abstract

We illuminate the connection between the chemical abundance ratios in stellar atmospheres and the presence of planets around the respective stars. In order to obtain reliable results, we consider only solar-type stars and conduct spectroscopic parameter and abundance analyzes in a strictly differential way relative to the Sun. Altogether, we examine exceptionally high quality spectra for almost 200 stars obtained with the most sophisticated telescopes available to us.

The first sample of 117 solar analogs is used to examine a possible connection between the surface lithium abundance of a star, its age, and its likelihood to host a planet. We determine very precise fundamental stellar parameters for each star using a carefully chosen set of Fe I and Fe II lines, up-to-date and well-tested model atmospheres, and state-of-the-art spectrum modeling routines. Masses and ages of the objects are determined using isochrone fits of the stellar parameters, resulting in solid relative parameters. For young stars, were isochrone ages are unreliable, we compare different alternative techniques. Lithium abundances are gained from spectral line synthesis of the lithium doublet at 6708 Å. Based on our results, a correlation between lithium abundance and the presence of planets can be ruled out, while it can be shown, that earlier findings indicating such a connection are based on selection biases.

To confirm the occurrence of some high-lithium subgiants detected in the solar analogs sample, we analyze a set of 76 evolved stars in the next step using the same techniques as before. We show, that most of the stars picked for this analysis really have evolved from the main sequence, and that their average lithium abundance is distinctly higher than in the main sequence case. The reason for this increase

remains to be discussed, possible explanations are presented in the work.

As a testing scenario for larger samples, we explore the condensation temperature trend in α Centauri A. In a very carefull analysis using different high-quality spectra for α Centauri A and the Sun, we determine abundances for 20 elements in the object's photosphere. It has been suggested, that an underabundance in refractory elements relative to volatiles could be an indicator for the presence of rocky planets. α Centauri A does show an even stronger underabundance than the Sun, which is why we conclude that α Centauri A is a hot candidate in the search for extrasolar planets.

Contents

1 Introduction **1**

1.1 Stellar chemical composition 3

1.1.1 Notation and units 3

1.1.2 The Sun 4

1.1.3 The solar neighborhood 5

1.1.4 Stellar composition and planet hosting 8

1.2 Lithium in the universe 12

1.2.1 The origins of lithium 12

1.2.2 The Spite plateau and the lithium dip 13

1.2.3 Lithium depletion in stellar evolution models 16

1.2.4 Lithium and planets 19

2 Data and Reduction **23**

2.1 Observation 24

2.2 Data reduction 27

3 Analysis **31**

3.1 Stellar spectroscopy 31

3.1.1 Line broadening 33

3.1.2 Atomic data 34

3.2 Model atmospheres 35
3.3 The fundamental parameters 36
3.3.1 Equivalent widths 36
3.3.2 Fundamental parameters from equilibria 37
3.3.3 Ages and Masses 41
3.4 Elemental abundances 44
3.5 The photospheric lithium abundance 45

4 Lithium in solar-type stars **51**
4.1 Lithium and ages 53
4.2 Lithium in planet hosts 56

5 Lithium in subgiants **65**
5.1 Sample selection and analysis 67
5.2 Results 73

6 α Centauri A **79**
6.1 Data and analysis 80
6.2 The condensation temperature trends 89
6.3 Discussion 91

7 Summary and conclusions **95**

A Tables **99**
A.1 Solar Twins 99
A.2 Subgiants 103
A.3 α Centauri A 106

List of Figures

1-1 Average chemical abundances for 64 solar analogs. 10

1-2 Model predictions for lithium depletion. 17

1-3 Lithium in planet hosts and field stars, data from Israelian et al. (2009, [76]). 20

2-1 Example for an image produced by the MIKE spectrograph. 27

2-2 Detail of the plotted spectra for HIP117320. 28

3-1 Snapshot from the parameter determination process. 38

3-2 $\log g$ vs. T_{eff} with overplotted evolutionary tracks. 41

3-3 Synthetic spectra for 4 different objects. 47

4-1 $\log \epsilon_{Li}$ versus age for all stars in the solar analogs sample. 52

4-2 $\log \epsilon_{Li}$ versus age for our solar analogs sample and the objects from [76]. 57

4-3 $\log \epsilon_{Li}$ versus $\log g$ for our solar analogs sample and the objects from [76]. 60

4-4 $\log \epsilon_{Li}$ versus T_{eff} for the I09 sample. Full sample and 2-σ comparison group. 63

5-1 The subgiants sample in the lithium-metallicity plane. 65

5-2 Different mass cuts for our solar analogs and the I09 sample. 66
5-3 The lithium doublet in 2 example spectra. 68
5-4 Visualization of the determination of evolutionary state for 2 objects. 70
5-5 Evolutionary tracks for different masses and metallicities. 71
5-6 $\log \epsilon_{Li}$ versus age for our solar analogs, the I09 objects, and our subgiants. 72
5-7 $\log \epsilon_{Li}$ versus $\log g$ for our solar analogs, the I09 objects, and our subgiants. 75
5-8 Different mass cuts for the combined samples. 77

6-1 Fitting of the Hα line wings for α Centauri A. 83
6-2 Photospheric elemental abundance versus respective condensation temperature for the MIKE and HARPS spectra of α Centauri A. . . 89
6-3 Chemical abundance versus T_{cond} including the M09 results. 90
6-4 Chemical abundance versus T_{cond} for α Centauri A and B, from [124]. 93

List of Tables

1.1 The fundamental parameters for the Sun, from [13]. 5

1.2 Elements covered in [96] and [131] and the corresponding condensation temperatures. 11

2.1 Instruments used for data acquisition for this work. 25

2.2 Excerpt from the MIKE observing log from June 24, 2011 26

2.3 Detail of the spectral data for HIP117320. 30

3.1 Iron lines used for the determination of the fundamental parameters. 37

3.2 Line list for the synthesis of the lithium doublet at 6707.8 Å. 46

4.1 Parameters for solar twins in open cluster 54

4.2 Ages, masses, and log $\epsilon_{Li}$for the outliers in Figures 4-2 and 4-3 . . . 61

5.1 The fundamental parameters for HIP49024, the only object being part of both the MIKE and the UVES sample. 73

6.1 Basic parameters for α Centauri A from selected publications 82

6.2 Fundamental parameters for α Centauri A obtained in this work . . 83

6.3 Corrections for galactic chemical evolution applied to the abundances obtained for α Centauri A. 86

6.4 Abundances obtained for α Centauri A from the MIKE and HARPS data. N_{lines} gives the number of lines used for the respective abundance. 87
6.5 Abundances obtained for α Centauri A from Meléndez et al. (2009, [96], M09). The last column gives the average of the M09 and our MIKE and HARPS results. 88
6.6 Fundamental parameters for α Centauri A and α Centauri B, from Porto de Mello (2008, [124]). 91
6.7 Abundances for α Centauri A and α Centauri B, from Porto de Mello et al. (2008, [124]). 92

A.1 Specifications for the different samples 100
A.2 Sample used in I09. Masses and ages are from this work. 102
A.3 Specifications for the subgiants 104
A.4 Linelist used for the analysis of the α Centauri A HARPS and MIKE data 107

Chapter 1

Introduction

The search for planets outside our own solar system has become one of the most exciting fields in astronomy during the last two decades. After the first detection of an extrasolar planet in 1992 (PSR 1257+12 b) and the first one around a solar-type star in 1995 (51 Pegasi b, [94]), the number of confirmed planet detections has grown at a pace that was unimaginable in the early 1990s. Missions like Spitzer, Corot, and especially Kepler helped to increase the number of confirmed exoplanets to more than 850[1] and over 2000 candidates. Naturally, the detection of terrestrial planets is of special interest, and indeed it looks like a large number of planets we find out there are Earth-like: 351 out of 2740 planet candidates detected with Kepler appear to have a radius of less than 1.25 Earth radii, another 816 candidates have a radius between 1.25 and 2 Earth radii. With the means of modern telescopes, it is even possible to study the atmospheres of exoplanets regarding molecular lines, day-night temperature differences, and vertical temperature gradients. So far, this is only possible for hot Jupiters, but with the launch of the *James Webb Space Telescope* in 2014, observers hope to be able to examine even super Earths. For

[1] Status in January 2013, see, e.g., http://exoplanet.eu/catalog/

a roundup of the achievements in this field and a theoretical outlook on the next years, see, e.g., S. Seager (2011, [153]).

Planet search is usually conducted using two different methods, the radial velocity method and the transit one. In the radial velocity method, displacements of a star's spectral lines are observed. This effect is caused by the star's motion around the common center of mass of the star-planet system and the resulting Doppler shift in the stellar spectral lines. If the exoplanet system plane lies on the observer's line of sight, the transit method can be applied, were periodical luminosity changes of a star are measured. While the first method can be used to obtain a planet's mass, the second one provides its radius via the amount of luminosity reduction during the transit. Other common methods are microlensing, where the influence of a planet on the gravitational lensing effect of its host star is measured, and pulsar timing, that lead to the first discovery of an exoplanet in 1992. With the pulsar timing method, observers examine small variations in the extremely periodic radio emission pattern of a star, that are caused by planets. However, all of the mentioned methods for planet detection are sumptuous and time consuming.

During the last years, however, several groups have come up with suggestions on techniques that would allow to select certain objects of interest in advance instead of just following a group of stars with sufficient brightness over a longer period of time. One of these ideas is the trace a planet will leave in the composition of its host star: since both planet and host are formed from the same material and the composition of a planet can be very different from that of its host star, a planet host might look different in terms of elemental abundances when compared to similar stars without planets. Finding a certain abundance pattern in a star via spectroscopic analysis would then indicate a promising candidate for an extrasolar planet host. This method depends strongly on the composition of the possible plan-

ets, since rocky planets could leave a strong imprint in the host's abundance ratios while gas giants might be chemically similar enough to the host not to be detected this way. That means, that the abundance pattern method would fit best for the search for terrestrial planets.

1.1 Stellar chemical composition

We are able to determine the chemical composition of stars by spectroscopic analyses. This is possible, because elements in the photospheres of cool, solar-type stars are, in general, neutral or only lightly ionized and therefore the cooler outer layers are able to absorb photons of a specific energy coming from the hotter inner layers and re-emit them in random directions. That causes absorption lines in the (otherwise uniform) stellar spectra that can be attributed to certain elements.

By measuring the strength of an absorption line, we can determine the abundance of the element that is producing that line. Important for a reliable determination is a realistic model for line formation in the photosphere, which depends strongly on the temperature, the pressure, and the density in the region of line formation. Hence before being able to determine chemical abundances of a star, we need to know its fundamental parameters. The details of parameter and abundance determination are explained in Chapter 3.

1.1.1 Notation and units

Throughout this work, we use the following standard notations for abundances:

The logarithmic abundance of an element relative to hydrogen is defined as $\log \epsilon_X \equiv \log \frac{n_X}{n_H} + 12$, where n_X and n_H are the number densities of element X and hydrogen, respectively. In this notation, the number density of hydrogen in an

arbitrary volume is defined to be 10^{12}, or 12 dex.

[X/H] gives the abundance of element X relative to the solar value, which defines the Sun's abundances to be 0 for all elements: $[X/H] \equiv \log \epsilon_X - \log \epsilon_X^{\odot}$ with $\odot$ marking the solar value. From this definition follows [X/Y] = [X/H] - [Y/H]. The iron abundance [Fe/H] is often used as an approximation for the overall metallicity in a star.

It is common to use the unit *dex* in this context to account for logarithmic values. Since we use the logarithm to base ten, one dex stands for one order of magnitude.

1.1.2 The Sun

The chemical composition of the Sun is of fundamental importance, mostly because the extraordinary high accuracy that can be achieved here. This precision makes it possible to understand the processes in stellar interiors, but also to use the Sun as the most important reference standard for elemental analyses in other objects. Obviously, the solar chemical composition has been an object of interest for a very long time.

First attempts to compile a complete catalog of solar abundances were made in the 20s and 30s of the last century by Russel (1929, [141]) and Goldschmidt (1938, [62]). Those early works already showed the same overall picture we see today: a dominant amount of hydrogen and helium, lower abundances with larger atomic numbers, a peak in iron, and comparably low amounts of lithium and beryllium. Two different approaches to the solar composition were applied in those works, that are still used today: mass spectrometry from meteoritic material and spectroscopy. A special class of meteorites, the CI carbonaceous chondrites, were formed from the same material as the rest of the solar system and therefore, since they are largely unaffected by physical and chemical processes, they exhibit the primordial compo-

sition of the Sun to a great extent (10 to 20 % for most elements, which is well within the uncertainties of the analysis). An exceptional case are volatile elements, such as hydrogen, helium carbon, nitrogen, and oxygen, that are depleted compared to the primordial value. Also lithium and beryllium show a different abundance in the photospheric analyses due to depletion in the Sun; the reason for this in the resulting consequences will be discussed in detail in Section 1.2. Apart from those elements, that have varied over the course of the last 4.5 Gyr since the formation of the solar system, the photospheric abundances gained from spectral analyses and the values from meteorites show an excellent agreement in younger studies.

Since these first achievements, frequent publications marked an ever better knowledge about the solar abundances (e.g., [61, 171, 6, 70, 89]). An extensive, up-to-date atlas of the solar abundances from both meteoritic and photospheric analyses is presented in Asplund et al. (2009, [8]). They give the solar values with a remarkable precision in the order of 0.01 to 0.1 dex.

For further reference, we give the fundamental solar parameters in Table 1.1:

T_{eff}(K)	log g	[Fe/H]	log ϵ_{Li}	Age (Gyr)	Mass ($M_\odot$)
5777	4.44	0.00	1.07	4.5	1.00

Table 1.1: The fundamental parameters for the Sun, from [13].

1.1.3 The solar neighborhood

Naturally, also the chemical compositions of other stars has been examined as soon as reasonably good data were available. Nearby stars are popular targets because of their brightness, which enables very high quality data, but also for reasons like the negligible reddening and the possibility to measure their trigonometric parallaxes very precisely. Solar-type stars on the other hand are of special interest in abundance determination works, because the influence of the atmospheric param-

eters is well known in the Sun, and therefore the derived values can be calibrated relatively easily using the solar results. Solar-type stars are stars with fundamental parameters very similar to solar, resulting in stars of spectral class late F to early K ([96]). Solar twins on the other hand are stars that are almost identical to the Sun, with very small allowed deviations in fundamental parameters resulting in spectral classes between G0 and G5. Important steps towards identifying solar twins have been made by Porto de Mello & da Silva (1997, [123]), Soubiran (2004, [163]), King et al. (2005, [79]), and Meléndez & Ramírez ([100, 101]).

Abundance ratios are, for example, an important tool in the modeling of theories of galaxy formation. It is possible to identify two main populations in the galactic disk of the Milky Way, an old, thick disk that formed within a relatively short period of time ($\sim 10^9$ years, or 1 Gyr), and a younger, thin disk, that took somewhat longer to form. The thin and thick disk do not only differ in galactic velocity components (by which they are usually defined), but also in their chemical composition (e.g., [115, 136, 129, 15]). Also for the galactic halo, two separate populations seem to exist, that differ in their α/Fe ratio[2] and seem to originate in different places (e.g., [117]). The production sites of certain elements (e.g. r- and s-processes) are used as indicators for the origins of different populations (e.g., [16]). Accordingly, most of the stars in the solar neighborhood are thin disk stars, thick disk and halo stars only have a share of about 10 %. For a very detailed summary on that topic, see the extensive article by P. E. Nissen (2011, [116]).

An important topic that is examined with the means of spectroscopic abundance analysis is galactic chemical evolution (GCE). Edvardsson et al. (1993, [49]) have shown, that even in nearby, solar-type stars, chemical evolution has taken place, that means, the abundance ratios in younger stars differ from those in older ones. This finding has since been explained by theoretical models (e.g., [181, 80]). The

[2] α stands for the average of the so-called α-elements O, Mg, Si, S, Ca, and Ti.

interstellar medium (ISM) is being enriched in iron and α elements by the ejecta of stars and supernovae (SN). The resulting change in the matter, that serves as raw material for new stars, leads to an increase of those elements in younger stars compared to ones that have formed at an earlier stage. Iron is therefore a widely used trace for ages in larger samples, so the patterns of other elements are often represented with their [X/Fe] versus [Fe/H] trend.

For broader parameter ranges (especially in metallicity) of samples, chemical evolution corrections become extremely important, since GCE effects show a strong impact on the results. The common procedure for GCE corrections is to fit the upper envelope of the [X/Fe] versus [Fe/H] plots for each elements and use it to define the growth of elemental abundance with metallicity. This trend has to be compared with galactic chemical evolution models such as [95, 183] and observational trends (e.g., [16, 136, 175, 114, 131]) to clarify whether the sample follows the expected evolutionary trend or if certain deviations are caused by other sources.

Through the [X/Fe] ratios and trends with [Fe/H], we can also gather information about the frequency of the sources that produce those elements. The main distributors of heavier elements are supernovae (SNe). The two most important types, SNe type Ia and type II, show quite different typical signatures. Type Ia supernovae are the result of white dwarfs in close binaries, that accrete material form their companion until their core reaches a critical mass, leading to a thermonuclear explosion. Those SNe Ia produce large amounts of iron, but only little α elements. SNe II on the other hand result from a core collapse in massive stars ($M_{core} > 8M_{\odot}$). They produce more α elements relative to iron compared to the solar values ([α/Fe] > 0, e.g., [131]). That leads, for example, to a decreasing [α/Fe] ratio for younger stars in the galactic disk, because of the increasing share of SNe Ia relative to SNe II in the enrichment of the interstellar medium.

For details on the more scarce special types of supernovae such as the extremely luminous type Ic or hypernovae and their impact on the ISM, see, e.g., Nomoto et al. (2010, [118]).

1.1.4 Stellar composition and planet hosting

But not only the region or epoch a star was formed in or the physics inside it have an impact on the composition of a star. Also the possible companions that may have formed from the same material, such as companions in binary systems or planets around the star, may change certain elemental abundances.

According to the Solar Nebular Disk Model ([188]), the most widely accepted model for the formation of stellar systems, planets form a very short time after their host stars from the so-called proto-planetary disk surrounding the protostar. This disk consists of the remnants of the collapsing cloud the star itself formed from and continues to feed its material to the star. In the disk, formation of dust grains may occur. Those grains made of rock and ice are the seeds for planetesimals. If the disk contains enough material, and the object's orbit around the host star is not obstructed, those planetesimals continue to accrete mass and eventually form planets. Those processes are thought to take place on timescales of some 100 million years. In case of a successful planet formation, the material locked up in the planets will not end up in the stellar interior (as long as the planetary orbit is stable and the planet does not eventually fall into the host star), so if the chemical compositions of the planets differ from that of the host, the abundance ratios in the star should be different from the original composition.

The formation of rocky planets takes place in the inner part of the protoplanetary disk, where temperatures are high enough to prevent water and other volatile elements from condensing, so purely rocky material is allowed to consolidate and

later form planetesimals. Following this theory, rocky planets are formed without the inclusion of water or any other volatile elements. Those materials are thought to have arrived on the terrestrial planets in a later phase through meteorite or planetesimal impacts.

This model can also explain, why gas giants are thought to have a composition very similar to their host stars, since they are formed in the outer regions of the protoplanetary disk, where temperatures are low enough for all elements to condensate and form dust grains.

For a detailed analysis of today's understanding of these processes, see, e.g., Montmerle et al. (2006, [111]) and references therein.

Inferences about impacts of those formation processes on the chemical composition of planet host stars have been difficult to draw, since reasonable numbers of planet hosts only became available during the last couple of years. Since the reports about the first exoplanets, however, it has been tried to examine possible differences between planet hosts and field stars.

Also the question whether the Sun is a typical example of a planet hosts is of crucial importance ([152]) for candidate gathering. This question has been answered positively in many studies until recently (e.g., [138, 72, 139]). However typical the Sun may bee, there are systematic differences to average field stars on small scales.

In 1997, Gonzalez ([63]) published a paper showing that planet hosts are, in general, more metal rich than comparison field stars for which no planets had been detected. Even though his analysis was based on very small numbers due to the fact that planet discoveries had just started, and the planets detected up to this date were giants, the results started an intense and still ongoing discussion. Several publications have strengthened theses findings (e.g., [67, 143, 73, 146, 54]), so that this systematic trend is generally accepted today. Some time later, Melendéz et al.

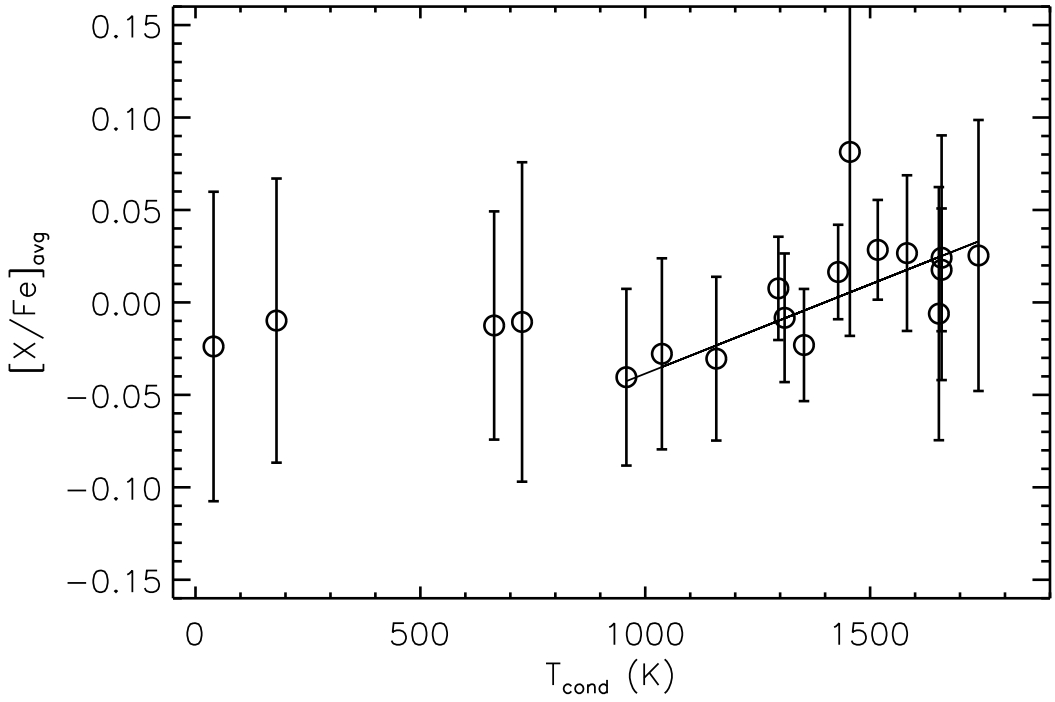

Figure 1-1: Average chemical abundances for 64 solar analogs relative to solar. Plotted is each elements mean abundance and error versus its condensation temperature. Data from [131].

(2009, [96]) presented a systematic analysis of 21 solar twins. They found, that the Sun shows a very peculiar abundance pattern: refractory elements in the Sun, which they define as chemical elements with a condensation temperature of about 900 K or higher, are depleted by about 20% relative to the volatile elements with respect to the field stars. The authors also showed, that the relative depletion grows with increasing condensation temperature of the element. In the same year, Ramirez et al. ([131]) confirmed those findings in a different sample of 64 stars impressively. Figure 1-1 shows this articulate trend: plotted are the averaged abundances for all 64 solar analogs in [131] relative to the solar values against the respective condensation temperatures. The solid line is the slope of $\sim 0.1 \frac{dex}{1000K}$ for refractory elements. Note that for 4 objects, Cu abundances (T_{cond} = 1037 K) were not taken into account

Atomic number	Name	T_{cond} in K
6	C	40
8	O	180
11	Na	958
12	Mg	1336
13	Al	1653
14	Si	1310
16	S	664
19	K	1006
20	Ca	1517
21	Sc	1659
22	Ti	1582
23	V	1429
24	Cr	1296
25	Mn	1158
27	Co	1352
28	Ni	1353
29	Cu	1037
30	Zn	726
31	Y	1659
32	Zr	1741
33	Ba	1455

Table 1.2: Elements covered in [96] and [131] and the corresponding condensation temperatures.

for this plot, since their values are extremely high and most likely overestimated. Also the mean barium abundance (T_{cond} = 1455 K) is unusually high due to a large scatter and a high number of objects with a Ba abundance greater than 0.1 dex (see Figure 1 in [131]). The condensation temperatures used in the plot are given in Table 1.2. They were taken from K. Lodders (2003, [88]).

The presented peculiarity shows that the Sun is, on closer contemplation, not a typical solar-type star. The shown deviation from the average can be interpreted as an evidence for terrestrial planet hosting. As described before, refractory elements

in the cooling protoplanetary disk will be the first to condensate and form dust. Those grains are the seeds for the formation of planets, hence a large amount of refractories will be locked up in the interior of planets. In most solar-type field stars, those refractory elements end up in the star together with the volatile ones, since the majority does not seem to have formed rocky planets. This means that a host star will be deficient in high condensation temperature elements compared to volatile ones. The rocky planets in the solar system are already sufficient to explain the deficiency of refractory elements. Even though gas giants make the biggest contribution to the mass bound in planets around the Sun, the composition of gas giants is very similar to the solar one, and therefore, the formation of gas giants does not influence the composition of the host star significantly. For an in-detail discussion, see [132].

Note that Gonzalez Hernandez et al. (2010, [68]), who compared a sample 24 solar-type planet hosts with 71 field stars, do not see a different behavior in condensation temperatures between the two sub-samples. However, this could possibly be caused by an inhomogeneous sample selection.

1.2 Lithium in the universe

1.2.1 The origins of lithium

Lithium is a very intriguing element to study, because it is subject to a variety of processes that both produce and destroy lithium with a very high sensitivity to environmental parameters. It is one of the few elements that were produced in the primordial nucleosynthesis (BBN) in the seconds after the Big Bang together with helium and beryllium. Already its primordial value has been highly debated for a long time. The production mechanisms of lithium in the BBN are

well known: the beryllium produced in the ^{3}He$(\alpha/\gamma)^7$Be reaction largely decays via ^{7}Be$(n, p)^7$Li, which is followed by lithium destruction via the proton capture reaction ^{7}Li$(p, \alpha)^4$He. Lithium destruction fades out with falling temperatures and decreasing proton densities. The amount of ^{6}Li produced via electron capture reactions from ^{6}He is very small: ^{6}Li/^{7}Li $\leq 10^{-4}$.

A crucial factor in this reaction network is the baryon[3] to photon ration, η. It determines the length of the so-called deuterium bottleneck, i.e., the time, in which deuterium can be effectively produced in $p + n$ reactions. The bottleneck is limited on the hot end by the density of high energy photons, that are able to destroy deuterium (the binding energy of deuterium is $B_d = 2.22$ MeV ([108])) and on the cooler end by the amount of free neutrons, that decay with a half-life of (880 ± 1) s ([18]). The amount of deuterium on the other hand is crucial for the rest of the BBN, and especially for the production of ^{3}He, that is needed for lithium production.

1.2.2 The Spite plateau and the lithium dip

Historically, the primordial lithium abundance had to be determined by extrapolating results from spectroscopic analyses in metal-poor population III stars to primordial metallicities ([169]). In addition to the uncertainties caused by the observations and the extrapolation, the obtained values also include the primordial ^{7}Be abundances, since ^{7}Be decays to ^{7}Li with a half life of 53 days[4].

A value for the primordial lithium abundance can also be obtained analytically, but calculations depend on a number of uncertain parameters, especially η. In 2003, observations from the Wilkinson Microwave Anisotropy Probe (*WMAP*) have put an end to those uncertainties by defining a precise baryon to photon ratio for the time of the Big Bang nucleosynthesis. This allows BBN models to deter-

[3] Baryons are particles consisting of 3 quarks. In this case, only protons and neutrons are relevant.
[4] from the Particle Data Group, [5], data available at http://pdg.lbl.gov/

mine the primordial lithium abundance with a very high accuracy to be $\log \epsilon_{Li}$= 2.70 ± 0.06 [149, 170, 36].

This highly precise value however conflicts with observations: since the 1980s, an almost universally constant lithium abundance was found in old, metal-poor dwarf stars, and later confirmed by several groups, the so-called *Spite plateau* [166, 167, 170]. This plateau shows a value for $\log \epsilon_{Li}$ of around 2.2, which is distinctly lower than the value predicted by BBN models (see, e.g., Fig. 3 in [170]). This discrepancy is known as the primordial, or cosmological, lithium problem, for which three solutions are being discussed: either even the oldest, most metal poor stars on the Spite plateau, that come closest to primordial abundances, have depleted their surface lithium abundance uniformly by 0.5 dex (more than a factor of 3), or the beryllium decay into ^{7}Li, though based on experimentally well tested cross-sections, could be considerably larger through resonant reactions, or the standard BBN models might be incomplete and therefore need enhancement through new physics, i.e., non-standard particle physics and cosmology such as decaying super-symmetric particles. Those additional physics, however, have to leave the amounts of hydrogen and helium unaltered, since the analytical predictions for those values agree extremely well with observations. For a comprehensive summary on the primordial lithium problem and its possible solutions, see Fields (2011, [53]) and references given therein.

For metallicities larger than -1.4 dex, the lithium abundances start to deviate from the plateau value. The upper envelope of the distribution starts to grow, until it reaches its maximum of around 3.3 at solar metallicity. At the same time, the abundance spread increases from an almost nonexistent dispersion to the full range between the upper envelope and zero ([84, 33]). Measurements of lithium in meteorites indicate an lithium abundance in the interstellar medium at the time of the

formation of the solar system of 3.26 ± 0.05 dex ([8], see also [109]), which is 3.6 times larger than the primordial prediction using the η obtained with *WMAP*, and more than 10 times the spite plateau value. Also in young open clusters with ages up to 100 Myr, surface lithium abundances between 3.0 and 3.2 dex are determined ([85] show a compilation of results from different sources). That means, that independent of the primordial value, lithium is also being created after the BBN. Three main locations are of importance here: the inter-stellar medium (ISM), carbon-rich stars, and supernovae. In the ISM, galactic cosmic ray particles interact with the medium and lead to spallation processes, that also produce lithium. Type II supernovae can also contribute to lithium production via spallation, in this case induced by the huge neutrino fluxes that occur here. This mechanism produces mainly ^{7}Li and ^{11}B. In nova outbursts, large amounts of ^{7}Be are produced during the thermonuclear explosion, which than decays into ^{7}Li with the abovementioned half-life of 53 days. While the lithium production in type II supernovae and novae is only theoretically described, carbon-rich stars are the only proven stellar source of lithium. Carbon-rich (C) stars have a photospheric C/O ratio greater than 1 and are seen to be lithium-rich. The production mechanism in those stars, however, is not well understood. For more details on lithium production and evolution, see, e.g., [3, 126]. Travaglio et al. (2001, [183]) give an extensive subsumption on the contributions of different sources of lithium production.

Another problem arising from observations is the so-called lithium dip. It was first detected by Wallerstein et al. (1965, [186]), and later confirmed in various studies (see, e.g., [20, 9]). The dip is a massive lithium depletion by up to 2.5 dex compared to neighboring (hotter and cooler) stars, that occurs in stars with effective temperatures of 6650 ± 150 K in field stars and open clusters. The fact that the dip is visible in young cluster such as the Hyades is a hint that the processes responsible

for this depletion work on rather short timescales. On the other hand, the depletion can not be confirmed in the Pleiades, a very young cluster (100 Myr, [104]), which indicates that the depletion has to take place in the main sequence phase rather than before. This is also supported by more recent findings by [85] and [10]. Even though the existence of the dip is very clearly proven, the physical reasons behind it are still far from being understood. Stellar evolution models (e.g., [178]) are, however, able to reproduce the dip based on the observational regularities.

However, since the lithium dip occurs at temperatures above 6500 K, it does not affect our work based on solar-type stars.

1.2.3 Lithium depletion in stellar evolution models

In the interior of main sequence stars, lithium is only being depleted. The destruction of lithium via proton-capture reactions (^{7}Li$(p,\alpha)^4$He) takes place at relatively low temperatures of around 2.5 million K at the pressures and densities we find in the particular regions inside solar-type stars ([121]). However, those temperatures occur only below the bottom of the convective zone in solar-type stars.

That means, without extra mixing, no lithium destruction can occur during the main sequence. Already in 1926, A. S. Eddington realized that mixing had to occur in the radiation zone as well in order to keep heavier elements from gravitational settling ([47]). He also suggested rotation-induced meridional circulation as the mechanism driving the mixing. Today, the non-standard processes that are thought to lead to a transport of material inside the interiors of stars are the following ([179]):

1. Atomic diffusion through radiation, temperature, or gravitation
2. Rotation leading to turbulence and meridional circulation
3. Convective overshooting

4. Internal gravity waves
5. Magnetic fields

Naturally, not all of these mechanisms have to occur at the same time, they differ depending on the initial mass of a star and on its evolutionary stage. Also their influence on the lithium depletion is very diverse and again depends on the stellar parameters. On the other hand, these processes do not only influence the photospheric lithium abundance, of course, but, through the redistribution of elemental abundances, they have an impact on the evolutionary tracks, lifetimes, and the abundances of other elements, too.

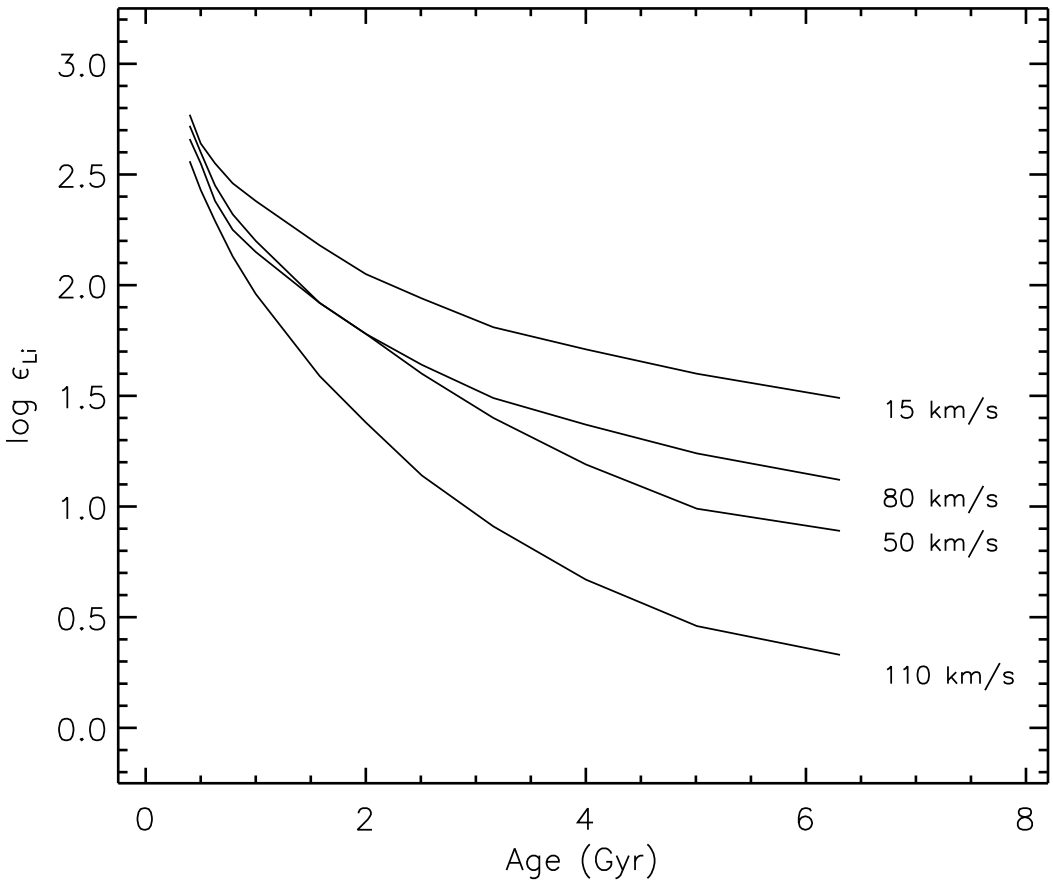

Figure 1-2: Model predictions for lithium depletion in solar-type stars depending on the initial rotational velocity. From Charbonnel & Talon, 2005 [31].

The physics for meridional circulation and turbulence in rotating stars and their interaction is described very thoroughly by J. P. Zahn (1992, [191]). His calculations, however, ignore magnetic fields and gravity waves. Maeder & Zahn revised those models (1998, [92]) by adding expansion and contraction as well as horizontal turbulence. A very extensive model on stellar evolution with rotation was published by Meynet & Maeder in 1997 ([103], see especially their Section 3). Thermal effects were discussed by Maeder & Meynet in 1996 ([91]). In 2007, Zahn reviewed the link between internal differential rotation, turbulence, and large-scale meridional circulation ([192]).

Around the same time, D'Antona & Mazzitelli published an extensive work on the evolution of low-mass stars (1997 [37]). D'Antona et al. also worked explicitly on the model influence on lithium abundances with special regards on magnetic fields and overshooting (1998 [38]).

Models also came from Talon & Charbonnel: in 2002 and 2003, they published works on angular momentum transport by gravity waves ([180, 178]), where they also explain how waves are generated (their Section 2). S. Talon presented an extensive review on rotational mixing in 2004 ([177]). In 2005, Charbonnel & Talon presented detailed model prediction for lithium depletion depending on the initial rotational velocity of a star ([31, 179]). Those models include rotation, internal gravity waves, and atomic diffusion as activators for extra mixing. In 2008, an up-to-date version followed containing all influences on non-classical mixing as well as the importance of gravity waves for the rotation profile ([32]). The peculiarity of the Talon & Charbonnel codes is the consistent combination of extra-mixing processes. An example of the lithium depletion predictions from these publications is plotted in Figure 1-2. Note that the models for and initial rotational velocity of 50 and 80 km/h intersect, which is why the predicted surface lithium abundance for a

star older than about 2 Gyr will be lower for a lower initial rotation.

Other noteworthy contributions to an understanding of the physics that lead to lithium depletion in main sequence stars came from Michaud (1986, [105]) and Chaboyer et al. (1995, [30]), who used diffusion as the driving force, Swenson & Faulkner (1992, [172]), who worked on mass-loss as a reason for lithium depletion, Montalban & Schatzman (2000, [110]) using internal gravity waves, Eggenberger et al. (2008, [51]), do Nascimento et al. (2009, [43], see also references therein), and Lagarde et al. (2012 [83]).

1.2.4 Lithium and planets

The possibility that the presence of a planet might influence a star's photospheric lithium abundance and therefore could explain the large spread in observed lithium abundances has been discussed for quite some time (see, e.g., [64]). First attempts to study a possible connection came to differing results: Gonzalez & Laws (2000, [66]) found a smaller lithium abundance in planet hosts compared to field stars, provided the lithium abundances were corrected for trends in fundamental parameters, while Ryan (2000, [142]) and Gonzalez et al. (2001, [67]) could not find a trend in their samples.

In 2004, Israelian et al. ([77]) claimed to have found a noteworthy difference between solar-type planet hosts and comparison field stars concerning lithium abundances. This result was largely confirmed by subsequent publications (see, e.g., [77, 174, 34, 175, 21, 27, 65]).

5 years later, Israelian et al. (2009, [76], hereafter I09) reported a significant difference in surface abundances based on a sample of 82 solar-type stars. More precisely, they claimed that planet host stars show an in average lower photospheric lithium abundance than field stars without planets and that stars with a lithium abun-

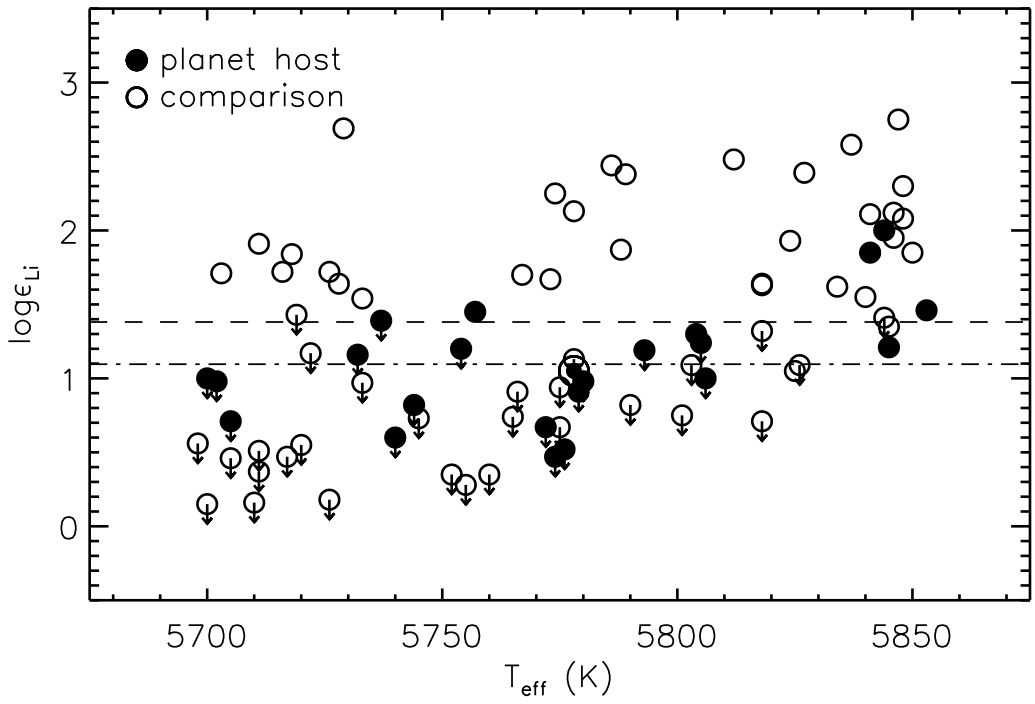

Figure 1-3: The results from Israelian et al. (2009, [76]). In this sample, comparison stars are in average more lithium-rich than planet hosts: the mean $\log \epsilon_{Li}$ for planet hosts is 1.08 dex, whereas the mean for the comparison sample is 1.39 dex (overplotted dashed and dash-dotted lines, respectively). The arrows denote stars, for which only $\log \epsilon_{Li}$ upper limits could be determined.

dance above a certain amount most likely do not host planets.

Figure 1-3 shows the results presented in the Israelian et al. 2009 publication (see their Figure 1): plotted is the surface lithium abundance ($\log \epsilon_{Li}$) versus effective temperature (T_{eff}) for their sample of 82 solar-type stars including planet information (filled symbols represent confirmed planet hosts). The average surface lithium abundance in the planet hosts is 0.3 dex (about two times) lower than the one in the stars where no planet had been found.

The scenario leading to this relation is based on the assumption that in order to establish planets, the protoplanetary disk around a young star has to be stable for longer than the typical time scale for a field star without planets. This long-lasting

interplay between the star and the disk slows down the star's rotation, which leads to an increase in differential rotation inside the host, i.e. between the core and the envelope. This will cause an enhanced mixing between the two regimes and thus a higher rate of lithium burning than in stars without planets. Also later the migration of planets could effect lithium depletion by influencing stellar angular momentum and induce extra mixing. However, the effect of at least the latter is debatable, since at this stage, the temperatures in the convective zone in a solar-type star will not be hot enough for proton-capture reactions to destroy lithium, so non-standard mixing processes are required again.

This hypothesis is strengthened by two publications by Takeda et al. ([175, 173]), who describe the stellar angular momentum as the crucial parameter for lithium depletion in solar-type stars. They also show, that slow rotators show an enhanced lithium depletion. Their data, however, does not allow to identify planets as the main reason for enhanced depletion, because it contains only a small fraction of planet hosts, and because of the fact that only the projected rotational velocity ($v \sin i$) could be accounted for, which is only statistically connected to the actual rotational velocity. Their data does, however, fortify model predictions such as [31], that anticipate a strong dependence of surface lithium abundance from the initial rotational velocity.

Note also, that according to the models by Charbonnel & Talon, stars with a low *initial* rotational velocity show a higher surface lithium abundance. That does of course not conflict with extra depletion due to a slowed down rotation. It could even support parts of the hypothesis of increased depletion in host stars, since initial slow rotators cannot be slowed down by the same amount as fast rotators, and therefore cannot develop a similar maximum differential rotation. But the models do conflict with possible explanations that predict a more likely planet formation in

slow rotators (e.g., [21]).

In contrast to the above-mentioned results, publications such as [142] and [90] find that stars with planets show the same lithium distribution as stars where no planets have been found so far. They conclude that the differences found by other groups are most likely based on systematic differences in the temperature scales of the used sub-samples.

Chapter 2

Data and Reduction

The data used for spectroscopic analyses are usually obtained with echelle spectrographs. In those instruments, the light is first refracted by a conventional grating, that creates one order containing the full spectrum. It then passes an echelle grating mounted orthogonally to the first one. This echelle grating separates the wavelength orders in a way that leaves small overlapping regions on the edges of each order. The advantage of this concept is a very high resolution (the UVES spectrograph at the VLT reaches a resolution of 110,000 in the optical red optical region, see below for definition.), together with the possibility to fit a large wavelength range on one CCD chip. Usually, in modern instruments, at least two CCDs are used to cover a large range with a high resolution. The concept of echelle spectrographs, though discovered in the late 1800s, was first applied by Nagaoka & Mishima in 1923 [112].

The obtained data can be classified using different specifications, that depend on the instrument and exact setup and conditions:

1. The wavelength range is the most obvious one. It is determined by the sensitivity of the CCD chip used in the instrument. For our work, we want to use

the optical regions. They spread from about 3800 to 7800 Å, the data in the optical bands may extend some 100 Å beyond that.

2. The spectral resolution is $R = \lambda/\Delta\lambda$, where $\Delta\lambda$ is the smallest wavelength difference that can be distinguished at a given wavelength λ. It depends mostly on the width of the entrance slit, but also on the spacial resolution of the CCD chip.
3. The signal-to-noise ratio (S/N) is a quantity resulting from the resolution. A higher resolution results in signal counts in fewer bins competing with fewer background photons. During observations, the S/N ratio varies with the conditions such as temperature, wind, and air mass. The value is very important in the identification of weak lines, since it defines the lower detection limit. We use the definition as the reciprocal of the coefficient of variation, i.e., the ratio of mean of our signal to its standard deviation for a small, clean wavelength region.

2.1 Observation

For this work, we gathered data for different types of stars. The main targets, however, are solar-type objects, that means, their fundamental parameters effective temperature, surface gravity, microturbulent velocity, mass, and metallicity are very similar to those of the Sun. Age is not a criterion, since we also want to follow the evolution of the surface lithium abundance in a given object. Also, the fundamental parameters do not change significantly during the main sequence phase.

The data for this work were gained from different instruments: the HARPS spectrograph on the 3.6m ESO telescope at La Silla, Chile, the MIKE spectrograph on the 6.5m Magellan Clay telescope at Las Campanas, Chile, the UVES spectro-

graph on the 8.2m VLT at the Paranal observatory, Chile, and the Robert G. Tull (RGT) spectrograph on the 2.7m Harlan J. Smith telescope, McDonald observatories, Texas. The instrument and data specifications are listed in Table 2.1.

1. The majority of the MIKE spectra were obtained by us in two dedicated observing runs in January and June 2011, additional MIKE data for α Centauri Aand some solar analogs were taken from [131, 96, 102].
2. HARPS data was selected from the ESO archive: http://archive.eso.org/cms.html
3. UVES data for 36 subgiant stars was obtained in a dedicated observation in service mode in ESO period P87 (September 2010 to February 2011) (PID 087.D-0724A) and can also be found on the ESO archive.
4. RGT spectra are from [131].

Instrument	λ(Å)	R_{max}	S/N @ 6700 Å
HARPS	3780-6910	115,000	300-450
MIKE	3400-9000	65,000	$\geq$ 500
UVES	3000-11000	110,000	250-600
RGT	3800-9125	60,000	$\geq$ 200

Table 2.1: Instruments used for data acquisition for this work.

The goal in the observations was to gather spectra with the highest quality possible in order to be able to fit the lithium doublet at 6708 Å, which is very weak in solar-type, solar $\log \epsilon_{Li}$ stars. To achieve this, a signal-to-noise (S/N) ratio of at least 200 is necessary in that region. For the determination of other elements, we aim for a minimum S/N of 200 at 5500 Å. For typical nearby stars with a visual magnitude of around 7, the exposure time is limited by saturation and therefore very sensitive to environmental conditions, mainly seeing, which is the reason why we used exposure times between 30 seconds and 10 minutes. In order to increase the S/N of the data, we took several exposures of every object, that were co-added in the reduction process as described in the next section. An example for a typical

observing run is given in Table 2.2. It shows the difficulty of achieving spectra with a sufficiently high signal-to-noise ratio, that are not saturated. 45 Flat field spectra were taken at the beginning of each night together with 5 bias frames. ThAr spectra with 4 and 8 seconds of exposure time were obtained roughly every hour.

File	Object	UT^{Start}	$Exp.^{Secs}$	Airmass	Seeing	Comments
158-172	Quartz Flat	-	50	-	-	-
173-182	Bias	-	-	-	-	-
183-212	Milky Flat	-	180	-	-	-
213	ThAr	23:00	4	-	-	-
214	ThAr	23:00	8	-	-	-
215-217	HIP60729	23:10	45	1.06	0.65	-
218	HIP62039	23:15	180	1.1	0.7	-
219	hip62039	23:19	210	1.1	0.7	-
⋮	⋮	⋮	⋮	⋮	⋮	⋮
241	ThAr	1:00	4	-	-	-
242	ThAr	1:00	8	-	-	-
243	HIP73241	1:00	180	1.07	0.7	Saturated
244-245	HIP73241	1:07	90	1.07	0.8	Saturated
246-248	HIP73241	1.10	60	1.07	0.7	-
249	HIP74273	1:20	45	1.3	0.7	-
250-252	HIP74273	1:22	60	1.3	0.7	-
⋮	⋮	⋮	⋮	⋮	⋮	⋮

Table 2.2: Excerpt from the MIKE observing log from June 24, 2011

Table A.3 in the Appendix lists all objects obtained during the MIKE observing runs that have been used in this work.

For every night of observing, spectra for solar reference objects were taken as well. Those are crucial for the differential analysis of the samples. This way, we are able to exploit the extremely precise knowledge about the solar fundamental parameters and composition as well as the fact, that a differential analysis holds very accurate results on the relative scale.

For our samples, we use asteroids as solar reference objects. Meléndez et al.

(2012, [99]) have shown, that the choice of asteroid does not influence the result, as long as the source is bright enough. This premise does not cause any problems, since we observed the brightest asteroid available each night, which resulted in a typical visual magnitude of less than 6 and also reduced the necessary exposure times by a lot. Asteroids are used, because their spectra are not affected by atmospheric scattering as it would be the case when using sky spectra. Also, unlike the moon, they are basically point sources, which makes it possible to analyze their spectra in the exact same way as the stellar objects.

2.2 Data reduction

Figure 2-1: Example for an image produced by the MIKE spectrograph.

The data taken at a spectrograph is barely usable in its raw format. The instruments we gained our data from all use an echelle grating, that splits the incoming light into several orders (see Figure 2-1). In some orders, absorption lines can already be seen, but a lot of work such as order extraction and calibration has to

be done before the data are usable. For MIKE and UVES, reduction pipelines are available. They are able to deal with the whole process of data reduction as described below. For data where no pipeline was available or the quality delivered by the available pipelines was not good enough for our purposes, we used the *IRAF*[1] package for a manual data reduction. *IRAF*stands for Image Reduction and Analysis Facility and is a free software collection for UNIX-like operating systems built for data reduction and visualization purposes.

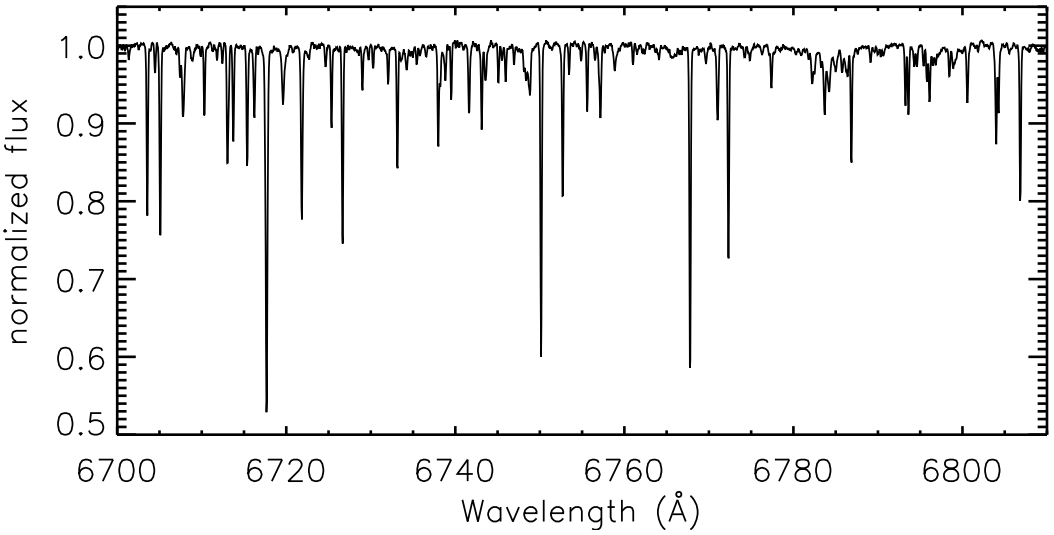

Figure 2-2: Detail of the plotted spectra for HIP117320.

As a first step in the data reduction, we removed bad pixels by applying a bad pixel mask to all spectra, which calculates a value for the bad pixel(s) from interpolating the surrounding pixels. The dark overscan regions, that don't contain any information, where removed. Bias subtraction was done to account for noise coming from the electronic. Then we corrected for the non-uniform sensitivity (leading to pixel-to-pixel variations) by applying high-S/N flat fields and dark frames and removed scattered light by fitting high-order polynomials to the counts between the

[1]Information and download at http://iraf.noao.edu/.

orders. Wavelength calibration was done using the spectra from a thorium-argon (ThAr) lamp taken at the beginning of every observing night. The (known[2]) positions of the lines were translated into a pixel-to-wavelength relation that was then applied to the object spectra. We also corrected for wavelength shifts due to rotation of the Earth as well as the star itself. Radial velocity shifts were determined by cross-correlating the exposures with a reference spectrum where the radial velocity is known.

After the spectra were brought to the correct wavelength scale, we co-added them. Co-adding the spectra before normalizing them is advisable to achieve better quality, because in that way, we automatically weight spectra by their photon count, and spectra with low counts and resulting low signal-to-noise ratios still contribute to the quality of the combined spectra without lowering the final S/N.

Up to this point, the orders are blaze-shaped (see Figure 2-1). This is caused by the echelle grating. Before being able to add the different orders into one spectrum, we have to normalize their continuum, i.e. the upper envelope of the spectra that would be emitted without any absorption or emission. This is done by fitting a high-order polynomial to the upper envelope of each order. This is a very crucial point and has to be done very carefully, so the envelope is not obstructed by broad lines.

Finally, the orders are merged into one single data array (Table 2.3, Figure 2-2). In that step, the overlap between the orders has to be taken into account concerning their wavelengths but also the resulting higher continuum, that has to be normalized once more for those regions. Again, a wavelength template is used here to make sure the final spectra are calibrated.

[2]A ThAr line atlas can be found here: http://www.noao.edu/kpno/specatlas/thar/thar.html

λ (Å)	Normalized flux
⋮	⋮
6749.7528977920	1.003637
6749.8016768289	1.003443
6749.8504558658	0.998216
6749.8992349027	0.994076
6749.9480139396	0.985308
6749.9967929765	0.943199
6750.0455720134	0.842381
6750.0943510503	0.692747
6750.1431300872	0.600332
6750.1919091241	0.646885
6750.2406881610	0.785039
6750.2894671979	0.906796
6750.3382462348	0.969707
6750.3870252717	0.993064
6750.4358043086	0.997455
6750.4845833455	0.999506
6750.5333623824	1.001579
6750.5821414193	1.002137
6750.6309204561	1.002523
6750.6796994930	1.001881
⋮	⋮

Table 2.3: Detail of the spectral data for HIP117320.

Chapter 3

Analysis

3.1 Stellar spectroscopy

Most information in astronomy is gathered using spectroscopic methods. In spectroscopy, the emitted spectra of the stars are analyzed regarding their absorption and emission lines. Usually, as a stellar spectrum, we regard the received flux versus respective wavelength. For different purposes, different wavelength regions of a star's spectrum are useful.

The photons that are emitted from the surface are produced in the stellar core in nuclear fusion (and fission) reactions. The energy transport is made possible by both convection and a temperature gradient in every layer of the star. In the radiative interior of a solar-type star, matter is very opaque to radiation, the mean free path for photons is typically in the order of 1 cm. Photons are continuously being absorbed by bound-bound, bound-free, and free-free interaction and scattered by electrons. Therefore, photons move outwards very slowly in random walk patterns, which results in a typical photon escape time of 10^7 years. This time span is also known as the Kelvin-Helmholtz timescale. The extremely small temperature gradient of

$\Delta T/T \simeq 10^{-11}$ is large enough to cause a net energy transport towards the outer layers. On the other hand, it is small enough to result in an almost perfect black body radiation.

In the outer layers of solar-type stars, convection dominates as the main process for energy transportation. The photons heat up the bottom of the convective layers, which leads to upflows of hot matter and to downflows of cooler, dense matter. A proper description of convection is a very difficult task, because it requires solving the hydrodynamical equations in three dimensions over an extremely large range of lengths, times, temperatures, pressures, and densities. A widely used, simple approach to the processes taking place hear is the one dimensional so-called mixing-length theory.

In the so-called photosphere, where the photons finally escape the star, the atoms are neutral or only lightly ionized. Absorption occurs, when the energy of a photon encountering an atom is close to a resonant energy of the atom, i.e. the energy that is necessary to bring the atom from one quantum state to a different one. Eventually, the atom will go back to its ground state again, releasing a photon with the resonant energy. This photon, however, is emitted in a random direction, and therefore most likely will not move along the line of sight of the observer.

The energy of a photon equals $\hbar\nu$, that is, Planck's constant times its wavelength. Provided the medium in which these resonant absorptions occur is large enough (which certainly is the case for stellar photospheres), those processes take place statistically. A wavelength that corresponds to a resonant absorption for a certain atom will therefore show a lower flux as an interval without any resonances. This will be seen as an absorption line in the spectrum.

The strength of an absorption line depends on the relative amount of an atom in the medium, but also on the cross section of the absorption. However, every

element has resonant wavelengths specific to the ground and excited quantum states that cause the absorption of a photon. Knowing these wavelengths, we are able to identify elements in a star's spectrum.

3.1.1 Line broadening

The determination of an actual abundance however is subject to a large variety of influences, such as the atomic data of the elements itself and effects that influence the shape of the line. A spectral line is never infinitely sharp, because the lifetime of an excited state is finite. That leads to a small Lorentzian distribution around the peak, caused by the energy-time uncertainty:

$$L(E) = \frac{1}{\pi} \frac{1}{1 + \left(\frac{\tau(E-E_0)}{\hbar}\right)^2} \tag{3.1}$$

with $\Delta E = 2\hbar/\tau$ being the full width at half maximum of the distribution.

Also the thermalized particles themselves show a distribution in energy, that is, not every particle moves at the same speed or in the same direction. For a single atom, this leads to a wavelength shift relative to the original resonant wavelength. For the whole volume, those statistical shifts sum up to an additional Gaussian broadening of the absorption line. The resulting line is then a convolution of the original Lorentzian profile with a Gauss profile, a so-called Voigt profile.

Even though this Doppler broadening is the main source of line broadening, also pressure broadening has an effect on the line width. It is caused by the interactions between the particles and shows two components: impact pressure broadening is caused by particle collisions, that shorten the lifetime of an excited state, leading to a higher energy-time uncertainty and therefore an additional Lorentzian share. Quasistatic pressure broadening on the other hand is caused by the presence of

particles, that may shift the energy levels in an emitting particle. Here, the line shape depends strongly on the force that causes the shift as well as on the distance to the disturbing particle.

A photon that was emitted by an atom can of course be re-absorbed by another atom of the same species. Since the energy of the emitted photon may already be altered by broadening effects, the absorption probability is higher for photons with an energy near the line center. This so-called opacity broadening (or sometimes self-absorption) caused a flattening of the line and may sometimes even lead to an inverted line that is stronger in the wings than it is in the center.

3.1.2 Atomic data

Knowing the atomic properties of an absorption line is crucial in order to derive information from it. The wavelengths and the energies of the lower and upper excitation levels (χ_l and χ_u) are usually well known, whereas the so-called *weighted oscillator strength* is subject to continuous revision. It is denoted as gf, or often $\log gf$, and consists of the oscillator strength of the transition from the lower excited state to the higher one and the statistical weight g of the lower state. Semi-empirical determinations of the gf values started in the 1960s, comprehensive work was done by, e.g., Warner (1967, [187]), Kurucz & Peytremann (1975, [82]), and Milone & Milone (1984 [107]). The results are continuously being reviewed and updated, recent work has been done by Raassen & Uylings (1998, [128]), Fuhr & Wiese (2006, [58]), Schnabel et al. (2004, [151]), and Meléndez & Barbuy (2002, 2009b, [97, 98]), just to name a few.

3.2 Model atmospheres

Model atmospheres of stars are necessary to determine the influences of effective temperature (T_{eff}), surface gravity ($\log g$), metallicity ([Fe/H]), and microturbulent velocity (v_t) on the radiation leaving the photosphere. For this work, we used the *ATLAS 9* model atmospheres computed by Kurucz (1979, [81]) in their latest version from 2004 ([26][1], see also [148, 150]). This classical model uses some major physical simplifications:

1. The models are plane parallel, i.e. cubic volumes are used instead of spherically symmetric ones.
2. The models are one-dimensional: the gas distribution is considered homogeneous, therefore the only necessary dimension to describe the physics inside the volume is the depth.
3. Local thermodynamic equilibrium (LTE): intensive (scale invariant) parameters vary slowly enough so thermodynamic equilibrium can be assumed for the volume in question.
4. Hydrostatic equilibrium: the whole volume is at constant velocity, because gravitational compression is canceled out by the pressure gradient (Buoyancy).
5. Homogeneous chemical composition of the whole volume
6. No influences from magnetic fields and rotation

The influences of the given simplifications are reasonably small, especially since our analysis is strictly differential and relative to the Sun, for which those models are well tested and very precise. The LTE assumption, however, does have a significant influence on some elements, therefore we have to take non-LTE correc-

[1] *ATLAS 9* model grids are available at http://kurucz.harvard.edu/grids.html

tions into account for those. The elements and necessary procedure are explained later in Sections 3.4 and 3.5. For details on the impacts of the model simplifications, see [7].

In order to work with a model atmosphere, routines such as *MOOG*[2] ([158]) are needed to create model spectra from the grid and an appropriate line list. Those synthetic spectra are then used to compare them with actual observed spectra to determine basic stellar parameters and chemical abundances.

3.3 The fundamental parameters

3.3.1 Equivalent widths

Equivalent widths (EW) of neutral and ionized iron are used to estimate the fundamental parameters effective temperature, surface gravity, microturbulent velocity, and, of course, metallicity. The equivalent width of a line is the width of a hypothetical rectangle with height equals one and the same area as the line that is treated.

For the measurement of equivalent widths, automated routines such as *ARES* ([164][3]) are available. For a given set of absorption lines, this routine tries to normalize the spectra locally around each line and fits a Gaussian profile to it. However, we decided to measure the EWs manually using *IRAF*, because of uncertainties that may occur when fitting the continuum near broad or emission lines. This alternative is a lot more work intensive that the automated one, but we want to be able to rely on the EW of every single line. In addition, *IRAF* enables us to fit Voigt profiles to the lines, which, in many cases, is the better option, since a gaussian fit tends to un-

[2] available at http://www.as.utexas.edu/ chris/moog.html
[3] obtainable from http://astro.up.pt/ sousasag/ares/

derestimate the line wings, especially in broader lines. As explained before, a Voigt profile is a convolution of Gauss and Lorentz profiles, where the Lorentzian share is caused by the uncertainty in the lifetime of an excited state, while the Gaussian one comes from thermal Doppler broadening of the line. Pressure broadening may lead to an enhanced Lorentzian due.

The uncertainties in the process of manual EW measurement are in the order of some mÅ and have to be accounted for in the later error analysis.

3.3.2 Fundamental parameters from equilibria

λ (Å)	Element	χ_l (eV)	log gf	λ (Å)	Element	χ_l (eV)	log gf
4445.47	Fe I	0.087	-5.412	6609.11	Fe I	2.559	-2.682
5247.05	Fe I	0.087	-4.961	6699.14	Fe I	4.593	-2.101
5491.83	Fe I	4.186	-2.188	6739.52	Fe I	1.557	-4.794
5600.22	Fe I	4.260	-1.420	6750.15	Fe I	2.424	-2.605
5661.35	Fe I	4.284	-1.756	6793.26	Fe I	4.076	-2.326
5696.09	Fe I	4.548	-1.720	6837.01	Fe I	4.593	-1.687
5701.54	Fe I	2.559	-2.163	6854.82	Fe I	4.593	-1.926
5705.46	Fe I	4.301	-1.355	6945.21	Fe I	2.424	-2.454
5778.45	Fe I	2.588	-3.44	6978.85	Fe I	2.484	-2.479
5784.66	Fe I	3.396	-2.532	7401.69	Fe I	4.186	-1.500
5855.08	Fe I	4.608	-1.478	7912.87	Fe I	0.859	-4.848
5956.69	Fe I	0.859	-4.552	4576.33	Fe II	2.844	-2.950
6151.62	Fe I	2.176	-3.282	4620.51	Fe II	2.828	-3.210
6200.31	Fe I	2.608	-2.416	5234.62	Fe II	3.221	-2.180
6240.65	Fe I	2.223	-3.287	5264.80	Fe II	3.230	-3.130
6265.13	Fe I	2.176	-2.547	5414.07	Fe II	3.221	-3.580
6297.79	Fe I	2.223	-2.715	6432.68	Fe II	2.891	-3.570
6311.50	Fe I	2.831	-3.141	6516.08	Fe II	2.891	-3.310
6498.94	Fe I	0.958	-4.695	7222.39	Fe II	3.889	-3.260
6518.37	Fe I	2.831	-2.448	7224.48	Fe II	3.889	-3.200
6574.23	Fe I	0.990	-5.010	7515.83	Fe II	3.903	-3.390
6593.87	Fe I	2.433	-2.394	7711.72	Fe II	3.903	-2.500

Table 3.1: Iron lines used for the determination of the fundamental parameters.

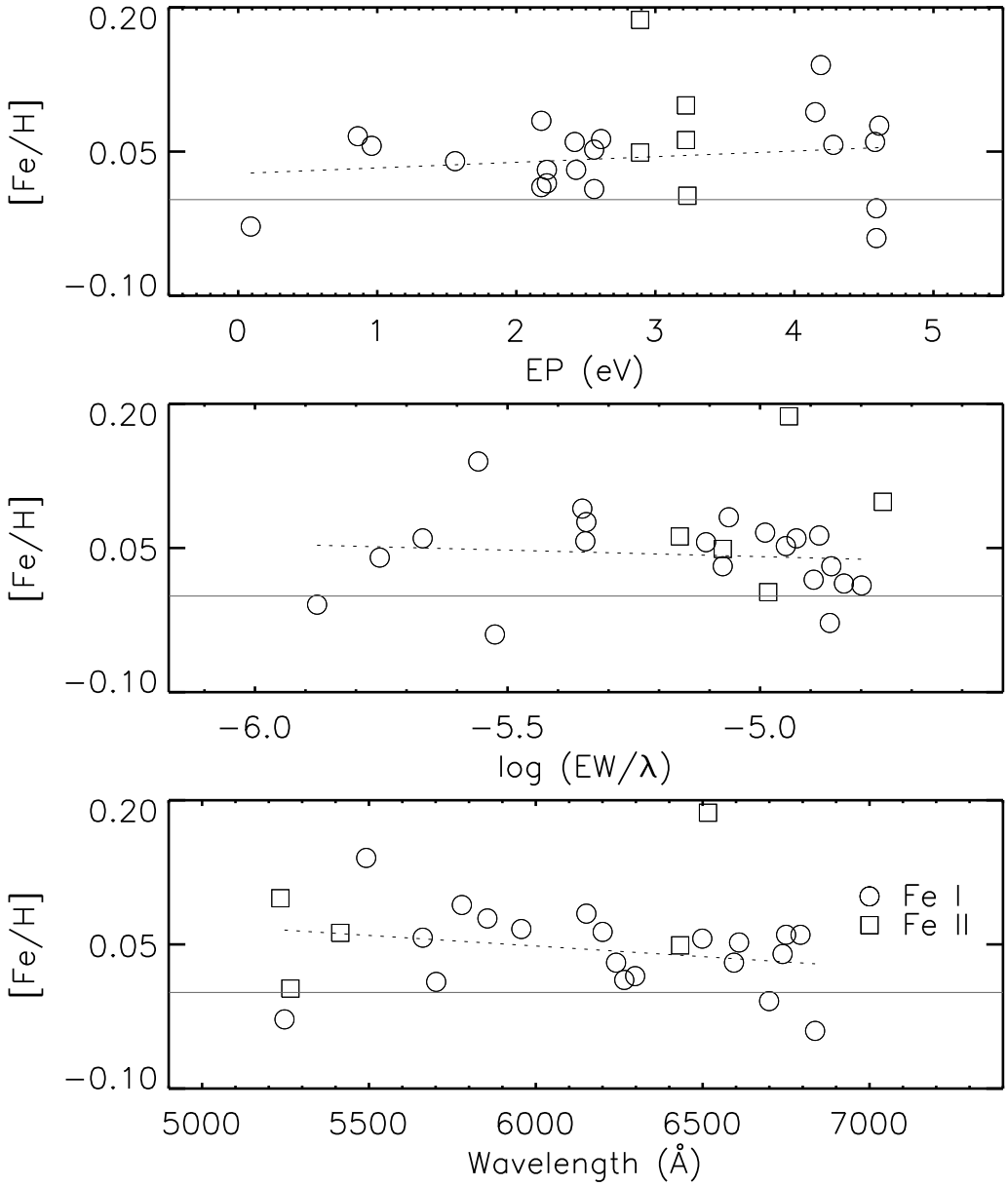

Figure 3-1: Snapshot from the parameter determination process. Shown are the lower excitation potential, reduced equivalent width, and wavelength of each line and their corresponding metallicity for HIP117320.

In order to determine the fundamental stellar parameters, iron equivalent widths can be used exclusively taking advantage of ionization and excitation equilibria. In

a first step, an initial set of values is guessed (typically the solar values for solar-type stars). Those are fed into the model together with the known values for each line: wavelength, measured equivalent width, and atomic data (excitation potential (χ) and astrophysical gf value ($\log gf$). From the model, we gain iron abundances for each line according to the input parameters. Those are plotted as in Figure 3-1. The parameters $T_{\rm eff}$ and v_t are then iteratively varied so that the [Fe/H] versus χ_l and log(EW/λ) trends (dotted lines in Figure 3-1) become flat. The surface gravity $\log g$ is obtained from changing its starting value so, that the difference between the mean Fe I and the mean Fe II disappears. The final [Fe/H] value is a natural result from the optimization of the other parameters as soon as the slopes approach zero and the values for neutral and ionized iron are the same.

Each step is being calibrated to the solar values by using a solar reference spectra and its EWs and comparing the results line by line. So since we typically start with solar fundamental parameters as a first guess for a new object, a larger equivalent width will result in a larger iron abundance for that line in the first step. The slope of the Fe I lines then leads to a readjustment of the parameters and a new estimate of [Fe/H].

In some cases, the iron abundances for single lines deviate visibly from the main trend. In those cases, the lines in question have to be looked at more carefully. Sometimes, the deviation is caused by an ungrateful measurement that leads to a wrong continuum, sometimes the reason is a blend. If a careful second measurement and/or de-blending cannot solve the problem, it usually is a good idea to remove the line from this object's line list.

This whole process is done by a routine and completely automatically to ensure independent and impartial results. The only human interaction is the reviewing of the mentioned deviating lines, but also that can be avoided by a so-called 'sigma

clipping', that simply removes lines that are off by a certain sigma value. Note that Figure 3-1 does not show the final result, but a snapshot from the process. The spread in [Fe/H] is still large, also the slope in [Fe/H] versus EP and versus wavelength is too steep. A result like this will force the routine to go back and vary the parameters.

Meléndez et al. (2012, [99]) showed, that the model dependency of this type of analysis is negligible.

The line list used for the stellar parameter determination in this work consists of 34 Fe I and 11 Fe II lines that are very carefully selected. A broad range of wavelengths from 4445 to 8294 Å (if applicable to the respective spectra), equivalent widths from about 10 to 130 Å, and lower excitation potentials (χ_l) from 0.1 to 4.6 eV is used to reduce the possibility of degenerate results caused by very similar lines. The list is based on the lines used by [96, 8] and carefully shortened to the most reliable ones in terms of blending and continuum determination. The whole list including atomic line data can be found in Table 3.1.

For the quality of the spectra used in this work, we obtain fundamental parameters with the following typical uncertainties: $\sigma(T_{eff})$ = 40 K, $\sigma(\log g)$ = 0.06 dex, and σ([Fe/H]) = 0.025 dex.

The propagated errors from EW measurements are obtained by conducting the parameter analysis also for the upper and lower limits for the equivalent widths. This results in typical combined uncertainties of 50 K in T_{eff}, 0.1 dex in $\log g$, and 0.04 dex in [Fe/H]. Note that those are only average values. The exact results of our error analysis are given in Chapters 4, 5, and 6.

3.3.3 Ages and Masses

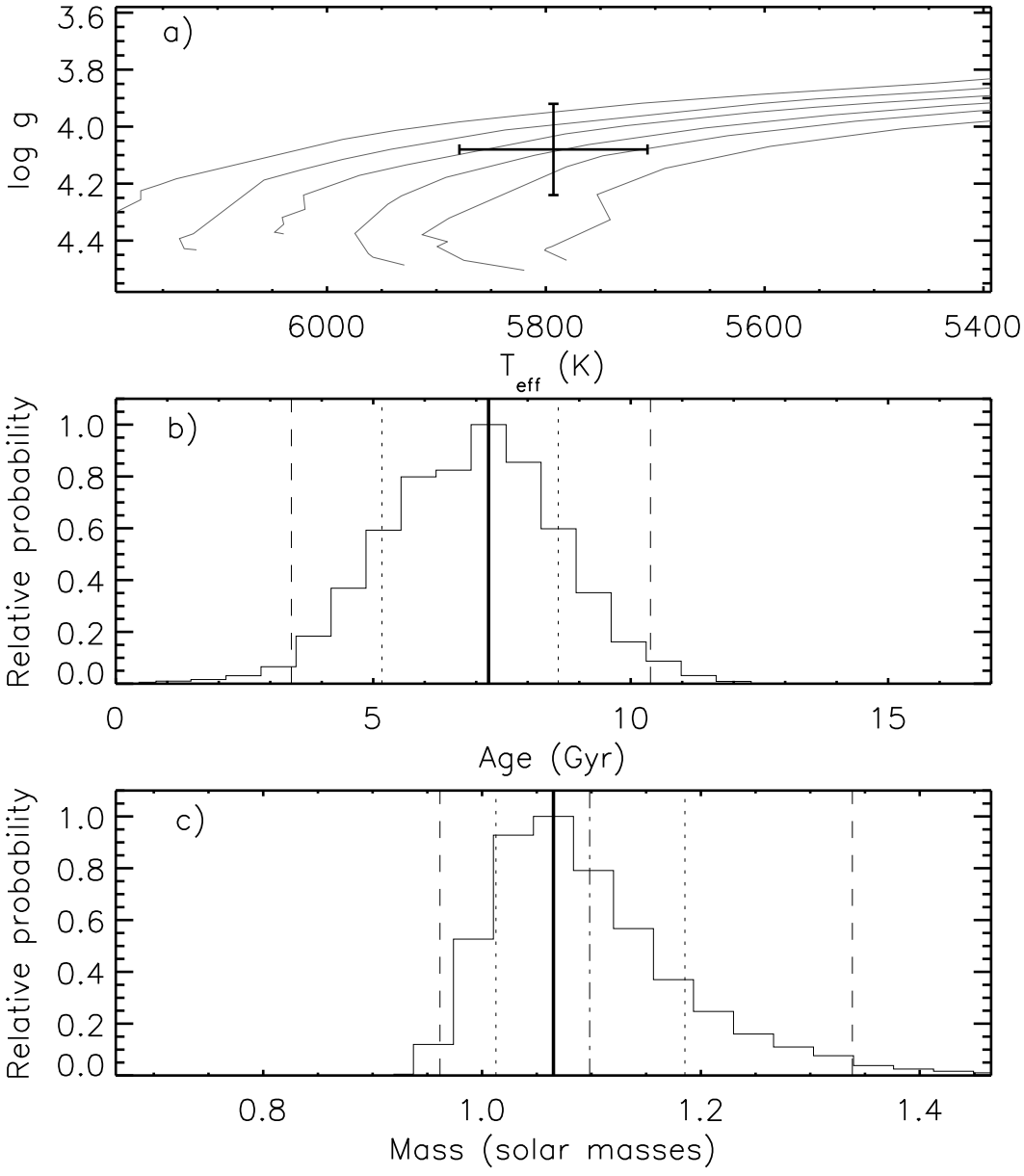

Figure 3-2: $\log g$ versus $T_{\rm eff}$ with overplotted evolutionary tracks for metallicities of -0.1, -0.05, 0.00, 0.07, 0.1, and 0.15 dex for a constant stellar mass of 1.065 $M_{\odot}$ (a)), age and mass probability distributions (b) and c)) for HIP117320.

Ages and masses of stars for this work are obtained from isochrone fitting. This technique was invented by A. Sandage in 1962 [145] with substantial contribution from Demarque & Larson (1964, [41]) and has since been improved by various groups. It is very sensitive to the fundamental parameters T_{eff}, $\log g$, and [Fe/H] as well as the calibration of the model isochrones, i.e., the isochrones have to be tested to reproduce the solar mass and age precisely. We used a grid of Y^2 isochrones[4] with a very small metallicity step size of 0.01 dex for [Fe/H] ±0.15 and a somewhat larger step size of 0.02 for the rest of the metallicities. Through normalization, we found a necessary offset of 0.04 dex in [Fe/H] to reproduce the solar mass and age. This normalization leads to a solar mass of 1.000 ±0.003 $M_{\odot}$ and age of 4.5 ± 0.2 Gyr for solar parameters of T_{eff} = 5778 ± 150 K, $\log g$ = 4.44 ± 0.1, and [Fe/H] = 0.0 ± 0.1, where the uncertainties represent the maximum errors for which the calibration is still valid. Note that no offset was needed in T_{eff} and $\log g$.

The process of determining masses and ages follows the one explained in [138, 4], but with the Y^2 isochrones described above. We determine each star's position in the $\log g$-T_{eff} plane and from that conclude its position on a grid of evolutionary tracks (panel a) in Figure 3-2). From the points in the 3 σ environment around that position, we obtain probability distribution functions for mass and age that we use to infer a most likely value as well as 1 and 2 σ minima and maxima. We also determine so-called simple masses and ages and their errors; those are a simple mean and standard deviation of the mean of all points in the 3 σ environment.

Panels b) and c) in Figure 3-2 show the mass and age normalized probability distributions for HIP117320 (spectra from MIKE) as an example. The vertical solid lines mark the values of highest probability, the dotted and dashed lines are the 1 and

[4]The Yonsei-Yale collaboration, [190, 40]. The data are available online at http://www.astro.yale.edu/demarque/yystar.html. The techniques, models, and compositions used for the generation of these tracks are presented in several publications linked on the website.

2 σ lower and upper limits, respectively. The dash-dotted line in panel c) represents the simple mass. The simple age is not visible in panel b), because it coincides with the most likely age.

Panel a) is a visualization of the process in the Hertzsprung-Russel (HR) diagram for the same star. Overplotted are evolutionary tracks for different metallicities between -0.2 and 0.2 around the star's determined value of 0.068 ± 0.054.

Isochrone ages are only reliable down to about 3 Gyr. For most stars younger than that, only upper limits could be obtained. For objects where this was the case, we adopted ages from other works, that were obtained using gyrochronology and X-ray luminosity. In a few cases of stars with ages between 2 and 4 Gyr, we used an average of isochrone ages and ages determined from gyrochronology to improve the result.

In gyrochronology, the rotational period of a star is used together with its colors to determine its age. It basically uses the relation $1/\sqrt{\tau} \sim v \sin i$ (where τ stands for the age of the object) discovered in 1972 by A. Skumanich [156]. This relation, however, is very vague due to the unknown inclination angle i. So instead of the projected velocity, the rotational period (P_{rot}) is used nowadays. P_{rot} can be measured from the modulation of the emission due to starspots (see, e.g., Barnes 2007 [12]). The rotational periods used in this work are adopted from [60, 122, 12].

X-ray luminosity (10^{-2}Å to 100 Å) can be used as an magnetic activity indicator. It is calibrated well enough so that we are able to infer ages for solar-type stars with a high accuracy (see, e.g., [2, 71]).

For older stars with a very high uncertainty in the age determination, we used the activity-based ages by Saffe et al. (2005, [144]) and Mamajek & Hillenbrand (2008, [93]).

3.4 Elemental abundances

For most elements, abundances can be determined more or less directly from the equivalent widths of their absorption lines and the corresponding models using *ATLAS 9* model atmospheres and *MOOG*. We measured the equivalent widths of 514 spectral lines for 20 elements for this analysis. All lines including their atomic data and the widths measured for our α Centauri A spectra are presented in Table A.4 in the Appendix.

As for the fundamental parameters, also this part of the analysis is strictly differential with respect to the Sun. For every line, we determine an absolute value for the object and for the Sun using the fundamental parameters determined before. Afterwards, we derive the relative value for the objects by subtracting the solar absolute abundance and finally we determine the mean and standard deviation for the different lines to obtain one abundance for the object. This procedure minimizes uncertainties due to wrong atomic data, systematic errors from the model, from the data reduction, and in the measurement of the equivalent widths (given that the measurements are performed in the same way for the Sun and the other objects).

The standard deviation between the different lines for one element are a proxy for the error in the measurements of the equivalent widths, given a certain precision of the model atmospheres. For a reasonable abundance accuracy, we add the propagated uncertainties from the fundamental parameters that are gained by deriving the elemental abundances also for the extrema of the basic parameters. Here, the error in effective temperature results in a typical abundance uncertainty of 0.01 dex and therefore dominates over all other influences on the final abundance value.

The elements analyzed in this work are carbon (C), oxygen (O), Sodium (Na), magnesium (Mg), aluminum (Al), silicon (Si), Sulfur (S), calcium (Ca), scandium

(Sc), titanium (Ti), vanadium (V), chromium (Cr), manganese (Mn), Cobalt (Co), nickel (Ni), copper (Cu), zinc (Zn), yttrium (Y), zirconium (Zr), and barium (Ba). Those elements extend over a broad range in condensation temperatures (T_{cond}) from 40 K (C) up to more than 1650 K (Al, Sc, and Y). Since some lines are affected by line splitting due to hyperfine structure (HFS), we used HFS data from Porto de Mello et al. (2008, [124]). This influences the following ions: Mg I, Sc I, Sc II, V I, Mn I, Co I, Cu I, and Ba II.

As in the lithium analysis, we have to account for departures from LTE in certain lines. The oxygen triplet at 777 nm is known to be strongly affected by non-LTE line formation effects, which means the physical conditions under which those lines are formed deviate from the LTE assumption. The other possible lines in the 6300 Å region, however, are too weak to be used or severely blended. In order to account for this deviation from the LTE conditions, we apply corrections calculated by Ramirez et al. (2007, [129]). The resulting correction is somewhat larger than the one for lithium, the solar one being +0.13 dex.

The final abundances for our test case α Centauri A are given in Table 6.4.

3.5 The photospheric lithium abundance

The photospheric (or surface) lithium abundance $\log \epsilon_{Li}$ cannot be determined form the equivalent width of absorption lines, because in most cases, the line we use is too weak to be reasonably well distinguished from the noise in the surrounding area. For that reason, the whole region has to be synthesized for each star considering the basic photospheric parameters we established before as well as hyper fine splitting of the lithium line.

A 10 Å region was synthesized around the lithium doublet at 6707.8 Å (caused by the 2s-2p transition in ^{7}Li), again using *ATLAS 9* model atmospheres and *MOOG*.

λ (Å)	Element	χ_l (eV)	$\log gf$
6707.38	CN	1.83	-2.170
6707.43	Fe I	4.61	-2.283
6707.45	Sm II	0.93	-1.040
6707.46	CN	0.79	-3.012
6707.52	CN	2.17	-1.428
6707.53	CN	0.96	-1.609
6707.53	CN	2.01	-1.785
6707.56	V I	2.74	-1.530
6707.64	Cr I	4.21	-2.140
6707.74	Ce II	0.50	-3.810
6707.75	Ti I	4.05	-2.654
6707.76	Li I	0.00	-0.428
6707.77	Li I	0.00	-0.206
6707.77	Ca I	5.80	-4.015
6707.82	CN	1.21	-2.317
6707.91	Li I	0.00	-1.509
6707.91	Li I	0.00	-0.807
6707.92	Li I	0.00	-0.807
6708.03	Ti I	1.88	-2.252
6708.09	V I	1.22	-3.113
6708.13	Ti I	1.88	-2.886
6708.28	V I	1.22	-2.178
6708.38	CN	2.10	-2.252

Table 3.2: Line list for the synthesis of the lithium doublet at 6707.8 Å.

We vary $\log \epsilon_{Li}$ so that the synthesized line fits the observed one as well as possible. Since $\log \epsilon_{Li}$ is the only free parameter at this point, the situation is perfectly non-degenerate and the solution is always unique. Table 3.2 shows the lines used in the synthesis process. The atomic line data was taken from [137]. Lithium data was taken from [74].

The signal-to-noise ratio in that region is usually around 700, but almost always more than 400, which enables us to derive surface lithium abundances with an (internal) accuracy of less than 0.01 dex. This uncertainty is defined by the smallest

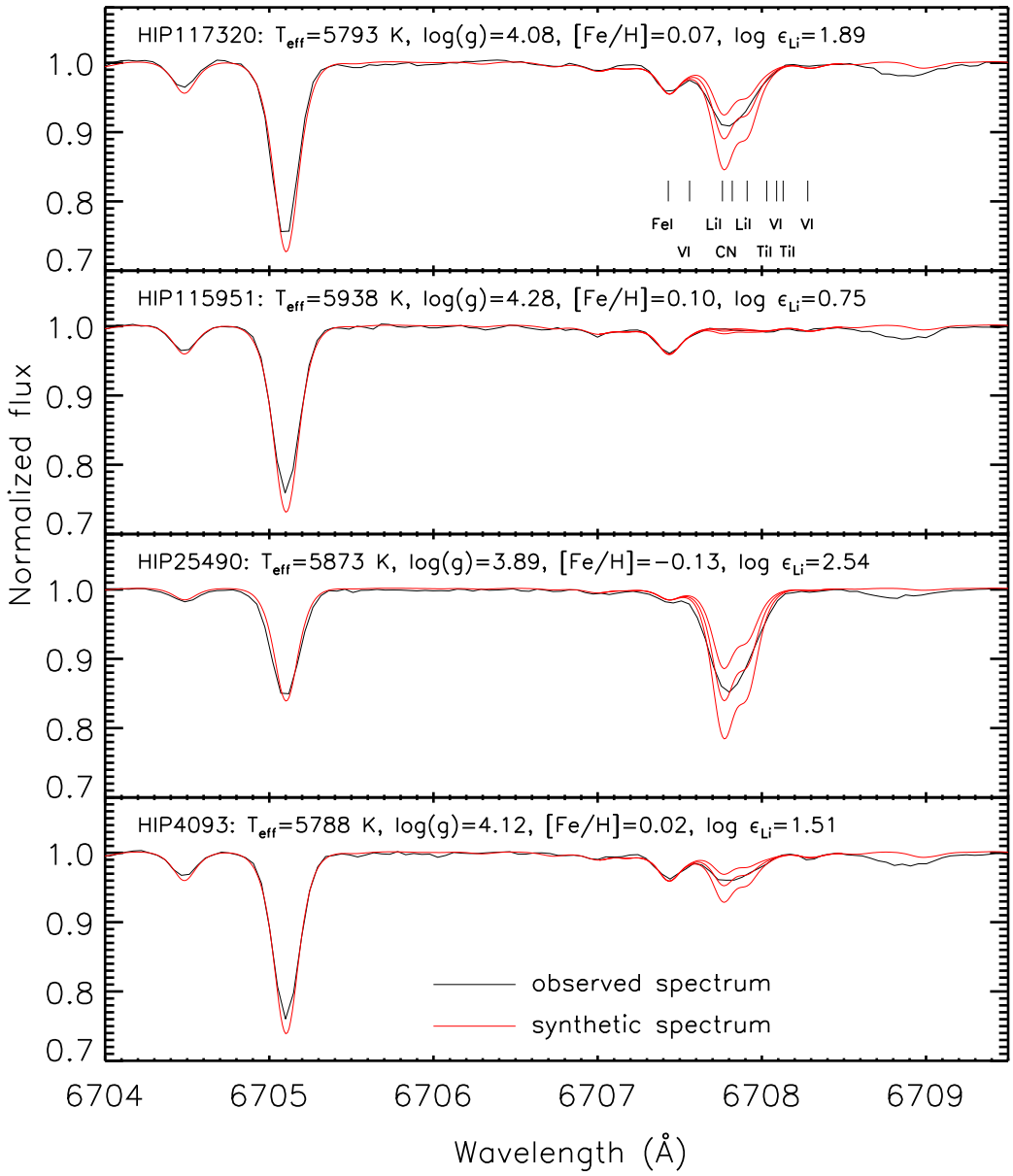

Figure 3-3: Spectrum synthesis for the determination of log ϵ_{Li} including ± 0.2 dex for 4 different objects observed with MIKE for visualization purposes. In the upper panel, the most important lines around the lithium resonance line are marked. In the HIP115951 spectra (second panel), only an upper limit could be estimated.

change in $\log \epsilon_{Li}$ that makes the synthetic line derive visibly from the best fit to the observed one. For weak lines, we are only able to derive upper limits in lithium abundance, since the line strength is of the same order as the noise level. This is typically the case for an abundance of 1.0 dex or less. Those upper limits are marked in the results with a '-1' in the uncertainty.

An error progression analysis was necessary to account for the fact that the fundamental parameters are uncertain as well. This was done by varying the input parameters by $\pm 1\sigma$ and synthesizing $\log \epsilon_{Li}$ for the changed values. The resulting uncertainty of around 0.03 dex is added to the internal one. The exact values obtained for each object are given in Chapters 4 and 5 and in the Appendix.

Figure 3-3 shows example spectra for 4 different objects. Overplotted in red are the synthesized spectra for the parameters indicated in each panel and ±0.2 dex deviations in $\log \epsilon_{Li}$ for visualization. For the object in the second panel (HIP115951), only an upper limit could be derived from the synthesis.

To account for deviations from local thermodynamic equilibrium (LTE), we applied non-LTE corrections gained from the Lind et al. grid (2009, [87]). Their grid is based on 1D *MARCS* model atmospheres[5] and cover a wide range of parameters: $T_{\rm eff} = [4000, 8000]$ K, $\log g = [1.0, 5.0]$, [Fe/H] $= [-3.0, 0.0]$, and $\log \epsilon_{Li} = [-0.3, 4.2]$. Caused by the fact that the highest metallicity in the grid is 0.0, we used an extrapolated version.

The corrections for our data reach from -0.03 dex to 0.08 dex, depending on the exact parameters of the star, but due to the small differences in fundamental characteristics in our samples mainly on the lithium line strength. The corrections results mainly from two competing effects: over-ionization and over-recombination of lithium. For most stars with an equivalent width of around 100 mÅ or less, the derived corrections are positive due to over-ionization of neutral lithium. The Li I/Li II

[5] See Gustafsson et al. 2008, [72].

ratio is smaller than the one assumed in the LTE model, therefore the lithium abundance, which is derived from Li I, is underestimated, resulting in positive non-LTE corrections. For larger values of $\log \epsilon_{Li}$, the picture turns: over-recombination starts to become dominant and the amount of Li I responsible for the resonant line is underestimated, leading to an overestimated total amount of lithium. The resulting NLTE lithium values for our solar reference objects are between 1.09 ± 0.03 and 1.07 ± 0.04 dex, which is on very good agreement with the 3D-NLTE estimate from Asplund et al. (2009, [8]).

The exact results including the corrections for each object are given in the Appendix, Tables A.1 and A.3. For a very detailed description of the non-LTE lithium line formation in cool stars, see Carlsson et al. 1994 ([23]).

Chapter 4

Lithium in solar-type stars

In the first part of this work, we wanted to examine the possible connection between lithium abundances in solar-type stars and the likelihood for those stars to host planets. My contribution to the work presented in this chapter consisted in the manual reduction of raw data and the parameter analysis for the 18 previously untreated objects, the age and mass determination and lithium abundance analysis for the whole sample, and the statistical and physical evaluation of the analysis. The results have been published in Baumann et al. (2010, [13]).

The sample we selected for this analysis consisted of objects form the following sources:

1. 105 objects from Ramírez et al. (2009, [131], 63 stars, hereafter R09) and Meléndez et al. (2009, 2010, [96, 102], 42 stars, hereafter M09). The data were taken with the RGT and MIKE spectrographs. For comparison, two stars (HIP10215 and HIP79672) are part of both samples.
2. Spectra for 12 objects obtained with HARPS were taken from the ESO archive.i HIP79672, HIP14614, and HIP42438 also occur in the first sub-sample.
3. 6 more stellar spectra come from the S^4N database ([4]). They, too, are ob-

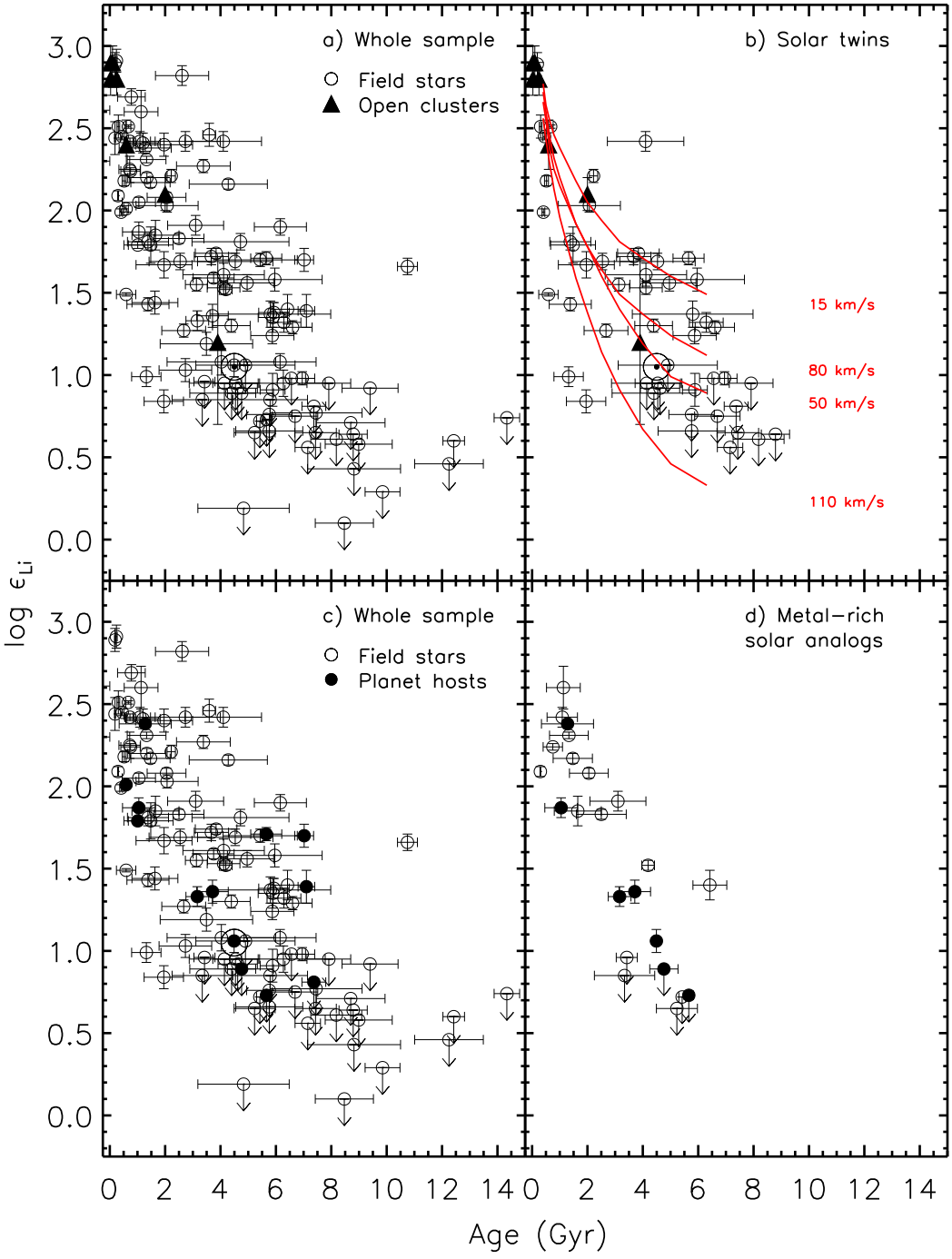

Figure 4-1: log ϵ_{Li}versus age for all stars in our sample (panels a) and c)). Panel b) shows the solar twins with overplotted depletion models from [31], panel d) depicts the metal-rich solar analogs. The Sun is plotted with the symbol $\odot$.

served with the RGT. HIP80337 is part of both the HARPS and S^4N sample.

The total number of objects in the sample is 117. For the specifications of the different instruments, see Section 2.1.

Since the spectra of the first sub-sample are analyzed in the same fashion as presented in Chapter 3, we did not re-analyze those. The spectra for the 18 additional objects were reduced as described in Chapter 2 and analyzed as in Chapter 3, using the iron line list given in Table 3.1.

Surface lithium abundances were derived for all 117 stars, using the stellar fundamental parameters from R09, M09, and the ones obtained by us. The mean uncertainty we derive for our abundances is 0.05 dex, the solar value is 1.03 ± 0.04 dex.

NLTE corrections from the Lind et al. 2009 grid were applied to the obtained lithium abundances, leading to the corrections explained in Section 3.5. The solar NLTE surface lithium abundance is 1.07 ± 0.04, in excellent agreement with the results from Asplund et al. (2009, [8]). The Detailed corrections for each star are given in row 16 in Table A.1.

4.1 Lithium and ages

Masses and ages were derived for the whole sample as explained in detail in Chapter 3, using the Y^2 isochrones. For most stars younger than about 3 Gyr, we adopted X-ray-luminosity ages or ages from gyrochronology. Some older isochrone ages with large uncertainties were replaced by activity-based ages from Saffe et al. (2005, [144] and Mamajek & Hillenbrand (2008, [93]). The method(s) used for the age determination of each star is given in Table A.1.

To our own sample, we added data for solar twins from 8 open clusters from the compilation by Sestito & Randich (2005, [154]); the data for the objects and the

Cluster	Age in Gyr	$\log \epsilon_{Li}$	$\sigma(\log \epsilon_{Li})$	[Fe/H]	Source
IC2602 & IC2391	0.03	2.9	0.1	-0.05	[134]
Pleiades	0.07	2.8	0.1	-0.03	[161]
Blanco I	0.10	2.9	0.1	+0.04	[56]
M34 (NGC1039)	0.25	2.8	0.1	+0.07	[78]
Coma Berenices	0.60	2.4	0.15	-0.05	[55]
NGC762	2.0	2.1	0.1	+0.01	[155]
M67	3.9	1.2	0.5	+0.05	[120]

Table 4.1: Ages, surface lithium abundances, and metallicities of solar twins in open clusters. The data are taken from [154], who gathered them from the given sources.

sources they were taken from are listed in Table 4.1. The mass of all twins taken into account here is $1M_{\odot}$ by definition, based on their effective temperatures and the fact that all objects in an open cluster have the same age. We add those objects because of their extremely well-known ages and masses as a comparison for our samples. Most ages for open cluster stars come from isochrone fitting as well, but the fact that all members of one cluster have the same age makes the determination very precise. For a detailed overview on the analysis of open clusters, see, e.g., [162, 154].

Figure 4-1 shows the complete sample used in this work. Open circles represent the field stars, black triangles represent the solar twins from open clusters. Downward arrows denote undetectable lithium lines, that resulted in upper limits. The solar values are marked with the symbol $\odot$. In panel b), we only plot solar twins, which we define to have solar mass and metallicity: [Fe/H] = 0.0 ± 0.1 dex, M = $(1.00 \pm 0.01)M_{\odot}$. The mass range is picked so that the twin sub-sample has a sufficiently consistent parameter range, but at the same time contains enough objects to work with it. Panels c) and d) shall be discussed later in this Chapter.

Overplotted in panel 4-1 b) are the model depletion predictions for solar-type stars from Charbonnel & Talon (2005, [31]), as discussed in Section 1.2.3. Two

things can be seen very clearly in this plot: 1) The Sun is definitely not peculiar regarding its position in the lithium versus age plane. Even though it does not have an exactly average surface lithium abundance for a star of its age, it is still perfectly normal. and 2) Our sample stars fit the model predictions very nicely. Also the solar twins from open clusters, that we added for comparison, fit both the trend of our sample objects and the predicted lithium trends from [31]. This excellent agreement between our sample and the cluster objects is very important, because the ages of young open clusters are determined very accurately, and therefore their agreement with our sample suggests that also the ages we derived are reliable. The good agreement with the models also explains the large scatter in photospheric lithium abundances in main sequence stars with the means of differences in their initial rotational velocities.

Already for the complete, unfiltered sample of solar-type stars, we receive a Spearman correlation coefficient of $\rho_{tot} = -0.61$. For the solar twins sub-sample, this value grows to $\rho_{twin} = -0.75$. The Spearman correlation coefficient is a non-parametric measure of the strength of dependency between two variables:

$$\rho = \frac{\Sigma_i (x_i - \bar{x})(y_i - \bar{y})}{\sqrt{\Sigma_i (x_i - \bar{x})^2 \Sigma_i (y_i - \bar{y})^2}} \tag{4.1}$$

where x_i and y_i are the ranks of the variables. The rank x_i is the position of elements x_j after all elements of x have been sorted in an ascending order. That way, the Spearman correlation coefficient becomes 1 (or -1), when the two variables are monotonically related, and it becomes 0, when they are perfectly statistically distributed. It is also very robust towards outliers.

4.2 Lithium in planet hosts

The work for this section is based on the findings by Israelian et al. (2009, [76], hereafter 'I09'). The principle result they presented is shown in Figure 1-3. It shows a sample of 82 solar analogs, plotted are the effective temperatures and lithium abundances the authors find in their analysis (where most the lithium abundances are taken from Sousa et al. 2008, [165]). Filled symbols stand for confirmed planet hosts, open circles are field stars for which no planets had been found at the point of publication.

The result, that can be seen very clearly in the figure, is an average lithium abundance that is higher for field stars than it is for planet hosts. The difference in the mean abundances is 0.29 dex, a factor of around 2.5. As explained in Section 1.2, the possible explanations for this phenomenon are mostly based on the long-lasting star-disk interaction in the very early stages of the host stars, that lead to increased differential rotation, which increases the lithium depletion relative to field stars without planets. Their results also include the fact, that solar-type stars with a surface lithium abundance of 1.5 dex or more are very unlikely to host planets.

We used our sample of solar-type stars to test this hypothesis, based on the stellar parameters published in I09 and ages derived by us using the exact same technique and isochrone grid as for our sample. This separate age determination is supposed to reduce the probability of systematic differences in the results.

As panels c) and d) in Figure 4-1 show, the difference between planet hosts and field stars is not as striking in our samples. Panel d) shows a sub-sample of metal-rich solar analogs. As metal-rich analogs, we define stars with [Fe/H] = 0.25 ± 0.15 and M = $(1.08 \pm 0.08)M_{\odot}$. This sub-sample is important for our analysis because, as indicated in Section 1.1.4, planet hosts are in average more metal rich than field

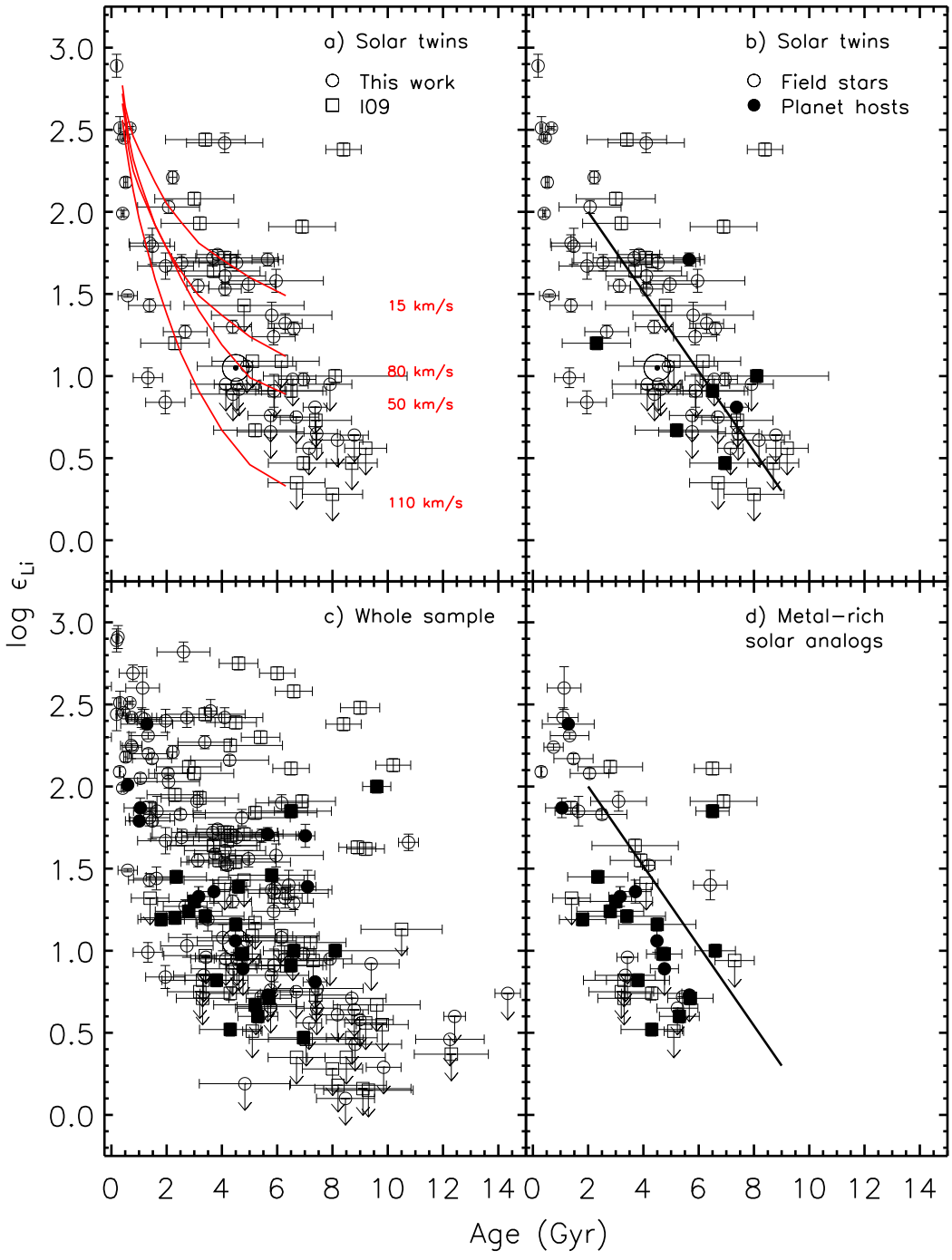

Figure 4-2: $\log \epsilon_{Li}$ versus age for all stars in our sample together with the objects from [76], (I09). The solid line in panels b) and d) are artificially added and only plotted to guide the eye.

stars without planets. This is also true for our sample. In the plot, we mark planet hosts with filled symbols, as opposed to field stars where no planets have been found (open symbols).

To statistically test the association between the planet host sample and the comparison field stars, we conducted a two-dimensional Kolmogorov-Smirnov (KS) test based on Monte-Carlo simulations to account for the uncertainties in lithium abundances and ages. That means, we pick random values from the Gaussian 1-σ environment around each value in both $\log \epsilon_{Li}$and age. Since $\log \epsilon_{Li}$ is a logarithmic quantity, we have to first convert those values to a linear scale by using $\frac{n_{Li}}{n_H} = 10^{\log \epsilon_{Li} - 12}$ instead of $\log \epsilon_{Li}$. For the objects where only upper limits could be derived, we used random values from a uniform distribution between 0 and the upper limit.

The Kolmogorov-Smirnov test estimates the likelihood that two samples follow the same distribution. It calculates the distance between the (empirically determined) distribution functions of the two samples and returns the probability for the null-hypothesis that the two samples are drawn from the same distribution. For details on the definition and the implementation, see, e.g., the very extensive series "Numerical Recipes" by Press et al., 2007 ([127]).

In order to achieve solid statistics, we used the averaged results of 1,000 KS tests each with random sets of values for every object. For the metal-rich stars of our sample, we received a probability of $64 \pm 15\%$ for the planet hosts and field stars to be sub-samples of the same sample. If we ignore the uncertainties and simply use the mean values for comparison, this probability reaches more than 80%. This fact is an important first step in the analysis of the data, because it tells us, that there is no intrinsic difference between planet hosts and field stars.

The Spearman correlation coefficient for the metal-rich solar analogs is similar

to that of the twins ($\rho_{analog} = -0.71$). The shape of the distribution, however, shows significant differences: the metal-rich analogs show an in average lower surface lithium abundance for a given age than solar twins with similar ages. This becomes most apparent in the region between 3 and 6 Gyr. This difference however does not seem to depend on the presence of planets; that means, that the age-lithium trend is strongly metallicity dependent.

This discrepancy, however, does not come surprisingly: stellar models predict such a [Fe/H] dependency based on the deeper convection zones in metal rich stars, that lead to an enhanced lithium depletion (see, e.g., [28, 42]).

For comparison, we added the data for all 82 objects presented in I09 to our data. Figure 4-2 shows the same parameter ranges for solar twins and metal-rich solar analogs as the panels of Figure 4-1, but including the data from I09. Panels a) and c) show, that both the agreement of the whole sample with our sample and the agreement of the I09 solar twins with the depletion models are excellent. this confirms, that the parameters presented in I09 (which were mostly taken from [165]) are at least on the same scale as the ones we derive for our sample; this is important to note, since it allows us to combine the two samples for the further analysis without introducing additional systematic errors.

For the 10 stars that our sample has in common with the I09 sample, our derived parameters deviate by 3 ± 20 K in effective temperature, 0.02 ± 0.04 dex in $\log g$, 0.003 ± 0.023 dex in [Fe/H], and 0.06 ± 0.11 dex in $\log \epsilon_{Li}$, where the differences in lithium abundance were only determined for the 3 star with line detection. This excellent agreement between the parameters once more confirms the consistency of the data analyses for our sample and the I09 sample.

In panels b) and d), we added an arbitrary line at the exact same position in both cases to guide the eye. It makes clear, that the metal-rich analogs are in average

more depleted in lithium than the twins. The plot also shows, that the metal-rich analogs again include more planet hosts than the twins.

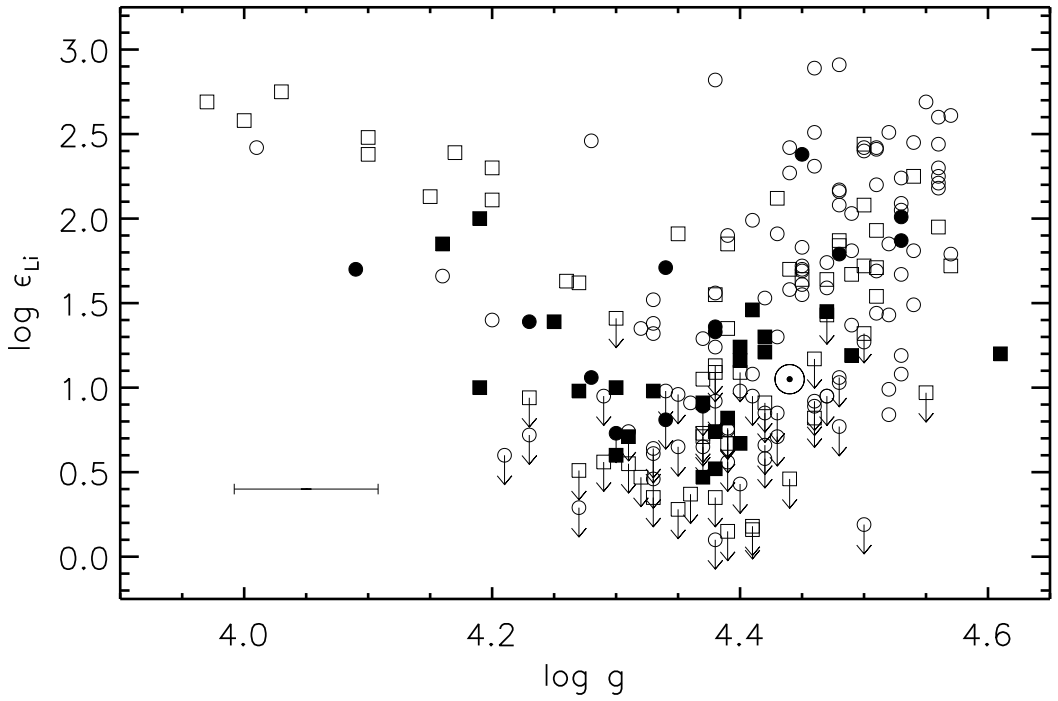

Figure 4-3: $\log \epsilon_{Li}$ versus $\log g$ for our sample and the sample from Israelian et al. (2009, [76]). The symbols are the same as in Figure 4-2, where open symbols stand for field stars and filled ones for planet hosts. The bar in the lower left of the plot represents the typical (i.e. mean) uncertainty in $\log g$.

In the complete sample (panel c)), 10 peculiar stars can be seen: they all have ages greater than 4 Gyr and a lithium abundance that is significantly higher than the average for their ages. The most obvious difference between those outliers and the main locus of objects turned out to be their surface gravity, which is around 4.1 dex and therefore significantly lower than for the rest of the solar-type stars. The outstanding position of those objects becomes even more obvious in Figure 4-3. In this figure, the main locus on the high-log g-side can be interpreted as an evolutionary track given that all objects have similar masses: lithium is decreasing

as the density decreases during the main sequence. The ascending branch below a surface gravity of 4.2 contains all the outliers from Figure 4-2, panel c) (and some others). This means, that those outliers are apparently in a different evolutionary phase. At the very least, they are not solar analogs as the rest of the objects and should not be in the analogs sample.

To exclude the possibility of systematic errors in this analysis, we compared our results for the ages, masses, and lithium abundances of those outliers with recent publications. The resulting overview for those objects is presented in Table 4.2. It shows, that the ages we derive are in reasonably good agreement with the ages derived by other groups. Only HD145809 is significantly older in our analysis compared to the literature, and therefore it would disappear into the main locus assuming the lowest value (6.9 Gyr) were true.

Object	Age (Gyr)	$M/M_{\odot}$	$\log \epsilon_{Li}$	Alternative ages (Gyr) and sources
HD221420	4.70	1.30	2.75	4.5 [119], 4.1 [184], 5.1 [140]
HD114613	6.03	1.19	2.69	5.1 [140], 5.6 [12], rot, 4.9 [184], 4.9 [140]
HD2151	6.53	1.12	2.58	5.2 [119], 5.8 [184], 6.7 [185]
HD215456	8.36	1.04	2.38	7.3 [119], 7.0 [75]
HD32724	9.07	0.97	1.63	9.9 [119]
HD4307	9.08	1.01	2.48	7.8 [189], R'_{HK}, rot, 7.4 [119], 6.4 [184]
HD78612	9.27	0.96	1.62	8.8 [119]
HD114729	9.68	0.97	2.00	10.9 [119], 6.45 [140] [planet-host]
HD145809	10.28	0.96	2.13	6.9 [189], R'_{HK}, rot, 7.9 [119], 7.4 [184]
HD32923	10.75	0.96	1.66	9.0 [184], 6.2 [189], 9.9 [119], > 9.5 [159]

Table 4.2: Ages, masses, and photospheric lithium abundances for the outliers in Figures 4-2 and 4-3. R'_{HK} denotes ages derived from chromospheric activity, rot marks those derived from rotational periods.

This very good agreement allows us to act on the assumption that the ages we derived for the I09 sample and the lithium abundances given therein are basically correct and the high-lithium envelope is therefore real, i.e., solar-type stars with a surface gravity below 4.2 dex have a higher lithium abundance than less evolved stars with similar fundamental parameters and ages.

Based on these results, we re-examined the key figure in I09 (their Figure 1, see Figure 1-3 in this work). As the figure clearly depicts, they found that stars with confirmed planets have a photospheric lithium abundance that is in average higher by a factor of 2. Moreover, almost all stars with a lithium abundance above 1.5 dex are so-called field stars, that means no planets have been found around them yet. Below this limit, planet hosts and field stars are distributed more or less equally. Note however, that the high number of upper limits makes a direct comparison rather difficult.

In order to make a more robust statement about the sample behavior, we restricted the sample to what we call a 2-σ-comparison sample. That means, we only take into account those field stars, that lie within a 2 σ environment in metallicity, surface gravity, and effective temperature of a planet host, where σ are the uncertainties presented in [165]. This restriction may seem as if forcing the objects into one distribution, but in fact, we simply force to be planet hosts and field stars to be in the same parameter space and are not influenced by the age and metallicity effects that we (and others) find. Note that we do not restrict the lithium abundances, since that is exactly the value we want to compare. This selection enables us to do a homogeneous and most importantly unbiased comparison between the sub-samples.

Figure 4-4 shows the original sample of 82 stars presented in I09, including average values for planet hosts (red dash-dotted line) and field stars (black dashed

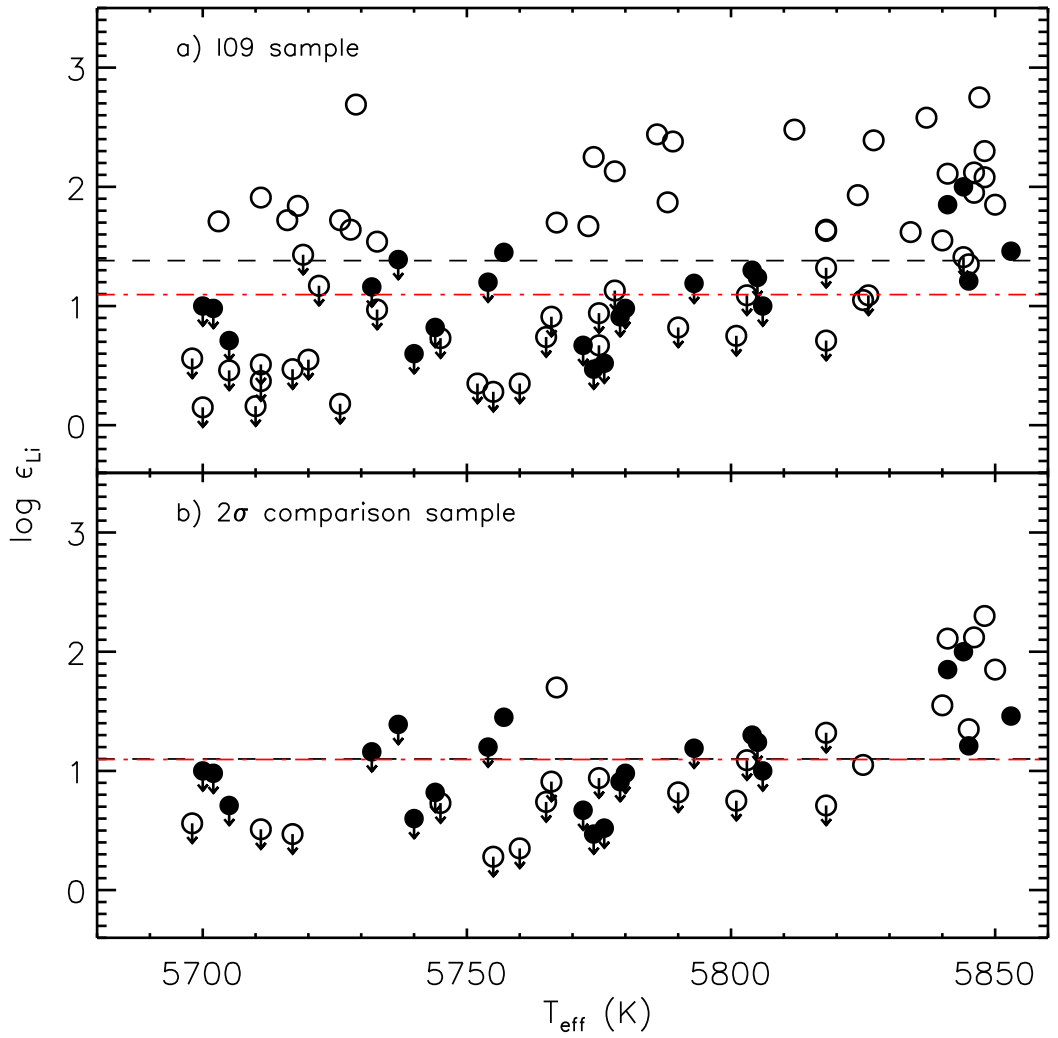

Figure 4-4: The I09 sample. Panel a) shows the complete sample as in Figure 1-3, panel b) includes only the planet hosts and the 2 σ comparison sample. The red, dash-dotted lines in both samples represent the average lithium abundance in planet host stars, the black, dashed line stands for the average of the two different comparison samples.

line). The difference between the two sub-samples amounts to 0.29 dex. In panel b), we plot the complete planet-host sample plus the 2 σ comparison group. The result is obvious: when we restrict the objects to a homogeneous sample, no difference

in surface lithium abundance can be seen. The difference of the averages has gone down to 0.005 dex, they are basically identical. It is not possible to conclude on a stronger lithium depletion in planet host stars based on this sample. Note that this comparison is based purely on the data presented in I09, there is no manipulation or addition of new parameters such as age in this case.

Regarding those results, we can identify 2 systematic biases that have lead to conclude the planet host lithium depletion presented in I09:

1. Planet host stars *are* biased towards higher metallicities, as shown in Section 1.1.4. As Figure 4-2, panels b) and d) show, metal-rich solar analogs are in general more depleted in lithium. However, this does not have to be caused by the presence of planets.
2. The I09 sample contains some outliers, that have a very high lithium abundance for stars of their ages. All of them have a surface gravity of less than 4.2, and only one of them has a confirmed planet. That makes them inappropriate for comparison with the rest of the sample.

In addition, our sample shows a shift towards higher ages for planet hosts around solar metallicity compared to field stars, which causes an enhanced lithium depletion caused by the age alone. This connection may also occur in the I09 sample, but the effect is too small to be detected. Also, finding a physical explanation for said connection would be rather difficult.

Chapter 5

Lithium in subgiants

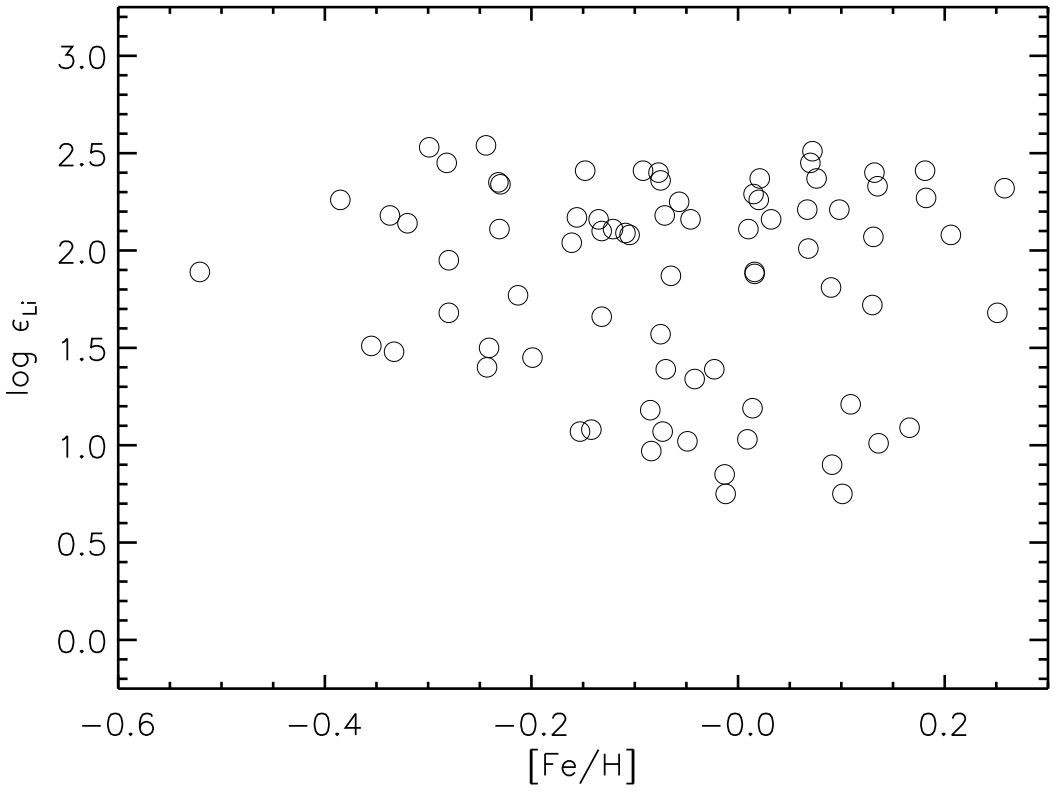

Figure 5-1: The subgiants sample in the lithium-metallicity plane.

The peculiar characteristics of the low-lithium outliers in Figure 4-2 suggests, that those objects may be stars that have evolved from the main sequence, given their lower surface gravity and otherwise solar-like parameters. By reducing the mass ranges, we see an even clearer picture: Figure 5-2 shows lithium versus age plots for three different sub-ranges in mass: below 1 solar mass, 1 to 1.1 solar masses, and above 1.1 solar masses, the typical uncertainty in mass being 0.04 $M_{\odot}$. The plotted sample contains the objects discussed in Chapter 4 as well as those from Israelian et al., 2009.

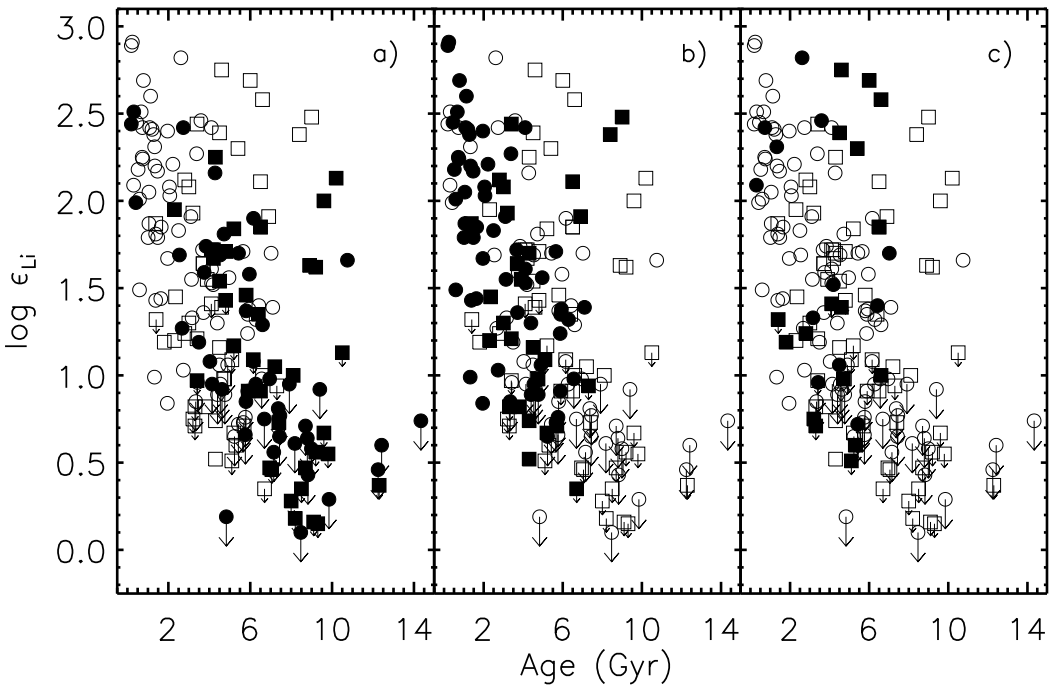

Figure 5-2: The combined objects from I09 and this work. Filled symbols denote different mass cuts: column a) M < 1.0$M_{\odot}$, b) 1.0$M_{\odot}$ ≤ M < 1.1$M_{\odot}$, and c) M ≥ $M_{\odot}$. Squares represent the I09 objects, circles stand for this work's sample.

The plots suggest that, under the assumption of consistent parameters in the sub-samples, the filled symbols in each panel can be read as evolutionary tracks: the stars steadily deplete their lithium content while they are on the main sequence

before they increase the amount of surface lithium on very short timescales as they evolve to become subgiants. Such a behavior is not predicted by any standard or extended evolutionary model.

Lithium rich subgiants have been found before, for example by Dravins et al. (1993, [45]) and Randich et al. (1999, [133]). Their studies, however, do not include a large, consistent control sample that enables objective statements about the nature of those subgiants. As I have shown in Section 4.2, this would be crucial in order to prevent misleading conclusions.

I was involved in writing the proposals and preparing the observations (including target selection), performed the actual observations at the Magellan Clay telescope (together with I. Ramírez and L. Casagrande), took part in the (automated) data reduction for the MIKE data and performed the reduction for the UVES spectra using the Gasgano interface and the ESO Common Pipeline Library (CPL)[1]. I conducted the remaining work for this Chapter largely on my own, but with great support from Martin Asplund and Iván Ramírez. The contents of this Chapter are based on a paper that is currently undergoing the finishing process.

5.1 Sample selection and analysis

Based on the unexplained peculiarity found in the low-log g objects, we created two samples of solar-type subgiant stars in order to be able to confirm (or discard) the high-lithium envelope and possibly draw conclusions about the physical reason for their presence.

The first sample consists of spectra for 36 objects from a dedicated UVES observing run (087.D-0724A, see http://archive.eso.org/). We applied for UVES observing time specifically to test the hypothesis of the presence of high lithium

[1] available at http://www.eso.org/sci/software/cpl/

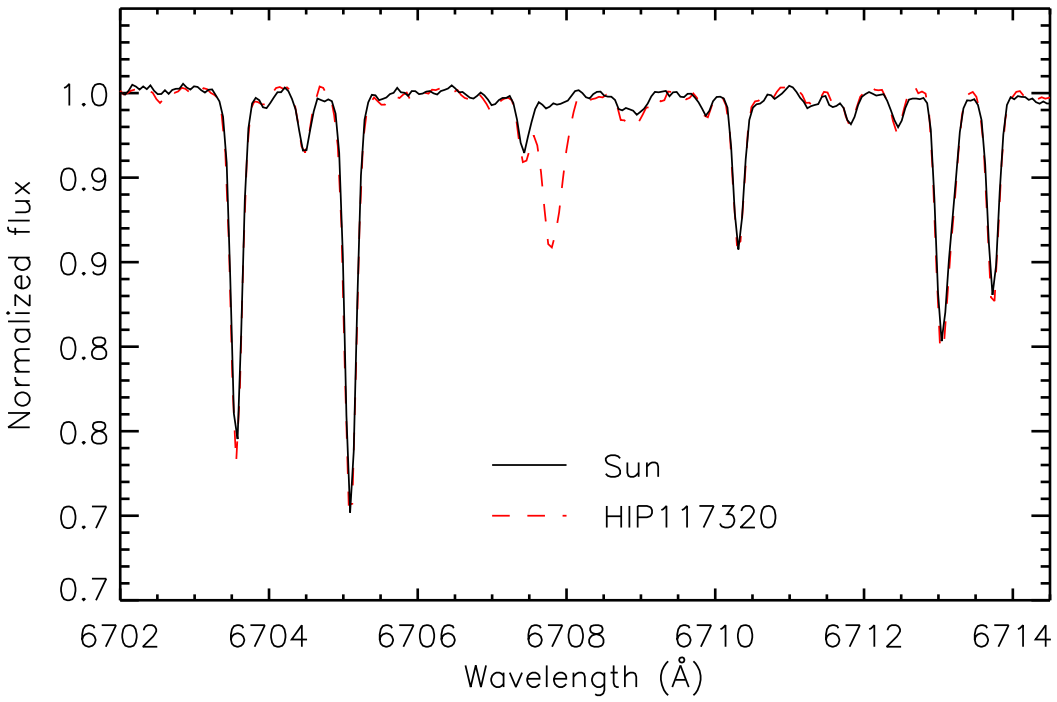

Figure 5-3: Spectra for HIP117320 and the Sun, observed with MIKE. Shown is the 6707.8 Å lithium doublet. The difference in lithium abundance is clearly visible.

subgiant stars with solar metallicities, masses, and effective temperatures. The application aimed for 25 hours of observing time during ESO period P87 (April to September 2011) to obtain spectra for 60 objects. Those objects were chosen based on their parameters published by the Geneva-Copenhagen survey (GCS, [119]). The parameter restrictions for our selection are as follows: visual magnitude V < 8, DEC < 10, RA > 10, 5600 K $< T_{eff} <$ 6050 K, -0.2 $<$ [Fe/H] < 0.2, and 3.8 $< \log g < 4.3$. The coordinate restrictions are based on the fact that the observations were to take place in the Chilean summer. 36 of the objects we obtained spectra for were used in the further analysis. The selection leading to this reduced number was caused by the high demands for quality of the data as well as the exact parameters we determined for them.

To those 36 objects, we added data for another 40 subgiant stars obtained in ob-

serving runs with MIKE at the Magellan Clay telescope in January and June 2011. The observations conducted by myself together with two co-workers where part of a MIKE program aiming for solar-type stars for extensive abundance analyses (see Chapter 6). Both datasets contain asteroid spectra for every night as solar references as explained in Section 2.1.

As an example, Figure 5-3 shows a detail of the reduced spectra for the Sun (from the asteroid Iris) and HIP117320 to visualize the extremely high quality of the obtained data. Both spectra agree very well, but the difference in the lithium line is apparent. Even though degenerate parameters are possible given that the plotted example region is very small, it already suggests very similar parameters in the two objects but a much larger photospheric lithium abundance in HIP117320. Indeed, the fundamental parameters we obtain for this object are very close to solar: $T_{\rm eff}$= 5793 ± 86 K, $\log g$ = 4.08 ± 0.160, [Fe/H] = 0.068 ± 0.054, and $\log \epsilon_{Li}$= 1.89 ± 0.05. Our mass for this star is $1.07^{1.19}_{1.01}M_{\odot}$. Naturally, the surface gravity is clearly sub-solar, since the low $\log g$ was one of the criteria by which we chose the sample objects.

The UVES data were made available by ESO in a reduced form (but re-reduced by us to maximize the quality of the final data), the MIKE data were reduced by us using the MIKE pipeline. The whole sample was analyzed in the same fashion as the solar-type stars in Section 4.1. For the characteristics of the data from the two instruments, see Section 2.1. We determined photospheric lithium abundances by line synthesis and corrected for NLTE effects using the correction grid by Lind et al. (2009, [87]).

Isochrone fitting was especially crucial for this sample. For a deeper understanding of possible systematics trends of low lithium stars, it is important to confirm that those stars really have evolved from the main sequence. For most ob-

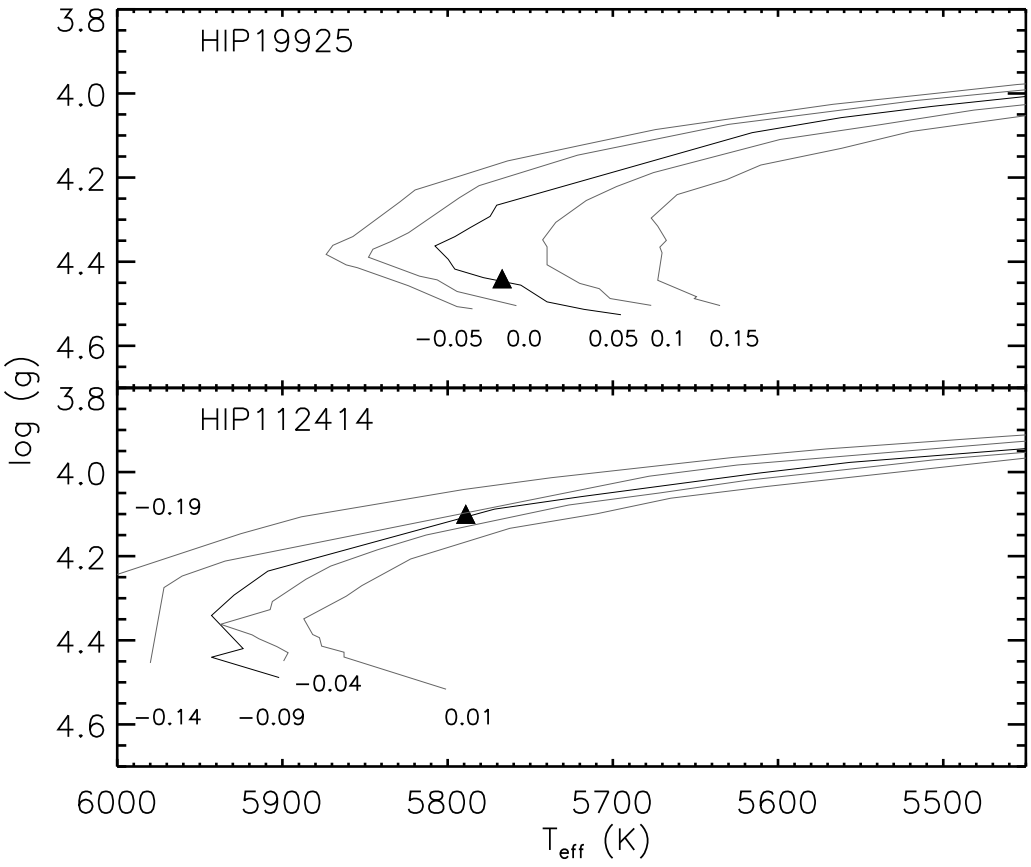

Figure 5-4: Visualization of the determination of evolutionary state for 2 objects, HIP19925 and HIP112414 for a stellar mass of 1.01 solar masses. Also included are evolutionary tracks for deviating metallicities (gray).

jects, the position in the HR diagram in combination with the evolutionary tracks allows a precise determination of the evolutionary state the star is in, given its fundamental parameters are accurate. Figure 5-4 shows two examples, HIP19925 and HIP112414, on the $T_{\rm eff}$-log g plane, with overplotted isochrones for their exact basic parameters (black lines) and deviations in metallicities (gray lines, the [Fe/H] for each track is printed at the bottom of the lines.). It is clear, that the first object is still in its main sequence phase, whereas the second one has evolved onto the subgiant branch.

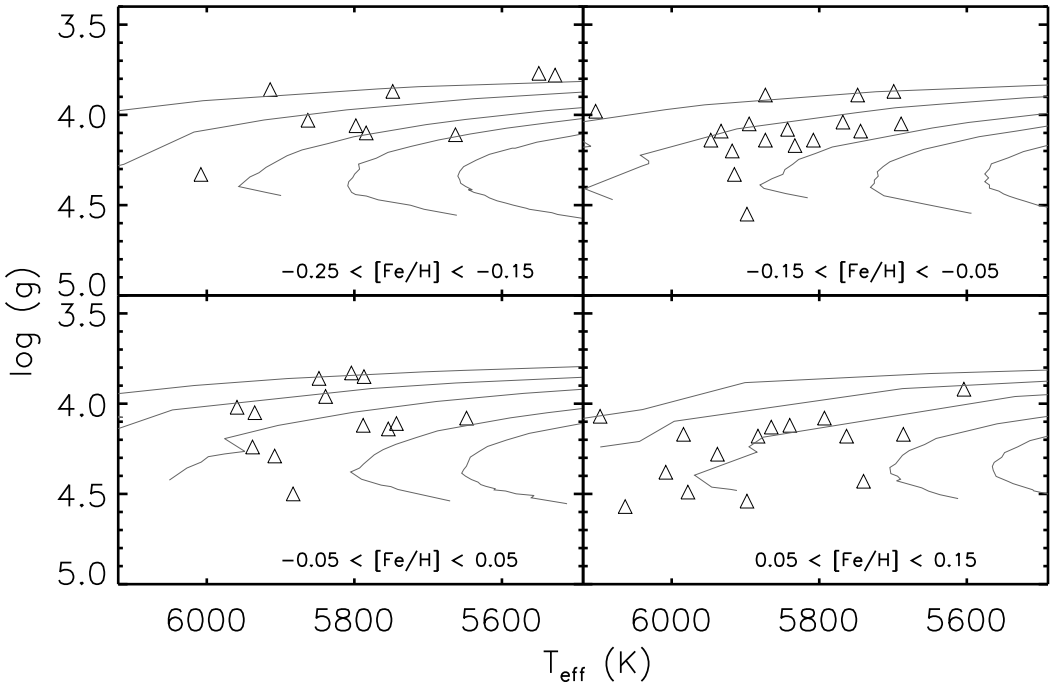

Figure 5-5: Evolutionary tracks for different masses and metallicities. Plotted are the tracks for the centers of the indicated metallicity regions and for 5 different masses: in the top panels, the masses are 0.9, 0.95, 1.0, 1.1, and 1.2 $M_{\odot}$, in the bottom panels, the masses are 0.95, 1.0, 1.1, 1.2, and 1.3 $M_{\odot}$. Overplotted are the sample objects that fall into the indicated metallicity and mass ranges.

In Figure 5-5, all sample objects with metallicities between -0.25 and +0.15 and masses between 0.9 and 1.2 $M_{\odot}$ (1.3 $M_{\odot}$ in the lower panels) are plotted over evolutionary tracks. Those tracks are calculated for the central [Fe/H] indicated in the panels and for different masses: the upper panel shows 0.9, 0.95, 1.0, 1.1, and 1.2 $M_{\odot}$, in the bottom panels, the masses are 0.95, 1.0, 1.1, 1.2, and 1.3 $M_{\odot}$. The parameter selection for the tracks is completely arbitrarily adjusted to the number of objects in the parameter region. Note that this whole plot is only there to visualize the fact, that most of our objects really are evolved stars and have left the main sequence. The plot also shows, that there is a slight metallicity dependence of the surface gravity: more metal-rich stars tend to be more dense than metal-poor ones.

Figure 5-1 at the beginning of this Chapter shows, that the photospheric lithium abundance in this sample does not depend significantly on [Fe/H]. The upper envelope appears to be nearly constant with metallicity.

We conducted the type of plot presented in Figure 5-4 for all objects from the subgiant sample and deduced that almost all stars with a surface gravity of around 4.1 or lower really have evolved from the main sequence. We also checked the evolutionary tracks for the outliers from Chapter 4 and found that all of them really are subgiants that have left the main sequence.

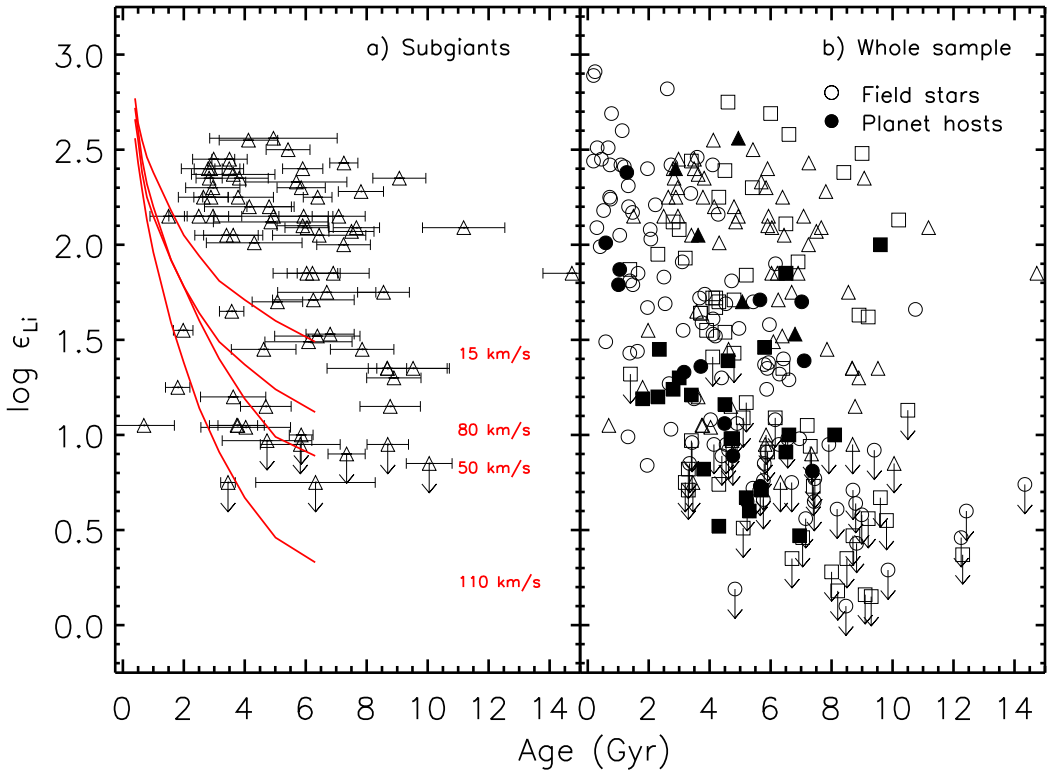

Figure 5-6: Lithium versus age as in Figure 4-1. The red lines in the left panel are the lithium depletion predictions from Charbonnel & Talon (2005, [31]), as in Figure 1-2. The right panel shows all objects from Chapters 4 and 5, with the following key: circles represent the solar-type stars from this work, squares are the I09 objects, and triangles stand for the subgiants presented in this chapter.

HIP49024 is the only object that is part of both observational samples. The parameters resulting from our analysis are presented in Table 5.1.

Sample	T_{eff}(K)	log g	[Fe/H]
MIKE	5933 ± 84	4.09 ± 0.16	−0.121 ± 0.055
UVES	5947 ± 65	4.14 ± 0.11	−0.057 ± 0.048
	log ϵ_{Li}(NLTE)	Age (Gyr)	Mass ($M_\odot$)
MIKE	2.10 ± 0.05	$6.67^{7.79}_{4.77}$	$1.052^{1.174}_{1.015}$
UVES	2.25 ± 0.05	$6.45^{7.16}_{5.05}$	$1.079^{1.148}_{1.045}$

Table 5.1: The fundamental parameters for HIP49024, the only object being part of both the MIKE and the UVES sample.

All fundamental parameters agree very well and are identical within the errors. Only the metallicities (for which the error ranges still overlap) show larger differences. This might be the reason, why the lithium abundances do not agree well, even though their errors are small. Note that even if this sort of uncertainty would be true for all objects of the sample, it would barely change the overall picture, since the difference in log ϵ_{Li} is still small compared to the abundance ranges of the whole sample.

5.2 Results

Figure 5-6 shows the result of this analysis: in panel a), we plot the subgiant stars together with the lithium depletion predictions for solar-type stars from Charbonnel & Talon (2005, [31]). Already from the plot it is evident, that the new objects are definitely more lithium-rich than the solar-type stars presented in Section 4.2. Indeed the average lithium abundance for this sample is 1.89 ± 0.46 dex, with an average age of 5.37 ± 2.40 Gyr. In the solar-type sample, the average lithium abundance is 1.03 ± 0.04 dex, and the average age 4.2 ± 3.0 Gyr. That means the average log ϵ_{Li} is

almost 8 times higher in the subgiant sample even though the age is slightly higher, too. Masses, metallicities, and temperatures in the subgiant sample lie around the solar values, as demanded: M = $(1.10 \pm 0.13)M_{\odot}$, [Fe/H] = -0.06 ± 0.16, and T_{eff} = (5839 ± 135) K. The average surface gravity on the other hand is sub-solar: $\log g = 4.08 \pm 0.28$.

The difference in parameters between the two samples can also be measured by statistical means: conducting the Kolmogorov-Smirnov test as described for the solar-type stars, again using a Monte Carlo simulation to pick 1,000 random sets of parameters within each object's 1 σ environment, we obtain a probability for the two samples of solar-type stars and subgiants being part of one sample of only 10^{-6}.

The in average higher lithium abundance in the subgiant sample is as expected (and was even visible for many stars in the raw data during observations due to the strong lithium line, see Figure 2-1). However, as panel b) in Figure 5-6 shows, the gap between the main locus and the low-$\log g$ objects disappears. In this Figure, circles stand for the solar-type stars presented in Section 4.2, squares are the added objects from I09, and triangles represent the newly added subgiants discussed in this section. Filled symbols depict known planet hosts and open ones are field stars for which no planets have been found so far. In the subgiant sample, only 5 out of 76 objects are confirmed planet hosts: HIP115697, HIP24681, HIP26380, HIP30114, and HIP42030. The planet information was taken from http://exoplanets.org/table/. This percentage is lower than in the solar-type sample (6.5% instead of 12.0%), but the difference is not significant and could as well be explained by the higher number of followed stars in the solar-type group.

Even though the large gap that was clearly visible in the solar analogs sample disappears with the extension of the sample, a strong deviation from solar-type behavior remains within the subgiants. This is not too surprising, given the fact that

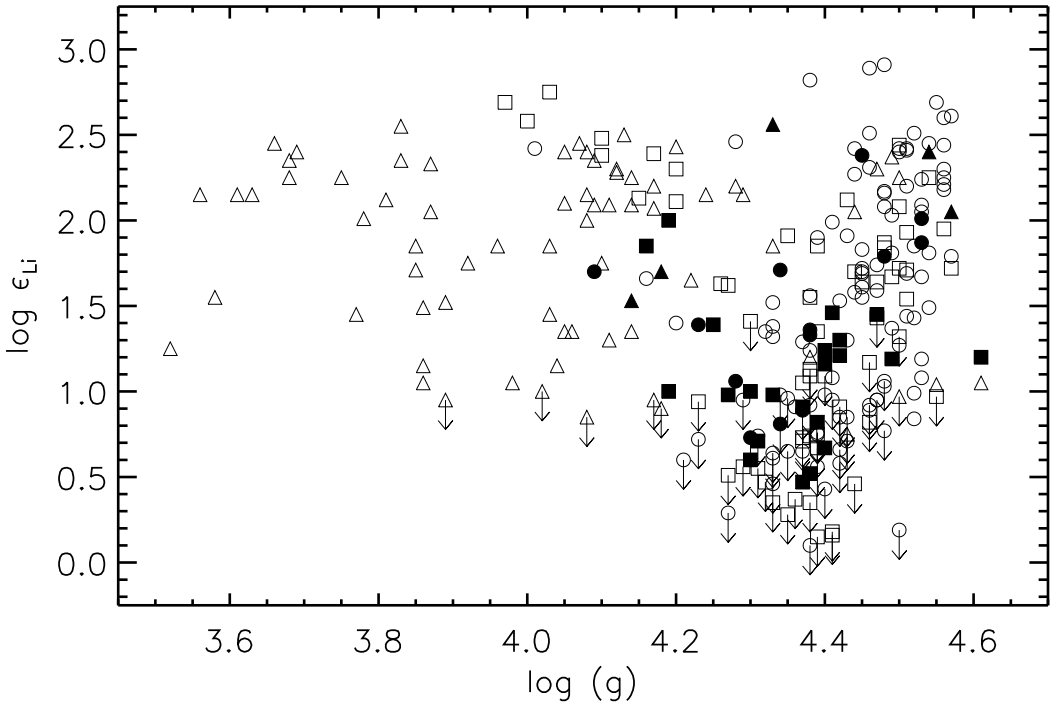

Figure 5-7: $\log \epsilon_{Li}$ versus $\log g$ for the solar analog sample, the subgiants, and the objects from I09. Again, filled symbols stand for known planet hosts, open ones for field stars. The errors in $\log g$ are similar to the ones in Figure 4-3.

lithium is well-known to be extremely sensitive to even minor changes in the environmental parameters. Figure 5-7 shows the same age effect that appeared in Figure 4-3. In this extended sample however, a similar effect as in the $\log \epsilon_{Li}$-age plot can be seen, but the trends that were clear in the solar analog sample wash out with the addition of a large number of subgiants. The field of main sequence stars that deplete their lithium with decreasing surface gravity is still the main accumulation, but the increasing branch at the end of the main sequence is becoming fainter. It is, however, still obvious that the lithium abundance is increasing again below a surface gravity of around 4.3, which is also supported by the fact that the number of upper limits drops below that point.

Figure 5-8 shows photospheric lithium abundance versus age using the same

mass cuts as in Figure 5-2 at the beginning of this Chapter, but including the new subgiant objects. The hook-shaped cuts in the original Figure, that lead to the suggestion of interpreting them as evolutionary tracks, are still clearly visible here. As expected, the more massive stars are in average younger than the lighter ones. Also within the mass cuts, the added subgiants fill the gap between the original subgiants and the main sequence stars of the same mass range.

The fact that the photospheric lithium abundance indeed seems to be increasing at the end of the main sequence remains hard to explain, but the disappearance of the gap between the main locus and the subgiants does make it easier to look for physical reasons. As explained in Section 1.2, temperatures at the bottom of the convection zone are not hot enough to actually burn lithium in solar-type stars without extra mixing by e.g. convective overshooting. That could make it possible for lithium to sediment below the convection zone without or with only little depletion. When the convection zone deepens at the end of the main sequence, the photosphere will get enriched with the material that has been stored at the bottom. The amount of actual enhancement will be extremely sensitive to even the slightest parameter variations, which is why one would expect a continuous enhancement rather than a clear gap as seen in Figure 4-2. That means, even though the results of the subgiant sample analysis do not reproduce the distribution gap that originally lead to the detailed study, exactly this disappearance of the gap makes a dredge-up scenario a lot more plausible.

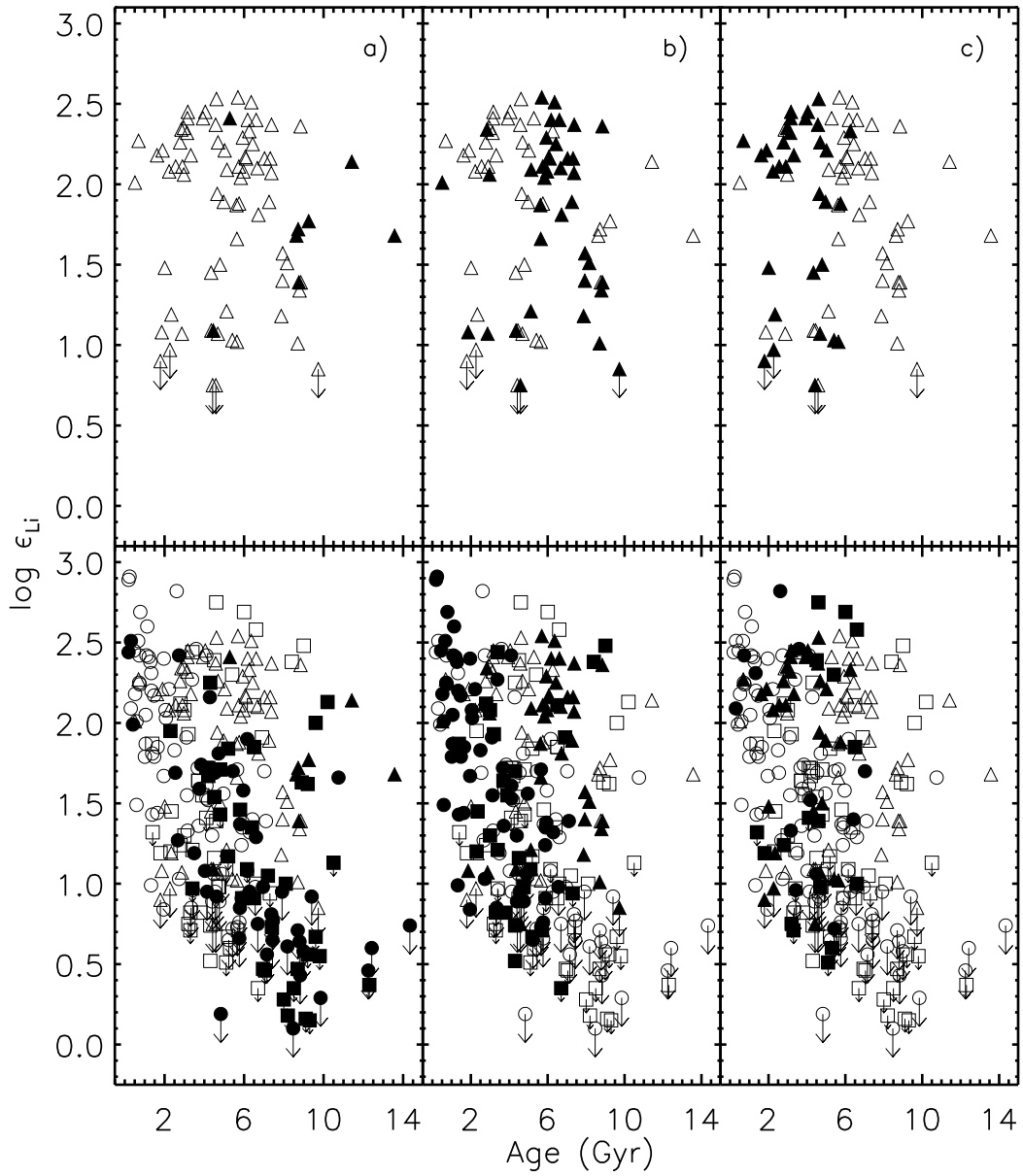

Figure 5-8: The combined solar-type and subgiant stars. Filled symbols denote different mass cuts: a) M < 1.0$M_{\odot}$, b) 1.0$M_{\odot}$ ≤ M < 1.1$M_{\odot}$, and c) M ≥ $M_{\odot}$. Squares represent the I09 objects, circles stand for this work's solar-type stars, and triangles for the subgiants discussed in this Chapter.

The main results of the subgiants analysis are the following:

1. Solar-type subgiants are in average more lithium rich than main-sequence stars of similar age.
2. The gap in lithium abundances between the main locus and the subgiants appears as a continuous transition with the addition of the new subgiants.
3. The mass cuts in the log ϵ_{Li}-age plane, that can be interpreted as evolutionary tracks, suggest an increase of the surface lithium abundance at the end of the main sequence.
4. A dredge-up scenario for lithium at the end of the main sequence seems to be a possible explanation given a continuous transition between the main sequence stars and the subgiants.

Chapter 6

α Centauri A

In order to test the results presented in Section 1.1.4, we gathered data for an extended sample of solar-type objects with UVES and MIKE. Before being able to analyze the whole sample however, we decided to examine one well-known object as a test case: α Centauri A. Due to difficulties with the reduction of the α Centauri A data, I was not able to finish the analysis of the whole sample for this work, which is why I only present the results for the test case here.

The results for α Centauri A are also going to be published in a separate paper that is currently in the pipeline. The parameter and abundance analyses presented here as well as the evaluation and comparison were done by myself, with great support from Martin Asplund, Iván Ramírez, and Jorge Meléndez, especially during may stays in the USA, Brazil, and Australia in the course of this work, but also remotely.

6.1 Data and analysis

α Centauri A (HD128620) is one of the best-known objects in the galaxy, equipped with the great advantages of being part of the system closest to the Sun (the α Centauri triple system with α Centauri C being the closest star to the Sun) and itself being the fourth-brightest star in the the sky (visual magnitude of -0.01, according to the *SIMBAD* catalog[1]). Furthermore, α Centauri A itself is solar-type (spectral type G2V), which makes it a prime candidate for comparative studies. Also its mass is extremely well known thanks to the fact that it has a companion, which makes the mass determination independent of models as would be the case for isochrone fitting. Pourbaix et al (2002, [125]) and Torres et al. (2010, [182]) publish a mass of $M_A = (1.105 \pm 0.007)M_\odot$.

Accurate fundamental parameters for α Centauri A are of great interest because, as with the Sun, they allow the calibration of theoretical models for stellar atmospheres and isochrones. α Centauri A is also very intriguing in the context of our work, especially in the light of the planet signature findings by Meléndez et al. and Ramírez et al.. Because of its outstanding characteristics, it is object of several planet searches. The fact that no planet has been found around α Centauri A so far actually increases the probability for the presence of rocky, Earth-sized planets. This can be explained with the statistics in the Kepler data (see [86]): massive planets, i.e. planets with 5 Earth masses or more, are mostly single planets. This is most likely due to the fact that giant planets can distort the orbit of smaller planets much easier and, should an Earth-sized planets have built, possibly lead to its destruction. The age of α Centauri A is a bit more uncertain: Eggenberger et al. (2004, [50] determine 6.53 Gyr, it is 5 Gyr according to [124], Miglio & Montalbán (2012,

[1] http://simbad.u-strasbg.fr/simbad/sim-fbasic

[106]) obtain ages between 5.4 and 8.9 Gyr, depending on the models they fit to the observable parameters. But α Centauri A is definitely old enough so a gas giant would have had enough time to clean other orbits around α Centauri A.

Also apart from the denoted ages, the parameters published for α Centauri A do not always agree, as is the case for most reference stars. In Table 6.1, we present a selection of publications on α Centauri A. Note that this selection is meant to be a historical comparison rather than a compilation of state-of-the-art results. A comparison of most of the presented values would be extremely difficult, since they are obtained using different methods, models, and assumptions.

For our own analysis of α Centauri A, we used spectra from the MIKE and HARPS spectrographs. The MIKE data were taken as a part of the subgiants observing runs in 2011, whereas the HARPS data were once more taken from the ESO archive. Those spectra are part of an asteroseismological analysis by Bazot et al. (2007, [14]), where 4959 spectra were taken with the HARPS spectrograph[2]. Exposure times between 2 and 15 seconds were used leading to a S/N ratio of 300 to 450 per pixel in the relevant regions.

The fundamental stellar parameters effective temperature, surface gravity, and metallicity were obtained from both sets of spectra separately using the methods described in Section 3.3. The results from this analysis are given in the first 2 lines of Table 6.2. The exact spectral lines that where used and the measured equivalent widths for each are presented in Table A.4 in the Appendix.

In order to gain a higher reliability for the effective temperature, we added results from two more methods, that are independent of the one explained before: color-temperature calibration based on the infrared flux method (IRFM) temperature scale by Casagrande et al (2011, [25], available at http://vizier.u-strasbg.fr/viz-bin/VizieR) and line synthesis of the Hα line at 6563 Å as explained in [11, 29].

[2]The data are available at the ESO archive under program ID 075.D-0800(A)

T_{eff} (K)	log g	[Fe/H]	Source
5770	-	+0.22	[57]
5727	4.38	+0.29	[52]
5820	4.25	-0.01	[19]
5793	4.4	+0.17	[135]
5793	4.4	+0.20	[157]
5770	-	-	[160]
5750	4.38	+0.11	[69]
5793	4.5	+0.20	[1]
5727	4.42	+0.20	[48]
5727	4.27	+0.10	[59]
5800	4.31	+0.22	[35]
5720	4.27	+0.15	[49]
5830	4.34	+0.25	[113]
5519	4.26	+0.12	[4]
5784	4.28	+0.12	[44]
5813	4.30	+0.26	[39]
5844	4.30	+0.28	[147]
5801	4.33	+0.21	[184]
5801	4.38	+0.31	[129]
5847	4.34	+0.24	[124]
5855	4.32	+0.23	[96]
5745	4.32	+0.22	[22]
5809	4.32	+0.23	Ramírez et al., in prep.
5801	4.44	+0.201	This Work (MIKE)
5812	4.28	+0.205	This Work (HARPS)
5788 ± 40	4.34 ± 0.06	+0.21 ± 0.05	Average

Table 6.1: Basic parameters from selected publications on α Centauri A and the average of all publications. In the average, we exclude the results from [4], since their T_{eff} is much smaller than that from the other publications and would bias the average.

IRFM is only based on photometry and depends on the metallicity of the object. The Hα method depends on both surface gravity and metallicity, but the sensitivity to those parameters is very small: an increase of 0.1 dex in metallicity results in an increase of less than 5 K in temperature, while an increase of 0.1 dex in sur-

Method	T_{eff}(K)	[Fe/H]	log g
Spectroscopy (MIKE)	5801 ± 40	0.201 ± 0.05	4.44 ± 0.10
Spectroscopy (HARPS)	5812 ± 50	0.205 ± 0.04	4.28 ± 0.10
Infrared Flux	5772	-	-
Hα line synth. (MIKE)	5838 ± 100	-	-
Hα line synth. (HARPS)	5807 ± 100	-	-

Table 6.2: Fundamental stellar parameters for α Centauri A obtained with different methods. IRFM results were taken from [24].

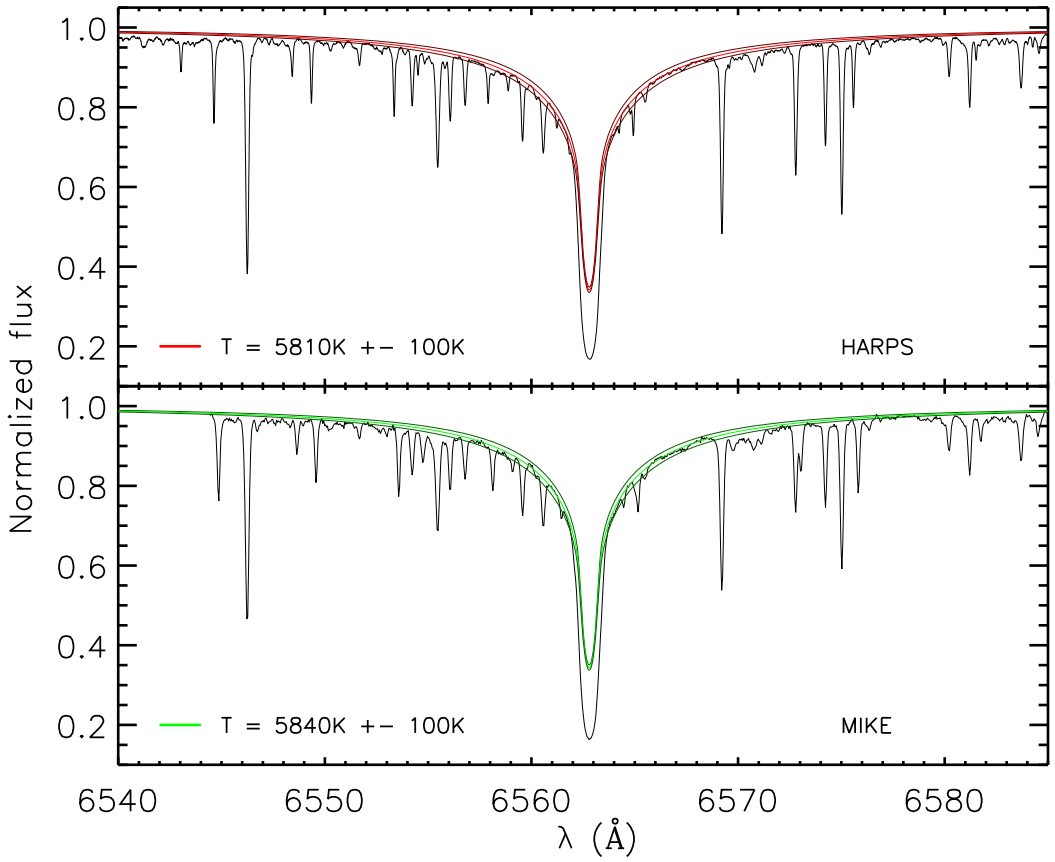

Figure 6-1: Fitting of the Hα line wings for the α Centauri A data from HARPS and MIKE. Plotted in each panel are the best fits and the ± 100 K deviations for comparison (in darker colors).

face gravity leads to a decrease of some 10 K. The grid for the Hα line fitting was calculated by Barklem et al. (2002, [11]), but is used here with an increased resolution: the steps in temperature, metallicity, and gravity are 10 K, 0.05 dex, and 0.05 dex, respectively. The results for those two temperature determinations are given in Table 6.2. Figure 6-1 shows the Hα line from the HARPS and the MIKE data together with the best fit. The darker lines are the 100 K deviations from the best fit, for comparison. We use a surface gravity of 4.36 dex, which is the average of the MIKE and HARPS results, and a metallicity of 0.20 dex. The uncertainty is a rough estimate depicting the noise of the spectra, possible systematic errors of the method, and the uncertainties in metallicity and surface gravity. The Hα analysis presented here was conducted by Deysi Cornejo at the Agencia Aspacial del Perú based on the abovementioned parameters.

Also in Table 6.1, some results are obtained with model-independent methods. The effective temperature can be retrieved from the object's angular diameter and its bolometric flux using the equation $f_{bol} = \frac{\Theta^2}{4}\sigma T_{eff}^4$, where σ is the Stefan-Boltzmann constant. For a detailed description, see e.g. [130], where a temperature of 5771±23 K is obtained for α Centauri A. The surface gravity on the other hand can also be determined using Hipparcos parallaxes as in [124], where a gravity of 4.31 ± 0.005 is reported.

The basic parameters presented in Table 6.2 show an overall consistent behavior. Effective temperatures and metallicities agree within the errors, surface gravities differ by 0.16 dex, but their error ranges overlap as well (MIKE: (4.44 ± 0.10) dex, HARPS: (4.28 ± 0.10) dex). However, those small differences can propagate as the example of HIP49024 in Chapter 5 showed. For this reason, we decided to treat the two datasets completely separately and compare the obtained results in the end of the process.

Photometric abundances for 20 elements in α Centauri A were determined using both sets of spectra completely independently. Equivalent widths were used with the aid of *MOOG* and *ATLAS 9* model atmospheres, as explained in Section 3.3. For each line of every element, relative abundances were determined using the solar comparison spectra from asteroid observations. We applied corrections for the deviations of the LTE assumption for the Oxygen triplet as explained in [129] and Chapter 3. Hyper-fine structure data for Mg I, Sc I, Sc II, V I, Mn I, Co I, Cu I, and Ba II were taken from [124], who imported data from [168]. Del Peloso et al. (2005, [39]) show, that the differences between corrections taken from various sources are negligible compared to their aftermath, especially for solar-type stars, which is why we can rely on the corrections we obtained from one source only. This should also minimize the chances of systematic differences between results from various works.

Since α Centauri A has a super-solar metallicity, galactic chemical evolution does influence the abundances for certain elements. In order to still be able to compare its composition with the solar one, we have to correct for evolution effects. To estimate the impact of galactic chemical evolution, the standard procedure is to plot the chemical abundances for each element in a sample of stars versus their metallicities and use the upper envelope of the distribution as an approximation for the growth of this element's photospheric abundance with metallicity. This result has than to be compared with theoretical predictions (e.g., [49, 95, 17]). The GCE corrections we derive are given in Table 6.3.

The final results of this analysis including the measured equivalent widths are given in Tables 6.4 and A.4. The abundances we present for each element are the mean of the elements' line-by-line relative abundances and the respective uncertainties. The basis of those uncertainties is the standard error of the mean ($\frac{s}{\sqrt{n}}$). To this value, we add the propagated uncertainties from the errors in the fundamental

Element	correction
C	0
O	-0.43
Na	0.39
Mg	0
Al	0
Si	0.33
S	0
Ca	0
Sc	-0.24
Ti	0
V	0
Cr	0
Mn	0.51
Co	0.37
Ni	0.54
Cu	0.54
Zn	0
Y	-0.18
Zr	-0.53
Ba	-0.14

Table 6.3: Corrections for galactic chemical evolution applied to the abundances obtained for α Centauri A.

Element	T_{cond} (K)	$[X/Fe]_{MIKE}$	N_{lines}	$[X/Fe]_{HARPS}$	N_{lines}
C	40	0.022 ± 0.019	5	0.029 ± 0.019	2
O	180	0.042 ± 0.026	3	N/A	0
Na	958	0.048 ± 0.020	3	0.037 ± 0.018	4
Mg	1336	0.004 ± 0.024	3	0.015 ± 0.023	4
Al	1653	0.014 ± 0.025	5	0.022 ± 0.015	3
Si	1310	0.022 ± 0.018	28	0.027 ± 0.021	22
S	664	−0.001 ± 0.021	4	0.020 ± 0.020	5
Ca	1517	0.022 ± 0.023	15	0.036 ± 0.024	16
Sc	1659	0.016 ± 0.028	13	−0.005 ± 0.018	13
Ti	1582	−0.002 ± 0.021	61	−0.011 ± 0.018	88
V	1429	−0.021 ± 0.022	20	−0.030 ± 0.021	19
Cr	1296	0.011 ± 0.021	35	0.011 ± 0.018	54
Mn	1158	−0.025 ± 0.012	6	−0.043 ± 0.023	7
Co	1352	−0.027 ± 0.025	14	−0.020 ± 0.026	16
Ni	1353	−0.007 ± 0.016	35	−0.007 ± 0.017	73
Cu	1037	0.005 ± 0.046	3	0.015 ± 0.035	3
Zn	726	0.024 ± 0.012	1	0.038 ± 0.017	3
Y	1659	−0.030 ± 0.023	4	−0.032 ± 0.024	5
Zr	1741	−0.007 ± 0.009	1	0.006 ± 0.013	1
Ba	1455	−0.053 ± 0.023	2	−0.079 ± 0.023	3

Table 6.4: Abundances obtained for α Centauri A from the MIKE and HARPS data. N_{lines} gives the number of lines used for the respective abundance.

parameters. Ideally, one would have to estimate the uncertainty of the equivalent width measurements. But, since α Centauri A is a solar-type star, we can assume that the line formation models reproduce reality precisely, and therefore, the standard error of the mean represents exactly the deviations in the line measurements. However, the propagated errors caused by the effective temperature uncertainties are of the order of 0.01 dex and therefore dominate over all other error sources.

Element	$[X/Fe]_{M09}$	N_{lines}	$[X/Fe]_{average}$
C	−0.008 ± 0.041	4	0.014 ± 0.020
O	−0.011 ± 0.033	3	0.016 ± 0.037
Na	0.040 ± 0.067	2	0.042 ± 0.006
Mg	−0.017 ± 0.038	3	0.001 ± 0.016
Al	0.056 ± 0.054	4	0.031 ± 0.022
Si	−0.011 ± 0.013	11	0.013 ± 0.021
S	−0.004 ± 0.044	4	0.006 ± 0.013
Ca	−0.009 ± 0.017	9	0.016 ± 0.023
Sc	0.037 ± 0.039	3	0.016 ± 0.021
Ti	0.001 ± 0.025	8	−0.003 ± 0.007
V	0.031 ± 0.016	6	0.007 ± 0.033
Cr	0.017 ± 0.015	7	0.013 ± 0.003
Mn	−0.031 ± 0.013	3	−0.016 ± 0.036
Co	0.016 ± 0.030	5	0.008 ± 0.025
Ni	−0.007 ± 0.014	9	−0.002 ± 0.008
Cu	−0.007 ± 0.048	2	0.004 ± 0.011
Zn	0.017 ± 0.055	1	0.026 ± 0.011
Y	−0.004 ± 0.085	5	−0.002 ± 0.031
Zr	−0.012 ± 0.064	1	0.000 ± 0.011
Ba	0.003 ± 0.062	3	−0.008 ± 0.067

Table 6.5: Abundances obtained for α Centauri A from Meléndez et al. (2009, [96], M09). The last column gives the average of the M09 and our MIKE and HARPS results.

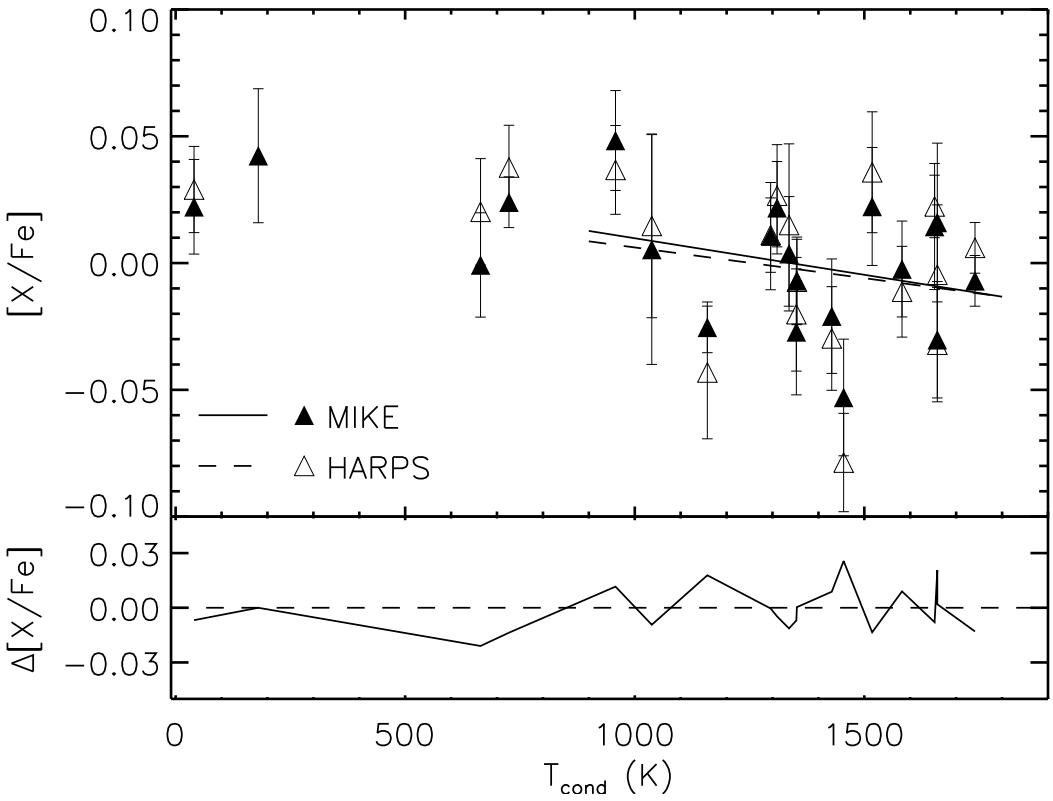

Figure 6-2: Photospheric elemental abundance versus respective condensation temperature for the MIKE and HARPS spectra of α Centauri A.

6.2 The condensation temperature trends

Figure 6-2 shows the elemental abundance [X/Fe] versus the corresponding condensation temperature as in Table 1.2. Element over iron ratio is used to compensate for the slightly different metallicities obtained for the two datasets. Nevertheless, some elements, such as Zinc (T_{cond} of 726 K), are extremely sensitive to changes in fundamental stellar parameters, which can lead to relatively large deviations for those elements, even though the measured equivalent widths are almost identical (see Table A.4). The solid and dashed lines are linear fits to the refractory abundances ($T_{cond} > 900$ K).

Despite the fact that the abundances for the individual elements do not always agree perfectly, the gradients of the refractory elements are identical within the errors: $g_{\mathrm{MIKE}} = (-2.9 \pm 2.8) \cdot 10^{-5}\mathrm{dex/K}^{-1}$, $g_{\mathrm{HARPS}} = (-2.4 \pm 3.6) \cdot 10^{-5}\mathrm{dex/K}^{-1}$. The lower panel in the Figure shows the difference between the results gained from the MIKE and from the HARPS data for each element.

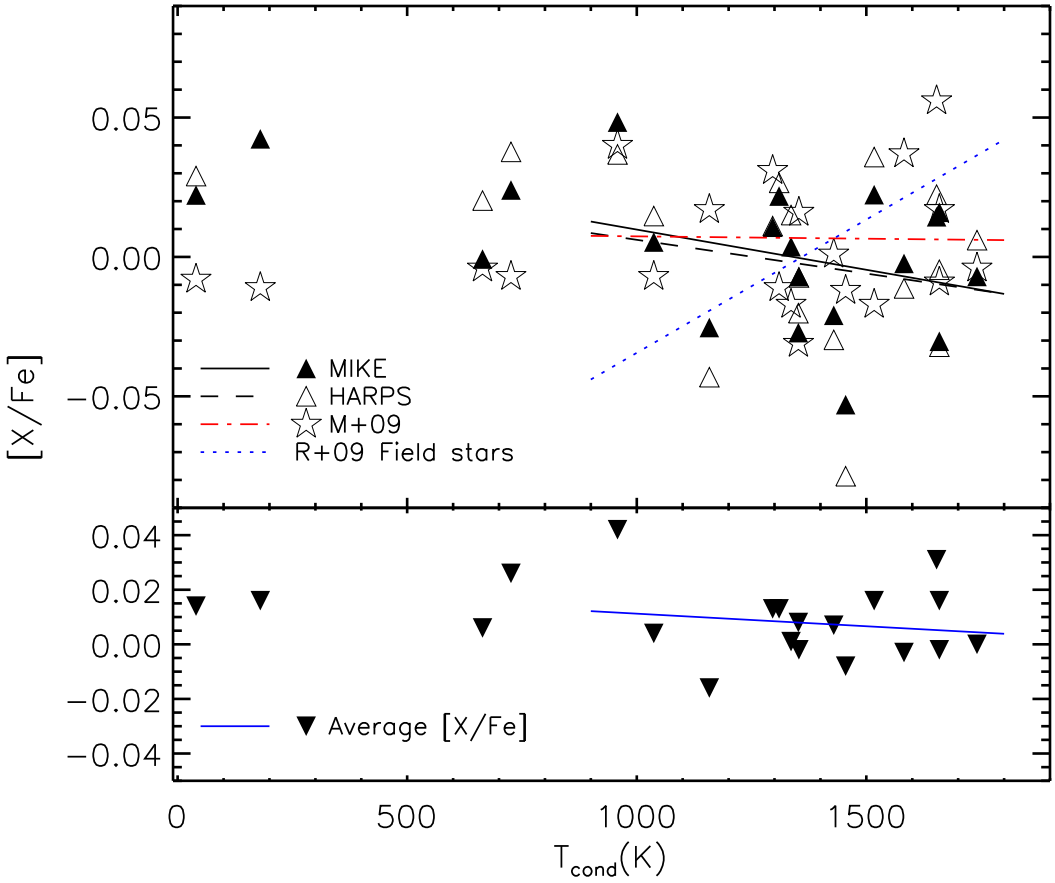

Figure 6-3: Photospheric elemental abundance versus respective condensation temperature for the MIKE and HARPS spectra as in Figure 6-2. Overplotted in star-shaped symbols are the results from Meléndez et al. (2009, [96]), as well as the refractory gradient for the comparison sample in Ramírez et al. (2009, [131]).

Figure 6-3 shows the MIKE and HARPS results, but also the results presented in Meléndez et al. (2009, M+09, [96]). They report a refractory slope of $-1.7 \cdot$

10^{-6}dex/K^{-1}. Also plotted (dotted blue line) is the average slope for the 22 solar twins analyzed by Ramírez et al. (2009, R+09, [131]), that they determine to be $(1.0 \pm 0.3) \cdot 10^{-4}$dex/K^{-1}.

6.3 Discussion

It is obvious, that α Centauri A shows a chemical composition very similar to the solar one. For most elements, the deviation from the solar value is comparable to the uncertainty of the value itself. The trend in the refractory regime is even weakly negative compared to the Sun, although it may be argued that the high sodium value at 958 K has a great contribution to the slope. However, the sodium values of all three samples agree almost perfectly, so we have a good reason to believe the abundance really is that high.

This weakly negative slope means that α Centauri A is even more depleted in high condensation temperature elements than the Sun compared to the average solar analog. According to the results by [96, 131], and following publications, this trend is a strong indicator towards the presence of one or more terrestrial planets. From the negative trend in refractories relative to solar, we can even conclude that the mass bound in rocky planets around α Centauri A is at least a high as in the solar system.

	T_{eff}(K)	log g	[Fe/H]
α Centauri A	5824 ± 26	4.307 ± 0.005	0.24 ± 0.03
α Centauri B	5316 ± 28	4.538 ± 0.008	0.25 ± 0.04

Table 6.6: Fundamental parameters for α Centauri A and α Centauri B, from Porto de Mello (2008, [124]).

Only recently, an Earth-sized planet has been detected around α Centauri B ([46]). This planet, however, appears to be far from habitable, given its rotational period of 3 Earth days and its semi major axis of 0.04 astronomical units. Even if the host star was cool enough to allow for life-supporting temperatures (i.e. temperatures that make liquid water possible, which is not the case given an effective temperature of α Centauri B of around 5300 K), the proximity to the host would lead to extreme influences from stellar activity or tidal locking (i.e., the same side of the planet faces the host star all the time). However, this finding proves that it is possible to find Earth-sized planets around solar-type stars, even though close-in planets are easier to detect than ones on an Earth-like orbit due to their gravitational influence on the host star.

Element	α Centauri A	α Centauri B
Na	0.14 ± 0.00	0.25 ± 0.00
Mg	0.00 ± 0.00	0.04 ± 0.00
Si	0.00 ± 0.06	0.00 ± 0.05
Ca	0.03 ± 0.03	0.09 ± 0.08
Sc	0.00 ± 0.02	0.01 ± 0.07
Ti	−0.01 ± 0.04	0.19 ± 0.14
V	0.02 ± 0.05	0.21 ± 0.09
Cr	0.00 ± 0.06	0.06 ± 0.09
Mn	0.07 ± 0.01	0.19 ± 0.06
Co	0.00 ± 0.06	0.06 ± 0.07
Ni	0.10 ± 0.07	0.11 ± 0.05
Cu	0.10 ± 0.05	0.10 ± 0.00
Y	−0.09 ± 0.05	−0.09 ± 0.08
Ba	−0.13 ± 0.05	−0.16 ± 0.08

Table 6.7: Abundances for α Centauri A and α Centauri B, from Porto de Mello et al. (2008, [124]).

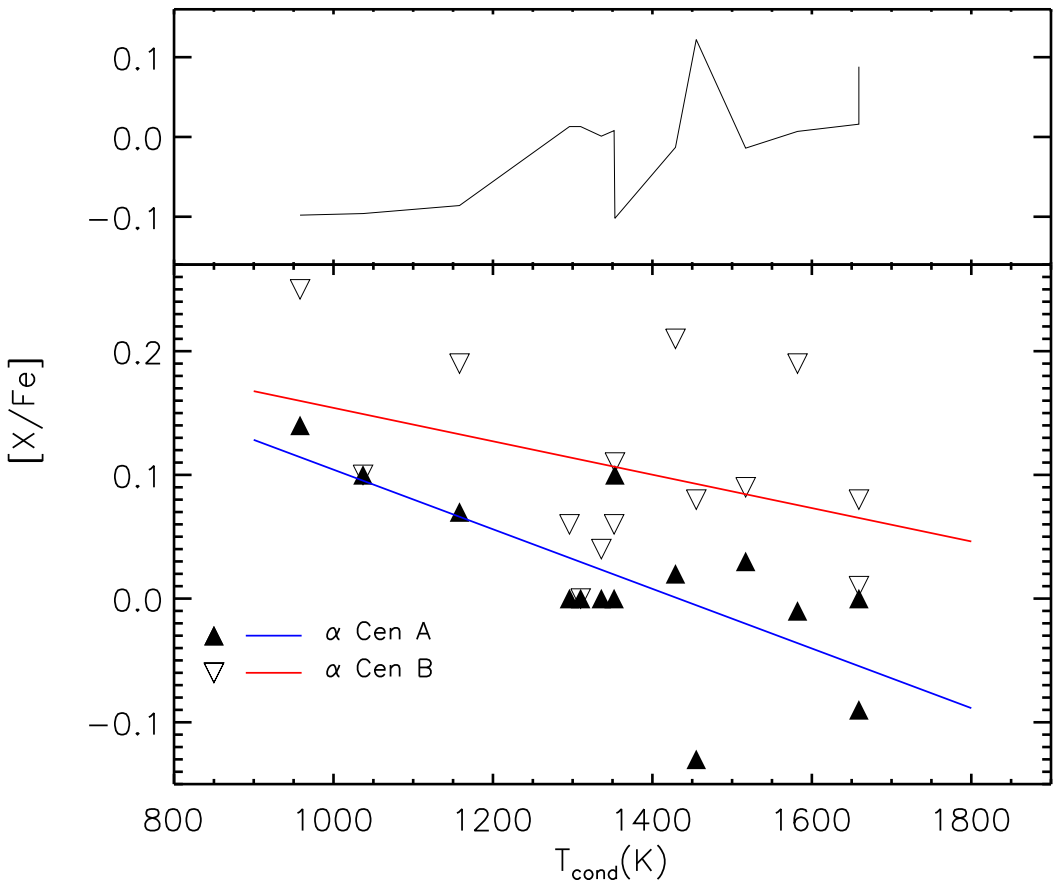

Figure 6-4: Photospheric elemental abundance versus respective condensation temperature for α Centauri A and α Centauri B as published in [124]. The upper panel shows the difference between their α Centauri A results and our average results as presented in Table 6.5.

In Table 6.7, we present the results of a comparison study by Porto de Mello et al, 2008 ([124], PdM08). They conducted an extensive analysis of the α Centauri binary system, including abundances for 14 elements in both stars. The elements covered in their work all lie in the refractory regime and don not agree too well with our results, but the intrinsic accuracy of the analysis should be very good. The methods used in their work are very similar to the ones used by us, including the addition of temperatures from Hα line fitting. Their fundamental parameters agree

well with ours (see Table 6.6).

Figure 6-4 shows our average results as presented in Table 6.5 minus the PdM08 ones in the first panel. The bottom panel shows the PdM08 α Centauri A and α Centauri B abundances and respective linear fits. It is evident, that the trend for α Centauri B is less steep than the α Centauri A one, which indicates a higher mass of rocky material bound in planets around α Centauri A compared to α Centauri B. Note however, that both trends are by far steeper than our trends derived for α Centauri A. This should not effect the differential results for the PdM08 data.

This trend agrees very well with the newly detected close-in Earth-sized planet around α Centauri B and again suggests terrestrial planets around α Centauri A.

Chapter 7

Summary and conclusions

In the present work, we examined the fundamental parameters and abundances in solar-type main sequence and subgiant stars. The fundamental questions leading to this analysis was the possible connection between abundance ratios in stellar photospheres and the presence of planets.

The work is divided into 3 main subjects: lithium abundances in solar-type stars, lithium abundances in subgiant stars, and the abundance pattern of α Centauri A.

Because elemental abundances are extremely sensitive to the fundamental stellar parameters, we had to restrict our analysis to solar-type stars in order to achieve the highest possible accuracy.

In a first step, we analyzed a set of 117 solar twin stars concerning their basic parameters, masses, ages, and surface lithium abundances. In a very careful, fully differential analysis, we achieved a substantially high precision in all parameters. Using those results, we were able to show that the lithium depletion that takes place in main sequence stars follows the trends predicted by theoretical models very nicely. We were also able to demonstrate, that solar-type planet host stars do not show a different behavior concerning lithium depletion that comparison field stars.

We used the sample presented in Israelian et al. (2009, [76]) to expose the selection biases that lead earlier publications to the wrong assumption that planet host stars with parameters similar to the Sun's are in average more depleted in lithium than comparison stars with a similar age. Those claims were mostly based on the fact that we find more planet hosts in slightly more metal-enhanced stars than in stars with solar metallicity, and simultaneously lithium seems to be more depleted in metal-rich stars.

We also found a number of high-lithium stars in the sample used by Israelian et al. that showed a clearly sub-solar surface gravity and therefore had biased the original sample. Using a sub-sample including only stars with fundamental parameters in a 2-σ-environment around the planet host stars, we were able to demonstrate that stars with and without detected planets do not show a different behavior concerning surface lithium abundances.

Using our data, we were also able to conclude that the Sun is not peculiar regarding its surface lithium abundance and age and the large difference in lithium abundances found in meteorites and in photospheric analyses can be explained purely by the normal lithium depletion depending on the age of a star.

The low-gravity objects mentioned above were the inception of a side project aiming for lithium abundances in solar-type subgiants. In the lithium versus age plane, those 10 stars found in the Israelian et al. sample suggested a sudden increase in surface lithium in solar-type stars at the end of the main sequence. This increase appeared to be as large as 2.5 dex for some stars, with a distinct gap between the main locus and the outliers, while cuts in mass lead to the conclusion, that the surface lithium abundance really is increasing abruptly when a star is leaving the the main sequence.

We gathered high resolution spectra for 76 subgiants from 2 different observing

runs to investigate the matter. Physical parameters were determined in the same fashion as for the solar analogs in the first study. Using theoretical isochrones, we were able to show that those low-gravity objects really are evolved stars at the end of the main sequence or beyond. The lithium abundances we deducted for those stars are higher than that of the solar analogs by 0.86 dex in average. At the same time, the evolved stars are in average 1.17 gigayears older. The large gap between the two groups on the other hand vanishes when we add the new objects to the original sample.

We concluded, that for solar-type stars, an increase in surface lithium abundance at the end of the main sequence appears very likely, and a dredge-up of lithium from the bottom of the convection zone seems to be the most acceptable scenario for this surprising activity.

The last section of this work deals with the condensation temperature trends in planet hosts. The original idea was to examine a large sample of solar-type stars regarding 20 different elements. After having reduced the spectra, we decided to start off with a test case to verify the quality of our process of analysis and chose α Centauri A to be the test object. Because of difficulties in the reduction process for the different datasets we gathers for α Centauri A, this test object remains the only one treated in this work regarding condensation temperature trends.

We obtained very high quality spectra for α Centauri A from 2 different sources (together with the necessary reference spectra). For a completely independent analysis, we analyzed both datasets separately and examined the object's fundamental parameters and surface abundances for 20 elements. When we plot those abundances (relative to the solar values) versus each element's condensation temperatures, it becomes obvious that α Centauri A is underabundant in refractory elements relative to the volatile ones and relative to the Sun.

In the Sun, an existing underabundance in refractory elements compared to the average of a sample of field stars has been suggested to be a trace of terrestrial planet formation. Seeing α Centauri A being even more depleted in those elements could be a strong indicator for one or more rocky planets around the solar-type star closest to us. The recent detection of a terrestrial planet around α Centauri B strengthens this claim, since α Centauri B shows a similar, but not as strong, condensation temperature trend as α Centauri A.

Appendix A

Tables

A.1 Solar Twins

HIP	HD	T_{eff}	$\log g$	[Fe/H]	$\log \epsilon_{Li}$ (LTE)	$\log \epsilon_{Li}$ (NLTE)	$\sigma(\log \epsilon_{Li})$	Mass	σ(m)	Age	$\sigma(\tau)$	Source(τ)	Parameters	Planets
Sun	Sun	5777 ± 0	4.44 ± 0	0.000 ± 0	1.03	1.07	0.04	1.00	0.01	4.5	0.5	iso	-	yes
348	225194	5777 ± 40	4.41 ± 0.07	−0.130 ± 0.024	1.08	1.11	0.05	0.97	0.01	6.2	1.5	iso	[131]	no
996	804	5860 ± 41	4.38 ± 0.07	0.000 ± 0.022	1.56	1.59	0.05	1.03	0.01	5.1	1.1	iso	[131]	no
1499	1461	5756 ± 44	4.37 ± 0.05	0.189 ± 0.015	0.89	0.95	-1.00	1.06	0.01	4.8	0.6	iso	[131]+[184]+[90]+[175]+[165]	yes
2131	236416	5720 ± 41	4.38 ± 0.07	−0.210 ± 0.026	0.10	0.13	-1.00	0.92	0.01	8.9	1.3	iso	[131]	no
2894	-	5820 ± 44	4.54 ± 0.07	−0.030 ± 0.025	1.81	1.84	0.05	1.02	0.01	1.6	0.8	iso	[131]	no
4909	6204	5836 ± 54	4.44 ± 0.07	0.020 ± 0.024	2.42	2.43	0.06	1.03	0.01	0.7	0.2	x-ray	[131]+[71]	no
5134	6470	5779 ± 38	4.49 ± 0.07	−0.190 ± 0.023	1.81	1.84	0.05	0.97	0.01	4.1	1.9	iso	[131]	no
6407	8291	5787 ± 25	4.47 ± 0.03	−0.090 ± 0.011	1.74	1.77	0.03	0.99	0.01	3.8	0.8	iso	[131]	no
7245	9446	5843 ± 47	4.53 ± 0.07	0.100 ± 0.023	1.87	1.91	0.06	1.07	0.01	1.3	0.7	iso	[131]	yes
8507	11195	5720 ± 55	4.44 ± 0.08	−0.080 ± 0.026	1.58	1.62	0.07	0.96	0.01	5.6	2.0	iso	[131]	no
8841	-	5676 ± 45	4.50 ± 0.06	−0.120 ± 0.021	0.19	0.23	-1.00	0.95	0.01	4.3	1.8	iso	[131]	no
9349	12264	5825 ± 28	4.49 ± 0.06	0.010 ± 0.017	2.03	2.06	0.04	1.03	0.01	2.5	1.2	iso	[131]+[175]	no
10710	-	5817 ± 43	4.39 ± 0.06	−0.130 ± 0.022	1.90	1.92	0.05	0.98	0.01	6.5	1.1	iso	[131]	no
11072	14802	5897 ± 84	4.01 ± 0.05	−0.037 ± 0.057	2.42	2.42	0.02	1.15	0.02	0.7	0.1	rot	TW+[12]	no
11728	15632	5738 ± 30	4.37 ± 0.05	0.045 ± 0.019	1.29	1.34	0.04	0.99	0.01	6.9	0.8	iso	[131]+[175]	no
11915	16008	5793 ± 43	4.45 ± 0.06	−0.050 ± 0.021	1.69	1.72	0.05	1.00	0.01	4.3	1.6	iso	[131]	no
12186	16417	5812 ± 34	4.09 ± 0.05	0.094 ± 0.04	1.70	1.74	0.07	1.11	0.01	7.0	0.4	iso	TW+[184]+[165]	yes
14614	19518	5803 ± 28	4.47 ± 0.03	−0.104 ± 0.016	1.59	1.62	0.03	0.99	0.01	3.6	0.9	iso	[131]+[175]+TW	no
14632	19373	6026 ± 42	4.28 ± 0.05	0.136 ± 0.019	2.46	2.47	0.07	1.17	0.01	3.7	0.3	iso	[131]+[184]	unknown
15457	20630	5771 ± 65	4.56 ± 0.01	0.078 ± 0.041	2.18	2.22	0.03	1.02	0.01	0.5	0.0	rot	TW+[184]	unknown
18261	24552	5891 ± 34	4.44 ± 0.05	0.002 ± 0.016	2.27	2.28	0.04	1.05	0.01	3.1	1.1	iso	[131]+[175]	no
22263	30495	5826 ± 48	4.54 ± 0.01	0.005 ± 0.029	2.45	2.46	0.02	1.02	0.01	0.5	0.1	rot	TW+[184]	unknown
22528	-	5683 ± 52	4.33 ± 0.10	−0.350 ± 0.035	0.46	0.49	-1.00	0.87	0.01	12.2	1.5	iso	[131]	no
23835	32923	5723 ± 33	4.16 ± 0.05	−0.184 ± 0.017	1.66	1.69	0.05	0.96	0.01	10.7	0.4	iso	[131]+[184]	unknown
25670	36152	5755 ± 37	4.38 ± 0.05	0.071 ± 0.017	1.24	1.29	0.05	1.01	0.01	6.0	0.9	iso	[131]+[175]	unknown
28336	40620	5713 ± 61	4.53 ± 0.08	−0.170 ± 0.027	1.19	1.23	0.07	0.95	0.01	4.0	1.8	iso	[131]	no
29525	42807	5715 ± 61	4.41 ± 0.03	−0.005 ± 0.036	1.99	2.03	0.02	0.97	0.01	0.4	0.0	rot	TW+[12]	no
30037	45021	5690 ± 30	4.42 ± 0.06	0.05 ± 0.03	0.66	0.71	-1.00	0.98	0.01	5.9	1.4	iso	[96]	no
30502	45346	5745 ± 25	4.47 ± 0.05	−0.01 ± 0.02	0.95	0.99	-1.00	1.00	0.01	3.8	1.4	iso	[96]	no
36512	59711	5740 ± 15	4.50 ± 0.03	−0.092 ± 0.02	1.27	1.31	0.04	0.99	0.01	2.7	1.0	iso	[96]+[175]+[165]	unknown
38072	63487	5839 ± 68	4.53 ± 0.11	0.060 ± 0.037	1.67	1.71	0.08	1.05	0.01	2.4	1.2	iso	[131]	no
38228	63433	5693 ± 58	4.52 ± 0.07	0.007 ± 0.025	2.51	2.53	0.07	0.99	0.01	0.3	0.0	rot	[131]+[184], τ from [60]	unknown
39748	67578	5835 ± 30	4.48 ± 0.06	−0.20 ± 0.03	2.16	2.17	0.03	0.98	0.01	3.8	1.6	iso	[96]	no
41317	71334	5724 ± 15	4.46 ± 0.03	−0.044 ± 0.02	0.92	0.96	-1.00	0.98	0.01	4.7	0.8	iso	[96]+[184]+[165]	unknown
42438	72905	5864 ± 47	4.46 ± 0.09	−0.052 ± 0.026	2.89	2.85	0.07	1.02	0.01	0.2	0.0	rot	[131]+TW	no
43190	75288	5775 ± 30	4.37 ± 0.06	0.12 ± 0.03	0.65	0.70	-1.00	1.04	0.01	5.3	0.9	iso	[96]	no
44324	77006	5934 ± 49	4.51 ± 0.06	−0.020 ± 0.019	2.41	2.41	0.06	1.07	0.01	1.5	0.6	iso	[131]+[175]	no
44713	78429	5784 ± 35	4.36 ± 0.02	0.096 ± 0.024	0.91	0.96	0.10	1.03	0.01	5.8	0.6	iso	TW + [184] + [165]	unknown
44935	78534	5800 ± 25	4.41 ± 0.05	0.07 ± 0.02	0.95	0.99	-1.00	1.03	0.01	4.6	1.0	iso	[96]	no
44997	78660	5782 ± 29	4.52 ± 0.04	0.033 ± 0.02	0.99	1.03	0.06	1.03	0.01	1.5	0.5	iso	[96] + [175]	no
46066	80533	5709 ± 65	4.49 ± 0.12	−0.070 ± 0.039	1.37	1.41	0.08	0.96	0.01	5.2	2.3	iso	[131]	no
46126	81700	5890 ± 30	4.48 ± 0.06	0.14 ± 0.03	2.17	2.20	0.03	1.09	0.01	1.7	0.8	iso	[96]	no
47990	84705	5910 ± 40	4.53 ± 0.08	0.12 ± 0.03	2.24	2.27	0.02	1.10	0.01	0.8	0.4	iso	[96]	no
49572	-	5831 ± 52	4.33 ± 0.06	0.010 ± 0.021	1.32	1.35	0.06	1.02	0.01	6.6	0.8	iso	[131]	no
49756	88072	5804 ± 52	4.45 ± 0.07	0.041 ± 0.023	1.61	1.65	0.07	1.03	0.01	3.6	1.6	iso	[131]+[184]+[175]	unknown
50826	-	5725 ± 30	4.47 ± 0.06	−0.28 ± 0.03	0.95	0.98	0.08	0.92	0.01	6.1	1.8	iso	[96]	no
51258	90722	5720 ± 25	4.23 ± 0.05	0.360 ± 0.03	0.72	0.80	-1.00	1.17	0.02	5.1	0.2	iso	[96]+[184]	unknown
52040	91909	5785 ± 44	4.51 ± 0.06	−0.090 ± 0.021	1.69	1.72	0.05	0.99	0.01	3.0	1.2	iso	[131]	no
52137	92074	5842 ± 69	4.56 ± 0.08	0.070 ± 0.026	2.25	2.28	0.08	1.06	0.01	0.9	0.5	iso	[131]	no
53721	95128	5916 ± 53	4.48 ± 0.01	0.027 ± 0.038	1.79	1.81	0.02	1.07	0.01	1.0	0.5	iso + rot	TW+[184]+[144]+[93]	yes
54102	96116	5870 ± 30	4.51 ± 0.06	0.04 ± 0.03	2.20	2.22	0.03	1.06	0.01	1.6	0.7	iso	[96]	no
55409	98649	5760 ± 25	4.52 ± 0.05	−0.01 ± 0.02	0.84	0.88	0.07	1.01	0.01	2.1	0.8	iso	[96]	no
55459	98618	5838 ± 21	4.42 ± 0.03	0.038 ± 0.012	1.53	1.56	0.04	1.03	0.01	4.1	0.7	iso	[131]+[184]+[100]+[175]	unknown
56948	101364	5795 ± 23	4.43 ± 0.03	0.023 ± 0.014	1.30	1.34	0.04	1.01	0.01	4.4	0.7	iso	[131]+[101]+[176]	unknown
56997	101501	5559 ± 65	4.53 ± 0.08	−0.030 ± 0.027	1.08	1.14	0.08	0.94	0.01	4.6	2.1	iso	[131]+[184]	unknown
57291	102117	5690 ± 22	4.30 ± 0.04	0.304 ± 0.03	0.73	0.81	-1.00	1.11	0.01	5.6	0.2	iso	[96]+[184]+[165]	yes
59357	105779	5810 ± 30	4.45 ± 0.06	−0.24 ± 0.03	1.70	1.72	0.04	0.95	0.01	5.5	1.5	iso	[96]	no
59610	106252	5899 ± 62	4.34 ± 0.04	−0.034 ± 0.041	1.71	1.73	0.04	1.04	0.01	5.7	0.7	iso	TW+[184]	yes
60081	107148	5811 ± 21	4.38 ± 0.04	0.315 ± 0.03	1.33	1.40	0.06	1.12	0.01	3.4	0.5	iso	[96]+[184]+[165]	yes
60314	107633	5874 ± 72	4.52 ± 0.10	0.110 ± 0.033	1.85	1.89	0.09	1.07	0.01	1.9	0.9	iso	[131]	no

Table A.1: Specifications for the different samples

HIP	HD	T_{eff}	log g	[Fe/H]	log ϵ_{Li} (LTE)	log ϵ_{Li} (NLTE)	σ(log ϵ_{Li})	Mass	σ(m)	Age	$\sigma(\tau)$	Source(τ)	Parameters	Planets
60370	107692	5897 ± 25	4.46 ± 0.05	0.171 ± 0.03	2.31	2.34	0.02	1.11	0.01	1.6	0.8	iso	[96]+[184]	unknown
60653	108204	5725 ± 30	4.38 ± 0.06	−0.29 ± 0.03	0.92	0.95	-1.00	0.90	0.01	9.6	1.2	iso	[96]	no
62175	110869	5849 ± 51	4.43 ± 0.06	0.140 ± 0.021	1.91	1.95	0.06	1.08	0.01	2.9	1.2	iso	[131]+[175]	no
64150	114174	5755 ± 41	4.39 ± 0.05	0.056 ± 0.016	0.76	0.81	-1.00	1.00	0.01	5.9	1.0	iso	[131]+[184]+[175]	unknown
64497	114826	5860 ± 110	4.56 ± 0.11	0.120 ± 0.037	2.60	2.61	0.13	1.07	0.02	1.3	0.8	iso	[131]	no
64713	115169	5815 ± 25	4.52 ± 0.05	−0.01 ± 0.02	1.43	1.46	0.04	1.03	0.01	1.7	0.8	iso	[96]	no
64794	115382	5743 ± 61	4.33 ± 0.08	−0.100 ± 0.027	0.61	0.65	-1.00	0.96	0.01	8.8	1.0	iso	[131]	no
64993	115739	5875 ± 30	4.56 ± 0.06	0.09 ± 0.03	2.30	2.32	0.03	1.08	0.01	0.9	0.5	iso	[96]	no
66618	118475	5951 ± 25	4.35 ± 0.05	0.135 ± 0.03	0.96	0.99	-1.00	1.12	0.01	3.6	0.5	iso	[96]+[184]	unknown
66885	119205	5685 ± 30	4.48 ± 0.06	−0.38 ± 0.03	0.77	0.80	-1.00	0.88	0.01	7.4	1.9	iso	[96]	no
69063	123152	5670 ± 30	4.31 ± 0.06	−0.45 ± 0.03	0.74	0.76	-1.00	0.83	0.01	14.1	0.7	iso	[96]	no
71683	128620	5840 ± 22	4.33 ± 0.04	0.228 ± 0.03	1.52	1.57	0.03	1.11	0.01	4.3	0.3	iso	[96]+[184]+[124]	unknown
72659	131156	5517 ± 67	4.56 ± 0.09	−0.117 ± 0.033	2.44	2.47	0.10	0.91	0.01	0.2	0.0	rot	[131]+[184]	unknown
73815	133600	5803 ± 33	4.34 ± 0.05	0.020 ± 0.016	0.98	1.02	-1.00	1.01	0.01	6.8	0.6	iso	[131]+[101]	no
74341	134902	5853 ± 57	4.51 ± 0.08	0.090 ± 0.026	1.44	1.48	0.07	1.07	0.01	1.9	0.9	iso	[131]	no
74389	134664	5859 ± 24	4.48 ± 0.04	0.105 ± 0.03	2.08	2.12	0.03	1.07	0.01	1.6	0.7	iso	[96]+[165]	unknown
75923	138159	5775 ± 25	4.56 ± 0.05	−0.02 ± 0.02	2.21	2.24	0.04	1.02	0.01	0.9	0.2	iso	[96]	no
77052	140538	5697 ± 33	4.54 ± 0.02	0.035 ± 0.023	1.49	1.54	0.01	1.01	0.01	0.6	0.4	iso	TW+[184]	unknown
77466	-	5700 ± 56	4.40 ± 0.09	−0.280 ± 0.028	0.43	0.46	-1.00	0.90	0.01	9.3	1.9	iso	[131]	no
77740	141937	5900 ± 19	4.45 ± 0.04	0.125 ± 0.03	2.38	2.40	0.02	1.09	0.01	1.3	0.9	iso + rot	[96]+[144]+[184]+[90]+[165]	yes
77883	142331	5695 ± 25	4.39 ± 0.05	0.04 ± 0.02	0.75	0.80	-1.00	0.98	0.01	7.0	0.9	iso	[96]	no
78028	-	5879 ± 98	4.57 ± 0.12	−0.030 ± 0.041	1.79	1.81	0.11	1.04	0.02	1.8	1.0	iso	[131]	no
78680	144270	5923 ± 67	4.57 ± 0.08	−0.000 ± 0.027	2.61	2.61	0.08	1.06	0.01	0.6	0.4	iso	[131]	no
79186	145514	5709 ± 48	4.27 ± 0.08	−0.120 ± 0.024	0.29	0.33	-1.00	0.95	0.01	10.3	0.7	iso	[131]	no
79304	145478	5945 ± 30	4.53 ± 0.06	0.11 ± 0.03	2.09	2.12	0.03	1.11	0.01	0.4	0.2	iso	[96]	no
79578	145825	5860 ± 33	4.53 ± 0.07	0.072 ± 0.03	2.05	2.08	0.03	1.07	0.01	1.3	0.6	iso	[96]+[184]	unknown
79672	146233	5822 ± 9	4.45 ± 0.02	0.051 ± 0.02	1.55	1.59	0.04	1.04	0.01	3.1	0.5	iso	[96]+TW+[165]	unknown
80337	147513	5881 ± 33	4.53 ± 0.02	0.033 ± 0.022	2.01	2.04	0.02	1.06	0.03	0.6	0.1	rot	TW (S^4N+HARPS)+[184]+[165]+[12]	yes
81512	-	5790 ± 58	4.46 ± 0.07	−0.020 ± 0.025	0.89	0.92	-1.00	1.01	0.01	4.0	1.7	iso	[131]	no
82853	150027	5640 ± 30	4.21 ± 0.06	−0.18 ± 0.03	0.60	0.64	-1.00	0.92	0.01	12.5	0.5	iso	[96]	no
83601	154417	6071 ± 43	4.38 ± 0.08	0.048 ± 0.028	2.82	2.79	0.06	1.13	0.01	2.4	1.1	iso	[131]+[184]	unknown
83707	152441	5880 ± 30	4.45 ± 0.06	0.15 ± 0.03	1.83	1.87	0.03	1.10	0.01	2.3	1.0	iso	[96]	no
85042	157347	5692 ± 37	4.39 ± 0.02	0.037 ± 0.026	0.56	0.61	-1.00	0.98	0.01	7.2	0.5	iso	TW+[184]+[165]	unknown
85272	156922	5700 ± 30	4.42 ± 0.06	−0.34 ± 0.03	0.58	0.61	-1.00	0.88	0.01	9.4	1.4	iso	[96]	no
85285	157691	5730 ± 30	4.43 ± 0.06	−0.39 ± 0.03	0.71	0.73	-1.00	0.88	0.01	8.8	1.5	iso	[96]	no
86796	160691	5809 ± 22	4.28 ± 0.04	0.298 ± 0.03	1.06	1.13	0.07	1.15	0.01	4.6	0.2	iso	[96]+[184]+[165]	yes
88194	164595	5735 ± 21	4.40 ± 0.03	−0.071 ± 0.010	0.98	1.02	0.04	0.96	0.01	7.3	0.6	iso	[131]+[184]+[175]	unknown
88427	-	5810 ± 57	4.42 ± 0.07	−0.160 ± 0.025	0.85	0.87	-1.00	0.97	0.01	5.7	1.5	iso	[131]	no
89162	165357	5835 ± 30	4.32 ± 0.06	0.07 ± 0.03	1.35	1.39	0.09	1.05	0.01	6.0	0.6	iso	[96]	no
89443	238838	5796 ± 73	4.48 ± 0.12	−0.020 ± 0.038	1.06	1.09	-1.00	1.01	0.01	4.4	1.9	iso	[131]	no
89650	167060	5855 ± 25	4.48 ± 0.05	0.02 ± 0.02	1.03	1.06	0.07	1.05	0.01	2.2	1.0	iso	[96]	no
91332	171918	5775 ± 25	4.20 ± 0.05	0.206 ± 0.03	1.40	1.46	0.09	1.12	0.02	6.4	0.7	iso	[96]+[184]	unknown
96402	184768	5713 ± 49	4.33 ± 0.03	−0.029 ± 0.030	0.64	0.68	-1.00	0.97	0.01	8.7	0.7	iso	TW+[175]	no
96901	186427	5737 ± 28	4.34 ± 0.04	0.055 ± 0.016	1.38	1.42	-1.00	1.00	0.01	7.5	0.5	iso	[131]+[184]+[90]+[175]	yes
96895	186408	5808 ± 39	4.33 ± 0.05	0.097 ± 0.020	0.81	0.86	0.06	1.05	0.01	6.0	0.6	iso	[131]+[184]+[90]	unknown
100963	195034	5802 ± 17	4.45 ± 0.03	0.008 ± 0.013	1.72	1.75	0.05	1.02	0.01	3.6	0.8	iso	[131]+[175]+[176]	no
100970	195019	5823 ± 40	4.23 ± 0.02	0.083 ± 0.025	1.39	1.43	0.10	1.06	0.01	7.2	0.4	iso	TW+[184]	yes
102152	197027	5737 ± 47	4.35 ± 0.06	−0.010 ± 0.022	0.65	0.69	-1.00	0.98	0.01	7.7	0.9	iso	[131]+[96]	no
104504	201422	5836 ± 48	4.50 ± 0.06	−0.160 ± 0.022	2.42	2.42	0.06	1.00	0.02	3.0	1.4	iso	[131]	no
107350	206860	6015 ± 50	4.48 ± 0.07	−0.020 ± 0.019	2.91	2.87	0.07	1.09	0.01	0.2	0.0	rot	[131]+[184]	unknown
108708	209096	5875 ± 51	4.51 ± 0.07	0.150 ± 0.024	2.42	2.44	0.06	1.10	0.01	1.3	0.6	iso	[131]	no
108996	209562	5838 ± 56	4.50 ± 0.08	0.060 ± 0.027	2.40	2.42	0.07	1.05	0.01	2.3	1.1	iso	[131]	no
109110	209779	5817 ± 60	4.46 ± 0.03	0.062 ± 0.030	2.51	2.52	0.01	1.04	0.01	0.7	0.1	rot	TW+[184]+[175]+[12]	unknown
109931	-	5739 ± 74	4.29 ± 0.08	0.040 ± 0.026	0.95	1.00	-1.00	1.00	0.01	8.2	0.9	iso	[131]	no
113357	217014	5803 ± 47	4.38 ± 0.05	0.221 ± 0.017	1.36	1.42	0.07	1.09	0.01	3.9	0.7	iso	[131]+[184]+[90]	yes
115604	-	5821 ± 51	4.43 ± 0.06	0.140 ± 0.019	0.85	0.90	-1.00	1.07	0.01	3.1	1.2	iso	[131]	no
118159	224448	5905 ± 44	4.55 ± 0.07	−0.010 ± 0.022	2.69	2.68	0.05	1.06	0.01	0.8	0.4	iso	[131]	no

Name / HIP	HD	Mass	σ(m)	Age	$\sigma(\tau)$	Name / HIP	HD	Mass	σ(m)	Age	$\sigma(\tau)$
WASP 5	-	0.99	0.06	7.9	3.3	52409	92788	1.08	0.01	3.8	1.0
XO-1	-	1.01	0.01	2.3	1.2	53837	95521	0.98	0.01	3.4	1.1
1499	1461	1.07	0.01	4.5	0.6	54287	96423	1.01	0.01	7.2	0.6
1954	2071	0.97	0.01	4.6	1.1	54400	96700	0.97	0.01	6.6	0.6
2021	2151	1.12	0.08	6.7	1.4	97998	97998	0.90	0.01	1.9	0.6
5339	4307	1.01	0.01	9.0	0.4	60081	107148	1.12	0.01	3.0	0.6
6455	8406	0.98	0.01	3.0	0.6	60729	108309	1.05	0.01	7.5	0.3
8798	11505	0.93	0.01	8.6	0.6	62345	111031	1.10	0.01	3.4	0.8
9381	12387	0.91	0.01	9.1	1.7	64408	114613	1.20	0.02	5.9	0.3
9683	12661	1.10	0.03	4.5	1.3	64459	114729	0.97	0.01	9.7	0.2
12048	16141	1.09	0.01	6.9	0.3	64550	114853	0.92	0.01	7.4	0.9
12186	16417	1.12	0.01	6.7	0.2	65036	115585	1.13	0.03	5.3	0.5
14501	19467	0.94	0.01	10.0	0.3	71683	128620	1.17	0.07	4.1	1.5
15442	20619	0.94	0.01	3.9	1.2	74500	134987	1.10	0.02	5.4	0.5
15330	20766	0.94	0.02	3.4	1.7	78330	143114	0.88	0.01	9.9	0.8
15527	20782	0.98	0.01	7.3	0.3	78459	143761	0.98	0.02	6.1	2.6
16365	21938	0.86	0.01	10.8	0.7	79524	145809	0.96	0.01	10.3	0.3
19925	27063	1.01	0.01	4.2	1.2	79672	146233	1.03	0.01	3.3	0.8
20625	28471	0.97	0.01	7.7	0.3	83906	154962	1.22	0.03	4.7	0.8
20677	28701	0.89	0.01	9.5	0.5	160691	160691	1.14	0.02	4.8	0.3
23627	32724	0.97	0.01	9.2	0.3	95962	183658	1.01	0.01	5.3	0.7
22504	34449	1.02	0.01	1.5	0.8	96901	186427	1.02	0.02	5.0	1.9
25670	36152	1.05	0.01	2.6	0.9	97336	187123	1.07	0.01	3.5	1.5
26737	37962	0.94	0.01	5.2	1.8	97769	188015	1.10	0.02	1.8	0.9
27435	38858	0.95	0.01	3.3	0.7	98959	189567	0.92	0.01	8.4	0.4
30243	44420	1.11	0.01	3.5	0.6	98589	189625	1.09	0.01	2.5	1.0
30104	44594	1.08	0.00	4.1	0.5	102664	198075	0.99	0.01	2.3	1.0
30476	45289	0.97	0.00	8.8	0.3	104903	202206	1.09	0.01	1.4	0.6
34065	53705	0.97	0.01	6.8	2.3	106006	204313	1.06	0.01	4.6	0.5
36512	59711A	0.96	0.01	5.3	1.0	108468	208704	0.99	0.01	6.6	0.3
39417	66428	1.09	0.02	5.8	1.0	109821	210918	0.96	0.01	8.2	0.4
43726	76151	1.05	0.01	1.5	0.5	110109	211415	0.96	0.01	6.5	1.2
43686	76700	1.17	0.07	4.5	1.2	112414	215456	1.04	0.01	8.4	0.4
44713	78429	1.02	0.01	7.0	0.5	113357	217014	1.08	0.02	3.4	1.6
44890	78538	1.01	0.01	2.5	1.1	-	219542	1.04	0.02	4.6	1.5
44860	78558	0.85	0.01	12.5	0.7	115577	220507	0.98	0.01	9.3	0.5
44896	78612	0.96	0.01	9.4	0.3	116250	221420	1.29	0.06	4.7	0.7
46007	81110	1.11	0.01	0.4	0.1	116852	222480	1.15	0.03	5.6	0.8
49728	88084	0.97	0.01	6.2	0.8	116906	222582	0.99	0.01	6.7	0.8
50534	89454	1.03	0.01	3.0	1.1	117320	223171	1.09	0.01	6.7	0.3
52369	92719	1.01	0.01	1.6	0.9	118123	224393	0.92	0.01	3.6	1.0

Table A.2: Sample used in I09. Masses and ages are from this work.

A.2 Subgiants

Table A.3: Specifications for the subgiants

Object	Sample	T_{eff} (K)	log g	[Fe/H]	log ϵ_{Li} (LTE)	log ϵ_{Li} (NLTE)	σ(Li)	τ (Gyr)	τ_{min}	τ_{max}	M ($M_{\odot}$)	M_{min}	M_{max}	Planets
Sun	both	5778 ± 10	4.44 ± 0.05	0.000 ± 0.005	1.05	1.09	0.03	4.45	4.26	5.43	1.000	0.993	1.003	no
HD114424	MIKE	6073 ± 71	4.61 ± 0.12	0.166 ± 0.041	2.25	2.27	0.05	0.69	0.64	2.66	1.153	1.127	1.189	no
HIP106913	MIKE	5988 ± 81	4.50 ± 0.14	0.182 ± 0.049	2.15	2.18	0.03	1.62	1.15	3.90	1.131	1.097	1.175	no
HIP115286	MIKE	5843 ± 77	4.08 ± 0.15	−0.071 ± 0.053	2.05	2.07	0.05	7.37	5.47	8.72	1.044	0.999	1.158	no
HIP115697	MIKE	6063 ± 170	4.57 ± 0.26	0.131 ± 0.090	2.20	2.21	0.05	1.90	1.58	5.54	1.121	1.048	1.221	yes
HIP115951	MIKE	5938 ± 82	4.28 ± 0.23	0.098 ± 0.077	0.75	0.75	-1	4.42	2.96	6.24	1.111	1.052	1.209	no
HIP117066	MIKE	5983 ± 186	4.76 ± 0.28	−0.012 ± 0.095	2.00	2.01	0.03	0.51	1.87	7.03	1.044	0.975	1.127	no
HIP117320	MIKE	5793 ± 86	4.08 ± 0.16	0.068 ± 0.054	1.85	1.89	0.05	7.26	5.17	8.59	1.065	1.013	1.185	no
HIP15940	MIKE	5508 ± 58	4.03 ± 0.10	−0.521 ± 0.035	1.65	1.68	0.05	13.57	12.62	13.7	0.863	0.864	0.960	no
HIP17486	MIKE	6053 ± 88	4.22 ± 0.13	0.251 ± 0.046	2.30	2.32	0.03	3.13	2.03	3.96	1.191	1.168	1.323	no
HIP17960	MIKE	5923 ± 70	4.47 ± 0.13	0.258 ± 0.044	0.90	0.90	-1	1.79	1.14	3.85	1.126	1.107	1.174	no
HIP23286	MIKE	5763 ± 66	4.18 ± 0.13	0.091 ± 0.044	1.35	1.40	0.05	7.93	5.80	8.82	1.026	1.004	1.108	no
HIP23627	MIKE	5798 ± 79	4.06 ± 0.15	−0.243 ± 0.050	1.70	1.72	0.05	8.72	6.51	10.74	0.953	0.937	1.109	no
HIP24681	MIKE	5883 ± 93	4.18 ± 0.17	0.130 ± 0.056	1.61	1.56	0.07	5.64	3.92	6.92	1.090	1.055	1.213	yes
HIP25490	MIKE	5873 ± 99	3.89 ± 0.18	−0.132 ± 0.063	2.40	2.54	0.05	5.69	3.95	8.94	1.080	0.993	1.292	no
HIP26380	MIKE	6008 ± 151	4.33 ± 0.25	−0.244 ± 0.086	2.43	2.41	0.03	5.28	3.22	8.46	0.987	0.946	1.107	yes
HIP26534	MIKE	5918 ± 56	4.20 ± 0.11	−0.092 ± 0.038	2.15	2.16	0.05	7.03	5.42	7.68	1.036	1.016	1.096	no
HIP26729	MIKE	5908 ± 159	4.29 ± 0.27	0.032 ± 0.092	2.07	2.09	0.05	5.14	3.12	8.10	1.050	0.985	1.181	no
HIP27058	MIKE	5833 ± 76	4.17 ± 0.16	−0.109 ± 0.053	1.49	1.51	0.05	8.16	5.68	9.23	1.005	0.971	1.090	no
HIP28428	MIKE	5723 ± 68	3.86 ± 0.12	−0.355 ± 0.043	2.40	2.40	0.03	6.18	4.33	9.57	1.070	0.987	1.243	no
HIP30114	MIKE	5898 ± 94	4.54 ± 0.15	0.132 ± 0.052	1.04	1.08	0.07	1.86	1.45	5.35	1.081	1.039	1.124	yes
HIP30232	MIKE	5898 ± 80	4.55 ± 0.15	−0.142 ± 0.052	1.05	1.07	0.05	2.87	1.94	6.86	1.006	0.973	1.043	no
HIP3169	MIKE	6103 ± 100	3.98 ± 0.20	−0.073 ± 0.068	1.45	1.45	0.05	4.34	3.06	5.41	1.184	1.118	1.386	no
HIP33371	MIKE	5863 ± 78	4.03 ± 0.15	−0.199 ± 0.050	2.37	2.37	0.05	7.38	5.57	9.17	1.031	0.981	1.167	no
HIP35209	MIKE	5978 ± 133	4.49 ± 0.21	0.076 ± 0.074	2.33	2.34	0.03	2.84	1.90	6.17	1.081	1.026	1.162	no
HIP36481	MIKE	5748 ± 76	3.87 ± 0.18	−0.230 ± 0.061	2.15	2.17	0.03	6.06	4.07	10.03	1.032	0.978	1.292	no
HIP36809	MIKE	5823 ± 111	3.61 ± 0.26	−0.156 ± 0.086	2.09	2.11	0.05	2.90	1.95	7.21	1.109	1.086	1.710	no
HIP37032	MIKE	5663 ± 79	4.11 ± 0.14	−0.231 ± 0.051	2.12	2.14	0.05	11.42	8.32	13.02	0.917	0.890	1.036	no
HIP38120	MIKE	5673 ± 98	3.81 ± 0.19	−0.320 ± 0.065	2.28	2.29	0.05	5.93	3.73	10.89	1.025	0.953	1.309	no
HIP4093	MIKE	5788 ± 76	4.12 ± 0.13	0.015 ± 0.044	1.53	1.51	0.07	7.94	6.07	9.10	1.026	0.998	1.127	no
HIP42030	MIKE	5873 ± 93	4.14 ± 0.17	−0.075 ± 0.059	2.15	2.16	0.05	7.32	4.87	8.55	1.032	0.992	1.137	yes
HIP42123	MIKE	5803 ± 135	3.56 ± 0.21	−0.135 ± 0.073	1.15	1.19	0.05	2.34	1.66	5.53	1.411	1.187	1.800	no
HIP44696	MIKE	5848 ± 86	3.86 ± 0.15	0.014 ± 0.051	1.89	1.74	0.05	4.65	3.50	6.91	1.210	1.109	1.396	no
HIP44927	MIKE	5908 ± 109	3.85 ± 0.20	−0.280 ± 0.070	1.20	1.21	0.07	5.12	3.46	8.46	1.052	1.002	1.342	no
HIP46388	MIKE	6008 ± 61	4.38 ± 0.11	0.109 ± 0.037	2.09	2.11	0.05	2.56	1.59	4.36	1.121	1.093	1.162	no
HIP49024	MIKE	5933 ± 84	4.09 ± 0.16	−0.121 ± 0.055	2.09	2.10	0.05	6.67	4.77	7.79	1.052	1.015	1.174	no
HIP54582	MIKE	5808 ± 73	4.14 ± 0.13	−0.132 ± 0.044	1.65	1.58	0.05	8.63	6.74	9.86	0.986	0.964	1.083	no
HIP58331	MIKE	5893 ± 70	3.58 ± 0.12	−0.280 ± 0.039	0.95	0.97	-1	2.27	1.77	3.40	1.564	1.354	1.687	no
HIP66974	MIKE	5748 ± 83	3.89 ± 0.16	−0.084 ± 0.053	2.01	2.04	0.03	5.83	4.12	8.86	1.097	1.029	1.309	no

Object	Sample	$T_{\rm eff}$ (K)	log g	[Fe/H]	log ϵ_{Li} (LTE)	log ϵ_{Li} (NLTE)	σ(Li)	τ (Gyr)	τ_{min}	τ_{max}	M ($M_{\odot}$)	M_{min}	M_{max}	Planets
HIP91684	MIKE	5528 ± 98	3.78 ± 0.15	−0.161 ± 0.053	0.97	1.03	0.05	5.41	3.64	10.01	1.119	1.011	1.358	no
HIP98813	MIKE	5883 ± 81	4.50 ± 0.14	0.009 ± 0.048	2.04	2.06	0.05	2.97	1.89	6.34	1.047	1.004	1.076	no
HIP103077	UVES	5787 ± 92	3.85 ± 0.19	0.016 ± 0.039	1.85	1.89	0.05	4.97	3.50	7.99	1.118	1.060	1.402	no
HIP103654	UVES	5982 ± 100	4.44 ± 0.16	0.206 ± 0.042	2.05	2.08	0.03	2.23	1.39	4.47	1.119	1.098	1.199	no
HIP105439	UVES	5865 ± 75	4.13 ± 0.22	0.072 ± 0.044	2.50	2.51	0.03	6.36	3.84	8.18	1.086	1.009	1.219	no
HIP105580	UVES	5935 ± 107	4.05 ± 0.20	0.010 ± 0.040	2.10	2.11	0.05	5.72	3.83	7.38	1.067	1.038	1.269	no
HIP106078	UVES	5754 ± 66	4.14 ± 0.10	−0.023 ± 0.025	1.35	1.39	0.05	8.85	7.39	9.93	1.013	0.981	1.079	no
HIP106438	UVES	5743 ± 75	4.11 ± 0.12	−0.042 ± 0.032	1.30	1.34	0.05	8.79	6.92	10.21	1.004	0.971	1.102	no
HIP108158	UVES	5740 ± 89	4.43 ± 0.12	0.101 ± 0.022	0.75	0.75	-1	4.58	2.70	7.97	1.014	0.982	1.054	no
HIP109214	UVES	5914 ± 90	3.86 ± 0.15	−0.153 ± 0.049	1.05	1.07	0.07	4.68	3.47	6.98	1.140	1.083	1.370	no
HIP109488	UVES	5577 ± 106	3.63 ± 0.18	−0.337 ± 0.023	2.15	2.18	0.05	3.32	2.39	8.44	1.118	1.041	1.535	no
HIP111274	UVES	5550 ± 75	3.77 ± 0.11	−0.241 ± 0.050	1.45	1.50	0.05	4.90	3.60	8.50	1.160	1.032	1.348	no
HIP112414	UVES	5744 ± 71	4.09 ± 0.10	−0.075 ± 0.046	2.35	2.36	0.03	8.84	7.11	10.26	1.008	0.976	1.101	no
HIP115577	UVES	5648 ± 64	4.08 ± 0.08	−0.013 ± 0.019	0.85	0.85	-1	9.70	8.06	11.28	1.009	0.970	1.078	no
HIP49024	UVES	5947 ± 65	4.14 ± 0.11	−0.057 ± 0.048	2.25	2.25	0.05	6.45	5.05	7.16	1.079	1.045	1.148	no
HIP52472	UVES	5839 ± 82	3.96 ± 0.12	0.016 ± 0.032	1.85	1.88	0.05	5.75	4.51	7.58	1.135	1.075	1.277	no
HIP57433	UVES	5942 ± 90	3.83 ± 0.14	−0.299 ± 0.017	2.55	2.53	0.03	4.60	3.36	6.94	1.169	1.074	1.352	no
HIP61173	UVES	5804 ± 107	3.83 ± 0.17	0.021 ± 0.024	2.35	2.37	0.05	4.56	3.32	7.31	1.174	1.096	1.426	no
HIP62661	UVES	5984 ± 94	4.17 ± 0.18	0.067 ± 0.030	2.20	2.21	0.05	5.02	3.39	6.24	1.120	1.069	1.248	no
HIP69796	UVES	5938 ± 86	4.24 ± 0.12	−0.046 ± 0.027	2.15	2.16	0.05	6.10	4.19	7.34	1.061	1.019	1.122	no
HIP71774	UVES	5988 ± 109	3.68 ± 0.18	0.020 ± 0.030	2.25	2.26	0.05	2.79	2.00	4.57	1.451	1.260	1.679	no
HIP72772	UVES	6040 ± 63	4.08 ± 0.09	0.181 ± 0.058	2.40	2.41	0.03	3.78	3.32	4.65	1.316	1.231	1.386	no
HIP72779	UVES	5686 ± 80	4.17 ± 0.11	0.136 ± 0.025	0.95	1.01	0.07	8.76	6.61	10.05	1.021	0.987	1.097	no
HIP73650	UVES	5784 ± 70	4.10 ± 0.10	−0.213 ± 0.026	1.75	1.77	0.05	9.25	7.65	10.79	0.987	0.948	1.062	no
HIP74059	UVES	5604 ± 93	3.92 ± 0.16	0.090 ± 0.043	1.75	1.81	0.05	6.70	4.63	10.19	1.093	1.012	1.290	no
HIP75948	UVES	5715 ± 91	3.66 ± 0.15	−0.282 ± 0.034	2.45	2.45	0.03	3.17	2.36	6.33	1.246	1.124	1.541	no
HIP76906	UVES	5868 ± 66	3.68 ± 0.11	−0.232 ± 0.031	2.35	2.35	0.03	2.97	2.35	4.57	1.411	1.238	1.545	no
HIP77325	UVES	5699 ± 103	3.87 ± 0.17	−0.105 ± 0.048	2.05	2.08	0.05	6.00	4.05	9.73	1.105	1.007	1.313	no
HIP79214	UVES	5745 ± 99	3.52 ± 0.15	−0.333 ± 0.048	1.47	1.28	0.07	2.02	1.53	3.97	1.575	1.282	1.776	no
HIP79524	UVES	5630 ± 77	3.75 ± 0.12	−0.385 ± 0.023	2.25	2.26	0.05	4.69	3.38	8.20	1.118	1.031	1.337	no
HIP80013	UVES	5689 ± 100	4.05 ± 0.24	−0.070 ± 0.028	1.35	1.39	0.05	8.83	5.14	11.31	0.966	0.925	1.167	no
HIP83863	UVES	5895 ± 82	4.05 ± 0.11	−0.077 ± 0.023	2.40	2.40	0.03	6.61	5.42	7.97	1.076	1.041	1.180	no
HIP83874	UVES	5915 ± 82	4.33 ± 0.11	−0.065 ± 0.027	1.85	1.87	0.05	6.05	2.90	10.47	1.013	0.905	1.235	no
HIP86385	UVES	6097 ± 100	4.07 ± 0.16	0.070 ± 0.025	2.45	2.45	0.03	4.05	3.01	5.01	1.189	1.152	1.389	no
HIP87100	UVES	5959 ± 58	4.02 ± 0.08	−0.049 ± 0.044	1.00	1.02	0.07	5.63	4.81	6.52	1.127	1.103	1.227	no
HIP88644	UVES	5768 ± 81	4.04 ± 0.11	−0.085 ± 0.024	1.15	1.18	0.05	7.89	6.23	9.70	1.045	0.996	1.147	no
HIP88782	UVES	5840 ± 94	4.12 ± 0.12	0.135 ± 0.042	2.30	2.33	0.03	6.26	4.70	7.55	1.105	1.059	1.209	no
HIP98222	UVES	5723 ± 79	3.69 ± 0.11	−0.148 ± 0.034	2.40	2.41	0.03	3.16	2.53	5.20	1.401	1.212	1.532	no

A.3 α Centauri A

λ (Å)	Element	χ_l (eV)	log gf	HARPS	MIKE	λ (Å)	Element	χ_l (eV)	log gf	HARPS	MIKE	λ (Å)	Element	χ_l (eV)	log gf	HARPS	MIKE
5044.21	26.0	2.851	-2.058	91.1	89.9	5952.72	26.0	3.980	-1.340	-	93.5	7710.36	26.0	4.220	-1.110	-	95.1
5054.64	26.0	3.640	-1.980	55.8	54.8	5956.69	26.0	0.859	-4.552	64.0	63.7	5197.58	26.0	3.231	-2.220	102.0	101.9
5145.09	26.0	2.200	-3.080	-	75.1	6003.01	26.0	3.880	-1.060	106.5	105.5	5234.62	26.0	3.221	-2.180	105.9	106.7
5187.91	26.0	4.140	-1.260	-	75.1	6027.05	26.0	4.076	-1.090	82.2	81.5	5264.80	26.0	3.230	-3.130	58.6	58.5
5217.92	26.0	3.640	-1.720	-	75.3	6056.00	26.0	4.730	-0.400	92.9	93.1	5414.07	26.0	3.221	-3.580	38.5	38.6
5225.52	26.0	0.110	-4.789	-	94.2	6065.48	26.0	2.609	-1.530	140.5	142.1	5425.26	26.0	3.200	-3.220	61.9	62.6
5228.38	26.0	4.220	-1.190	-	89.2	6079.01	26.0	4.650	-1.020	61.5	61.2	6369.46	26.0	2.891	-4.110	27.1	27.2
5247.05	26.0	0.087	-4.961	84.7	85.1	6082.71	26.0	2.220	-3.570	46.1	46.9	6432.68	26.0	2.891	-3.570	58.1	58.2
5250.21	26.0	0.121	-4.938	-	84.7	6085.26	26.0	2.760	-3.050	56.3	57.1	7222.39	26.0	3.889	-3.260	-	44.8
5253.46	26.0	3.280	-1.570	97.8	-	6093.64	26.0	4.607	-1.300	42.9	43.7	7449.33	26.0	3.890	-3.270	-	33.8
5285.13	26.0	4.430	-1.540	36.6	-	6096.67	26.0	3.984	-1.810	53.8	52.6	7515.83	26.0	3.903	-3.390	-	19.9
5288.52	26.0	3.690	-1.510	-	82.3	6127.91	26.0	4.140	-1.400	61.0	60.3	7711.72	26.0	3.903	-2.500	-	65.9
5293.96	26.0	4.140	-1.770	40.8	40.7	6151.62	26.0	2.176	-3.282	62.3	60.7	5052.17	06.0	7.685	-1.304	49.5	47.7
5295.31	26.0	4.420	-1.590	39.7	39.2	6165.36	26.0	4.143	-1.460	60.3	58.7	5380.34	06.0	7.685	-1.615	33.9	34.8
5373.71	26.0	4.470	-0.740	76.7	-	6170.51	26.0	4.800	-0.380	109.2	109.7	7111.47	06.0	8.640	-1.074	-	29.1
5379.57	26.0	3.690	-1.510	76.1	78.0	6173.33	26.0	2.223	-2.880	83.9	84.6	7115.17	06.0	8.650	-0.930	-	78.0
5386.33	26.0	4.150	-1.670	44.9	44.8	6180.20	26.0	2.730	-2.630	-	79.4	7116.96	06.0	8.650	-0.910	-	33.8
5441.34	26.0	4.310	-1.630	47.2	47.8	6187.99	26.0	3.940	-1.620	62.5	62.4	4751.82	11.0	2.104	-2.078	22.8	-
5464.28	26.0	4.140	-1.580	50.2	49.6	6200.31	26.0	2.609	-2.416	92.1	91.7	5148.84	11.0	2.102	-2.044	24.0	21.9
5472.71	26.0	4.210	-1.520	57.0	57.1	6213.43	26.0	2.223	-2.520	97.6	98.8	6154.23	11.0	2.102	-1.547	62.3	64.2
5473.90	26.0	4.150	-0.720	95.1	-	6229.23	26.0	2.850	-2.830	53.1	52.9	6160.75	11.0	2.104	-1.246	85.4	88.1
5483.10	26.0	4.150	-1.450	60.2	61.2	6232.64	26.0	3.650	-1.220	103.0	104.2	4730.04	12.0	4.340	-2.390	98.9	-
5487.15	26.0	4.420	-1.430	-	63.9	6240.65	26.0	2.223	-3.287	62.1	63.8	5711.09	12.0	4.345	-1.729	128.4	132.4
5491.83	26.0	4.186	-2.188	-	25.9	6252.56	26.0	2.404	-1.687	141.2	142.1	6318.72	12.0	5.108	-1.945	79.1	80.7
5522.45	26.0	4.210	-1.450	58.2	58.6	6265.13	26.0	2.176	-2.547	101.5	101.5	6319.24	12.0	5.108	-2.324	62.2	60.5
5525.54	26.0	4.230	-1.120	75.5	74.0	6270.23	26.0	2.858	-2.540	67.9	68.6	5557.07	13.0	3.140	-2.210	21.9	20.7
5543.94	26.0	4.220	-1.040	79.4	79.9	6297.79	26.0	2.223	-2.715	90.9	91.7	6696.02	13.0	3.143	-1.481	59.9	62.0
5546.51	26.0	4.370	-1.210	70.1	-	6322.69	26.0	2.590	-2.430	91.7	92.4	6698.67	13.0	3.143	-1.782	39.2	39.3
5560.21	26.0	4.430	-1.090	65.4	65.8	6380.74	26.0	4.190	-1.320	67.6	69.3	7835.31	13.0	4.022	-0.689	-	86.2
5584.76	26.0	3.570	-2.220	-	63.9	6419.95	26.0	4.730	-0.240	109.3	110.2	7836.13	13.0	4.021	-0.450	-	111.0
5618.63	26.0	4.210	-1.270	64.9	65.3	6430.85	26.0	2.176	-2.006	138.2	137.4	5488.98	14.0	5.614	-1.690	44.5	52.5
5619.60	26.0	4.390	-1.600	54.9	-	6481.87	26.0	2.280	-2.980	83.1	82.5	5517.54	14.0	5.080	-2.496	23.2	24.0
5633.95	26.0	4.990	-0.230	89.3	-	6498.94	26.0	0.958	-4.695	61.9	61.7	5645.61	14.0	4.930	-2.043	60.7	56.8
5635.82	26.0	4.260	-1.790	47.9	48.5	6518.37	26.0	2.831	-2.448	72.7	73.6	5665.55	14.0	4.920	-1.940	58.5	57.7
5638.26	26.0	4.220	-0.770	95.6	95.7	6574.23	26.0	0.990	-5.010	40.4	40.9	5684.48	14.0	4.954	-1.553	84.3	81.1
5650.71	26.0	5.090	-0.860	53.1	52.0	6593.87	26.0	2.433	-2.394	106.1	108.1	5690.42	14.0	4.930	-1.773	71.9	72.1
5651.47	26.0	4.473	-1.750	27.1	26.8	6597.56	26.0	4.800	-0.970	61.7	62.7	5701.10	14.0	4.930	-1.953	55.8	59.5
5653.87	26.0	4.390	-1.540	53.7	52.9	6609.11	26.0	2.559	-2.682	82.2	82.3	5753.64	14.0	5.620	-1.333	84.6	-
5661.35	26.0	4.284	-1.756	33.6	33.1	6699.14	26.0	4.593	-2.101	13.9	14.0	5772.15	14.0	5.082	-1.653	80.2	81.9
5679.02	26.0	4.652	-0.750	75.8	75.3	6703.57	26.0	2.759	-3.023	52.1	52.3	5793.07	14.0	4.930	-1.963	65.5	64.1
5696.09	26.0	4.548	-1.720	19.6	19.9	6705.10	26.0	4.607	-0.980	63.7	63.5	5797.87	14.0	4.950	-1.912	65.4	68.6
5701.54	26.0	2.559	-2.163	104.3	105.3	6713.75	26.0	4.795	-1.400	31.5	32.4	5948.54	14.0	5.080	-1.208	115.6	117.2
5705.46	26.0	4.301	-1.355	54.1	53.5	6726.67	26.0	4.607	-1.030	59.9	60.6	6125.03	14.0	5.610	-1.510	54.6	51.3
5717.83	26.0	4.280	-1.030	87.1	86.8	6739.52	26.0	1.557	-4.794	19.1	19.4	6142.49	14.0	5.620	-1.540	53.8	55.0
5731.76	26.0	4.260	-1.200	71.3	71.4	6750.15	26.0	2.424	-2.621	90.1	90.3	6145.02	14.0	5.610	-1.480	61.4	60.5
5775.08	26.0	4.220	-1.300	74.0	73.8	6752.71	26.0	4.640	-1.220	52.4	53.9	6155.14	14.0	5.620	-0.720	-	129.8
5778.45	26.0	2.588	-3.440	30.7	30.2	6793.26	26.0	4.076	-2.326	20.0	19.7	6195.46	14.0	5.870	-1.666	38.5	39.3
5784.66	26.0	3.396	-2.532	41.2	-	6810.26	26.0	4.607	-0.986	66.9	67.1	6237.33	14.0	5.610	-1.116	99.3	111.7
5793.91	26.0	4.220	-1.619	46.1	45.5	6828.59	26.0	4.640	-0.820	72.6	74.3	6243.82	14.0	5.620	-1.310	67.6	79.9
5806.73	26.0	4.610	-0.950	74.0	73.5	6837.01	26.0	4.593	-1.687	25.3	24.7	6244.48	14.0	5.610	-1.360	68.6	73.2
5809.22	26.0	3.883	-1.710	67.0	65.4	6841.34	26.0	4.610	-0.710	91.2	89.7	6527.21	14.0	5.870	-1.227	72.4	75.5
5852.22	26.0	4.550	-1.230	58.8	59.6	6842.69	26.0	4.640	-1.220	55.5	56.0	6721.84	14.0	5.863	-1.060	74.9	77.2
5855.08	26.0	4.608	-1.478	32.4	32.0	6843.66	26.0	4.550	-0.830	79.3	80.6	6741.64	14.0	5.984	-1.653	32.4	34.7
5856.09	26.0	4.290	-1.460	46.1	46.4	6854.82	26.0	4.593	-1.926	-	21.1	7034.90	14.0	5.871	-0.783	-	109.2
5905.67	26.0	4.650	-0.690	76.3	-	6855.16	26.0	4.560	-0.740	96.1	95.2	7226.21	14.0	5.614	-1.413	-	60.6
5909.97	26.0	3.210	-2.600	61.6	62.2	6858.15	26.0	4.610	-0.940	68.1	68.2	7405.77	14.0	5.614	-0.720	-	125.6
5916.25	26.0	2.450	-2.990	74.9	75.6	6945.21	26.0	2.424	-2.454	-	106.7	7415.96	14.0	5.610	-0.850	-	116.9
5927.79	26.0	4.650	-0.990	54.1	53.9	6978.85	26.0	2.484	-2.479	-	101.3	7423.52	14.0	5.620	-0.650	-	135.9
5929.68	26.0	4.550	-1.310	57.8	58.5	7090.38	26.0	4.230	-1.110	-	90.0	7760.64	14.0	6.200	-1.370	-	31.3
5930.18	26.0	4.650	-0.170	117.1	117.7	7401.69	26.0	4.186	-1.500	-	57.3	4694.11	16.0	6.525	-1.673	30.8	-
5934.65	26.0	3.930	-1.070	99.9	101.5	7418.67	26.0	4.140	-1.380	-	67.3	4695.44	16.0	6.525	-1.829	12.4	-

Table A.4: Linelist used for the analysis of the α Centauri A HARPS and MIKE data

λ (Å)	Element	χ_i (eV)	log gf	HARPS	MIKE	λ (Å)	Element	χ_i (eV)	log gf	HARPS	MIKE	λ (Å)	Element	χ_i (eV)	log gf	HARPS	MIKE
6046.00	16.0	7.868	-0.100	38.7	31.7	5224.30	22.0	2.134	1.349	59.6	64.8	4827.45	23.0	0.040	-1.478	24.6	-
6052.66	16.0	7.870	-0.400	26.1	-	5247.29	22.0	2.103	0.229	17.9	15.6	4875.49	23.0	0.040	-0.806	71.0	-
6743.54	16.0	7.866	-0.600	-	17.8	5252.10	22.0	0.048	0.004	59.5	83.1	4881.56	23.0	0.069	-0.657	80.2	-
6757.17	16.0	7.870	-0.353	25.3	38.2	5295.77	22.0	1.067	0.026	20.7	19.8	5670.85	23.0	1.081	-0.425	30.0	29.4
4512.27	20.0	2.526	-1.901	38.3	-	5299.98	22.0	1.050	0.034	33.5	38.3	5703.59	23.0	1.051	-0.212	50.7	50.5
5260.39	20.0	2.521	-1.719	49.9	55.1	5426.26	22.0	0.020	0.001	10.9	12.4	5727.05	23.0	1.081	-0.012	54.4	56.2
5261.71	20.0	2.520	-0.677	136.1	133.0	5471.20	22.0	1.440	0.040	14.3	14.9	5731.25	23.0	1.051	-0.875	13.7	-
5349.47	20.0	2.710	-0.581	116.8	126.8	5474.23	22.0	1.460	0.059	19.4	24.5	5731.25	23.0	1.064	-0.732	18.9	19.9
5512.98	20.0	2.930	-0.559	120.2	121.4	5474.46	22.0	2.340	0.141	6.9	7.4	5737.06	23.0	1.064	-0.736	20.1	-
5867.56	20.0	2.933	-1.570	36.9	38.8	5490.15	22.0	1.460	0.133	36.3	31.4	6039.73	23.0	1.064	-0.652	20.7	22.9
6156.02	20.0	2.520	-2.497	18.5	27.2	5503.90	22.0	2.580	0.605	29.7	31.4	6081.44	23.0	1.051	-0.579	24.9	27.3
6161.30	20.0	2.523	-1.266	90.6	94.4	5648.57	22.0	2.490	0.389	16.4	15.4	6090.21	23.0	1.081	-0.062	49.9	48.0
6163.75	20.0	2.521	-1.286	78.6	80.6	5662.15	22.0	2.318	1.023	38.8	45.3	6111.65	23.0	1.043	-0.714	18.4	19.3
6166.44	20.0	2.521	-1.142	87.0	86.0	5689.46	22.0	2.297	0.437	24.0	19.8	6119.53	23.0	1.064	-0.320	32.7	39.4
6169.04	20.0	2.523	-0.797	115.1	118.9	5702.66	22.0	2.292	0.257	12.9	17.9	6135.36	23.0	1.051	-0.746	18.4	19.1
6449.82	20.0	2.520	-0.733	124.3	139.9	5716.44	22.0	2.297	0.191	11.5	13.7	6199.19	23.0	0.287	-1.286	-	24.2
6455.60	20.0	2.523	-1.340	70.7	76.1	5737.07	22.0	1.060	0.153	20.1	19.5	6216.36	23.0	0.275	-0.830	-	58.3
6471.66	20.0	2.526	-0.686	112.3	111.9	5739.46	22.0	2.249	0.251	12.0	12.8	6224.51	23.0	0.290	-1.935	9.1	11.6
6499.65	20.0	2.523	-0.818	105.0	105.5	5766.33	22.0	3.290	2.118	15.6	16.3	6242.83	23.0	0.262	-1.553	-	19.2
6572.80	20.0	0.000	-4.280	60.1	48.5	5866.45	22.0	1.066	0.145	65.2	74.0	6243.11	23.0	0.301	-0.979	-	53.2
4743.82	21.0	1.448	2.642	17.4	-	5953.17	22.0	1.890	0.537	52.9	55.8	6251.82	23.0	0.287	-1.343	-	25.6
5081.56	21.0	1.448	2.944	14.9	12.5	5965.84	22.0	1.880	0.322	44.8	63.7	6274.65	23.0	0.267	-1.674	-	14.3
5520.50	21.0	1.870	3.648	12.6	16.9	5978.55	22.0	1.870	0.250	45.7	41.6	6285.16	23.0	0.275	-1.513	-	28.7
5671.83	21.0	1.448	3.126	24.1	22.1	6064.63	22.0	1.050	0.011	13.1	16.3	6292.82	23.0	0.287	-1.471	-	19.7
5686.86	21.0	1.439	2.377	20.3	15.8	6091.18	22.0	2.267	0.427	23.1	28.0	6531.41	23.0	1.218	-0.836	16.4	15.0
5318.37	21.1	1.357	0.010	-	21.5	6126.22	22.0	1.066	0.038	32.0	31.6	4511.90	24.0	3.090	0.407	59.8	-
5526.82	21.1	1.770	1.380	100.3	97.8	6258.10	22.0	1.443	0.502	64.4	68.9	4535.13	24.0	2.544	0.102	50.0	-
5667.88	21.1	1.510	0.472	88.3	92.1	6261.10	22.0	1.429	0.332	69.2	70.9	4541.06	24.0	2.545	0.072	43.4	-
5667.14	21.1	1.500	0.094	60.4	61.7	6303.75	22.0	1.443	0.031	13.1	-	4545.94	24.0	0.940	0.049	113.3	-
5669.06	21.1	1.500	0.063	59.2	58.0	6312.23	22.0	1.460	0.032	11.6	11.3	4575.11	24.0	3.370	0.099	21.3	-
5684.21	21.1	1.507	0.084	61.1	60.8	6599.10	22.0	0.900	0.009	14.8	19.2	4600.75	24.0	1.000	0.035	99.1	-
6245.64	21.1	1.507	0.092	49.4	51.0	6743.13	22.0	0.899	0.023	30.6	38.9	4626.18	24.0	0.970	0.034	103.8	-
6320.84	21.1	1.500	0.012	21.1	23.4	7357.73	22.0	1.443	0.086	-	40.4	4633.26	24.0	3.125	0.078	18.8	-
6604.58	21.1	1.357	0.049	53.0	55.8	7949.15	22.0	1.500	0.035	-	38.4	4700.60	24.0	2.710	0.056	22.3	-
4512.73	22.0	0.840	0.380	85.0	-	8426.50	22.0	0.826	0.064	-	64.0	4708.02	24.0	3.168	1.230	73.2	-
4518.02	22.0	0.830	0.537	88.9	-	8675.37	22.0	1.067	0.024	-	43.4	4730.72	24.0	3.080	0.452	71.8	-
4555.48	22.0	0.850	0.372	82.2	-	8682.98	22.0	1.053	0.013	-	23.3	4745.27	24.0	2.708	0.042	26.0	-
4562.64	22.0	0.020	0.003	17.7	-	4409.52	22.1	1.231	-2.570	54.2	-	4767.86	24.0	3.560	0.252	26.8	-
4617.28	22.0	1.750	2.818	78.5	-	4444.54	22.1	1.116	-2.210	82.9	-	4775.14	24.0	3.550	0.094	15.4	-
4645.19	22.0	1.730	0.216	48.2	-	4493.52	22.1	1.080	-2.830	56.0	-	4789.34	24.0	2.544	0.449	85.6	-
4656.47	22.0	0.000	0.049	88.4	-	4563.77	22.1	1.220	-0.690	214.9	-	4801.05	24.0	3.122	0.740	65.5	-
4675.11	22.0	1.070	0.115	53.3	-	4583.41	22.1	1.165	-2.870	48.5	-	4885.73	24.0	2.544	0.088	49.9	-
4722.61	22.0	1.050	0.037	30.3	-	4609.27	22.1	1.180	-3.430	25.2	-	4936.34	24.0	3.113	0.579	59.9	62.8
4758.12	22.0	2.249	3.027	58.2	-	4636.32	22.1	1.165	-3.020	35.8	-	4953.71	24.0	3.122	0.033	10.7	-
4759.27	22.0	2.256	3.715	59.6	-	4657.21	22.1	1.243	-2.320	72.8	-	4964.93	24.0	0.940	0.003	57.2	58.4
4778.26	22.0	2.236	0.603	26.7	-	4705.62	22.1	5.648	-1.830	66.0	-	5214.14	24.0	3.370	0.164	26.6	23.4
4820.41	22.0	1.500	0.407	58.3	-	4708.66	22.1	1.237	-2.370	69.9	-	5220.91	24.0	3.385	0.129	18.7	-
4840.88	22.0	0.900	0.355	83.7	-	4719.53	22.1	1.243	-3.280	21.4	-	5238.96	24.0	2.710	0.037	26.1	27.8
4874.88	22.0	3.320	0.407	48.4	-	4749.55	22.1	5.638	-1.780	69.6	-	5241.45	24.0	2.710	0.012	9.0	8.7
4913.62	22.0	1.870	1.660	68.8	72.6	4764.52	22.1	1.237	-2.770	50.3	-	5247.57	24.0	0.960	0.024	100.4	98.9
4964.71	22.0	1.969	0.151	14.5	20.8	4798.53	22.1	1.080	-2.670	59.5	-	5272.01	24.0	3.449	0.379	35.8	35.0
4997.10	22.0	0.000	0.007	44.9	43.9	4865.61	22.1	1.116	-2.810	57.9	-	5287.20	24.0	3.438	0.129	17.8	15.8
5016.16	22.0	0.850	0.302	77.8	84.7	4874.01	22.1	3.095	-0.800	48.7	-	5296.69	24.0	0.983	0.039	115.0	116.2
5022.87	22.0	0.826	0.419	95.0	88.3	4911.20	22.1	3.120	-0.610	78.4	92.9	5297.39	24.0	2.900	1.000	105.2	135.8
5024.85	22.0	0.818	0.275	94.6	86.1	5005.16	22.1	1.566	-2.720	34.1	32.0	5300.74	24.0	0.983	0.008	78.9	79.6
5039.96	22.0	0.020	0.063	94.3	110.1	5145.69	22.1	5.424	-1.180	9.2	-	5304.18	24.0	3.464	-0.681	-	22.9
5064.06	22.0	2.690	0.338	10.0	15.5	5154.08	22.1	1.570	-1.750	106.8	107.7	5312.87	24.0	3.449	-0.556	-	29.4
5071.49	22.0	1.460	0.160	44.1	45.3	5185.91	22.1	1.890	-1.490	75.3	79.3	5318.81	24.0	3.438	-0.679	-	27.0
5087.06	22.0	1.430	0.166	-	54.5	5211.53	22.1	2.590	-1.160	49.9	45.5	5340.47	24.0	3.468	0.186	38.2	-
5113.44	22.0	1.443	0.187	40.0	52.5	5336.78	22.1	1.582	-1.630	-	91.4	5480.51	24.0	3.500	0.120	18.2	14.7
5145.46	22.0	1.460	0.303	57.1	50.9	5381.02	22.1	1.566	-1.970	90.2	85.1	5574.39	24.0	4.450	0.191	8.0	5.7
5147.48	22.0	0.000	0.011	52.0	-	5418.77	22.1	1.582	-2.110	66.8	64.0	5628.62	24.0	3.422	0.175	23.2	22.8
5152.18	22.0	0.021	0.011	51.1	51.3	5490.69	22.1	1.566	-2.430	30.2	29.6	5719.81	24.0	3.013	0.024	12.1	-
5186.33	22.0	2.117	0.170	10.6	-	6606.98	22.1	2.061	-2.760	15.1	14.5	5781.16	24.0	3.011	0.100	26.1	28.7
5219.70	22.0	0.021	0.006	40.2	41.8	4586.37	23.0	0.040	-0.793	63.9	-	5783.07	24.0	3.232	0.331	44.6	46.7
5223.62	22.0	2.092	0.324	-	28.8	4594.12	23.0	0.069	-0.672	76.3	-	5783.87	24.0	3.322	0.513	62.7	65.5

λ (Å)	Element	χ (eV)	log gf	HARPS	MIKE
5785.02	24.0	3.321	-0.380	-	56.2
5787.93	24.0	3.322	0.832	60.9	58.8
5844.59	24.0	3.013	0.017	7.9	8.1
6330.10	24.0	0.941	0.001	40.2	36.9
6661.08	24.0	4.190	0.583	18.6	20.7
6882.48	24.0	3.438	0.422	46.8	43.7
6883.00	24.0	3.438	0.380	44.7	46.9
4554.99	24.1	4.071	-1.249	59.0	-
4588.20	24.1	4.071	-0.594	90.5	-
4592.05	24.1	4.070	-1.252	61.6	-
4616.63	24.1	4.073	-1.210	70.6	-
4848.24	24.1	3.864	-1.160	81.6	-
4884.61	24.1	3.860	-2.069	41.4	-
5237.33	24.1	4.073	-1.087	70.2	70.6
5246.77	24.1	3.714	-2.436	27.1	25.8
5279.88	24.1	4.073	-1.909	38.8	42.8
5305.87	24.1	3.827	-1.970	-	39.1
5308.42	24.1	4.070	-1.790	-	38.5
5310.69	24.1	4.072	-2.144	-	24.6
5313.56	24.1	4.073	-1.473	-	53.0
5502.07	24.1	4.168	-2.049	28.1	27.8
4709.71	25.0	2.888	0.324	94.1	-
4739.11	25.0	2.941	0.251	77.3	-
5004.89	25.0	2.920	0.023	-	22.8
5255.33	25.0	3.133	0.135	67.6	78.3
5377.62	25.0	3.840	0.855	66.5	73.4
5399.47	25.0	3.850	0.787	54.2	58.2
5413.67	25.0	3.860	0.334	39.5	41.3
6021.80	25.0	3.070	1.072	120.5	120.0
4792.86	27.0	3.250	0.708	50.3	-
4813.48	27.0	3.220	1.503	73.2	-
5212.69	27.0	3.514	0.776	34.4	31.8
5280.63	27.0	3.629	0.933	30.6	30.4
5301.04	27.0	1.710	0.011	35.1	35.2
5342.71	27.0	4.020	3.467	46.0	48.7
5352.04	27.0	3.576	1.148	40.7	42.5
5359.20	27.0	4.150	1.096	19.0	17.2
5483.35	27.0	1.710	0.039	71.4	71.7
5530.77	27.0	1.710	0.006	35.0	27.4
5647.23	27.0	2.280	0.028	24.0	21.9
6082.42	27.0	3.514	0.302	22.1	22.8
6093.14	27.0	1.740	0.004	17.6	17.7
6189.00	27.0	1.710	0.004	15.2	17.1
6455.00	27.0	3.632	0.562	26.6	27.9
6814.95	27.0	1.960	0.015	35.0	40.7
4686.22	28.0	3.600	0.263	102.7	-
4740.17	28.0	3.480	0.019	28.7	-
4811.98	28.0	3.658	0.026	48.2	-
4814.60	28.0	3.597	0.024	35.3	-
4831.18	28.0	3.610	0.479	89.6	-
4853.78	28.0	3.543	0.028	52.0	-
4857.40	28.0	3.740	0.148	75.4	-
4866.27	28.0	3.539	0.617	99.6	-
4874.79	28.0	3.543	0.035	46.7	-
4886.71	28.0	3.706	0.017	28.6	-
4900.97	28.0	3.480	0.021	33.9	-
4904.42	28.0	3.540	0.562	112.4	-
4913.98	28.0	3.740	0.218	79.1	-
4946.04	28.0	3.800	0.060	43.6	44.3
4952.29	28.0	3.610	0.055	43.7	47.5
4953.21	28.0	3.740	0.263	71.8	73.1
4976.13	28.0	3.606	0.056	48.2	49.5
4995.66	28.0	3.630	0.024	28.7	38.9
4998.22	28.0	3.606	0.204	77.0	77.8
5010.94	28.0	3.630	0.126	66.2	62.8
5081.11	28.0	3.850	1.159	123.3	154.9
5082.35	28.0	3.658	0.257	91.1	91.1
5084.11	28.0	3.680	0.871	111.8	114.7
5088.54	28.0	3.850	0.091	47.9	48.8
5088.96	28.0	3.680	0.051	50.2	44.1
5094.42	28.0	3.833	0.085	47.0	43.0
5102.97	28.0	1.680	0.002	80.7	75.4
5115.40	28.0	3.834	0.525	103.3	108.8
5157.98	28.0	3.606	0.031	29.7	27.7
5392.33	28.0	4.150	0.048	22.3	20.3
5435.86	28.0	1.990	0.004	64.5	65.1
5462.50	28.0	3.850	0.132	62.7	64.6
5468.11	28.0	3.850	0.022	20.9	21.3
5504.09	28.0	3.834	0.020	27.4	31.4
5510.01	28.0	3.847	0.126	61.6	78.7
5578.73	28.0	1.677	0.003	77.8	83.4
5587.87	28.0	1.930	0.004	70.9	86.3
5589.36	28.0	3.900	0.071	40.8	39.9
5593.75	28.0	3.899	0.166	57.8	57.3
5625.32	28.0	4.090	0.186	56.8	56.2
5628.35	28.0	4.090	0.048	26.4	29.6
5638.75	28.0	3.900	0.020	19.4	19.7
5641.88	28.0	4.110	0.096	39.7	40.4
5643.08	28.0	4.160	0.058	27.5	24.8
5694.99	28.0	4.090	0.235	59.7	59.9
5748.36	28.0	1.680	0.001	43.0	46.3
5754.67	28.0	1.930	0.014	100.1	98.2
5805.22	28.0	4.168	0.240	59.2	58.9
5996.74	28.0	4.236	0.098	34.6	-
6086.29	28.0	4.266	0.347	64.4	-
6108.12	28.0	1.680	0.004	80.1	-
6111.08	28.0	4.088	0.155	53.4	-
6119.76	28.0	4.270	0.048	16.4	-
6130.14	28.0	4.266	0.115	32.8	-
6133.98	28.0	4.090	0.012	9.6	-
6175.37	28.0	4.089	0.282	71.7	-
6176.80	28.0	4.088	0.550	81.5	-
6186.72	28.0	4.106	0.132	47.3	-
6204.60	28.0	4.088	0.079	34.5	-
6230.10	28.0	4.110	0.074	38.0	-
6314.67	28.0	1.936	0.010	95.1	-
6322.17	28.0	4.154	0.062	28.2	-
6327.60	28.0	1.680	0.001	57.1	-
6360.81	28.0	4.170	0.072	31.1	-
6414.59	28.0	4.154	0.066	28.2	-
6482.81	28.0	1.930	0.002	57.3	-
6598.61	28.0	4.236	0.123	38.3	-
6635.13	28.0	4.420	0.191	36.2	-
6643.64	28.0	1.676	0.009	110.4	-
6767.78	28.0	1.830	0.008	92.8	-
6772.32	28.0	3.658	0.107	65.0	-
6813.61	28.0	5.340	0.468	22.4	-
6842.04	28.0	3.658	0.032	45.8	-
5105.54	29.0	1.390	0.021	109.9	117.8
5218.20	29.0	3.820	1.271	76.8	74.4
5220.07	29.0	3.820	0.167	26.7	28.2
4722.16	30.0	4.030	0.417	102.0	-
4810.53	30.0	4.080	0.692	96.6	-
6362.35	30.0	5.800	1.380	33.4	31.5
4900.12	39.1	1.030	-0.090	71.5	-
5087.42	39.1	1.080	-0.170	64.3	60.5
5119.12	39.1	0.990	-1.360	25.5	25.9
5200.41	39.1	0.990	-0.570	55.7	51.1
5402.78	39.1	1.839	-0.440	20.6	18.4
5112.28	40.1	1.660	-0.590	15.3	19.5
5853.69	56.1	0.600	-0.907	77.2	77.3
6141.73	56.1	0.704	-0.030	139.9	-
6496.91	56.1	0.600	-0.407	118.9	141.4

Bibliography

[1] C. Abia, R. Rebolo, J. E. Beckman, and L. Crivellari. Abundances of light metals and NI in a sample of disc stars. *A&A*, 206:100–107, November 1988.

[2] M. A. Agüeros, S. F. Anderson, K. R. Covey, S. L. Hawley, B. Margon, E. R. Newsom, B. Posselt, N. M. Silvestri, and et al.,. X-Ray-Emitting Stars Identified from the ROSAT All-Sky Survey and the Sloan Digital Sky Survey. *ApJS*, 181:444–465, April 2009.

[3] A. Alibés, J. Labay, and R. Canal. Galactic Cosmic Rays from Superbubbles and the Abundances of Lithium, Beryllium, and Boron. *ApJ*, 571:326–333, May 2002.

[4] C. Allende Prieto, P. S. Barklem, D. L. Lambert, and K. Cunha. S^4N: A spectroscopic survey of stars in the solar neighborhood. The Nearest 15 pc. *A&A*, 420:183–205, June 2004.

[5] C. Amsler et al. Reviews of Particle Physics. *Phys. Lett. B*, 667.

[6] E. Anders and N. Grevesse. Abundances of the elements - Meteoritic and solar. *Geochim. Cosmochim. Acta*, 53:197–214, January 1989.

[7] M. Asplund. New Light on Stellar Abundance Analyses: Departures from LTE and Homogeneity. *ARA&A*, 43:481–530, September 2005.

[8] M. Asplund, N. Grevesse, A. J. Sauval, and P. Scott. The Chemical Composition of the Sun. *ARA&A*, 47:481–522, September 2009.

[9] S. Balachandran. The Lithium Dip in M67: Comparison with the Hyades, Praesepe, and NGC 752 Clusters. *ApJ*, 446:203, June 1995.

[10] S. C. Balachandran, S. V. Mallik, and D. L. Lambert. Lithium abundances in the α Per cluster. *MNRAS*, 410:2526–2539, February 2011.

[11] P. S. Barklem, H. C. Stempels, C. Allende Prieto, O. P. Kochukhov, N. Piskunov, and B. J. O'Mara. Detailed analysis of Balmer lines in cool dwarf stars. *A&A*, 385:951–967, April 2002.

[12] S. A. Barnes. Ages for Illustrative Field Stars Using Gyrochronology: Viability, Limitations, and Errors. *ApJ*, 669:1167–1189, November 2007.

[13] P. Baumann, I. Ramírez, J. Meléndez, M. Asplund, and K. Lind. Lithium depletion in solar-like stars: no planet connection. *A&A*, 519:A87, September 2010.

[14] M. Bazot, F. Bouchy, H. Kjeldsen, S. Charpinet, M. Laymand, and S. Vauclair. Asteroseismology of α Centauri A. Evidence of rotational splitting. *A&A*, 470:295–302, July 2007.

[15] T. Bensby and S. Feltzing. Chemical Evolution of the Galactic Disk(s). In W. Aoki, M. Ishigaki, T. Suda, T. Tsujimoto, and N. Arimoto, editors, *Galactic Archaeology: Near-Field Cosmology and the Formation of the Milky Way*, volume 458 of *Astronomical Society of the Pacific Conference Series*, page 201, August 2012.

[16] T. Bensby, S. Feltzing, I. Lundström, and I. Ilyin. α-, r-, and s-process element trends in the Galactic thin and thick disks. *A&A*, 433:185–203, April 2005.

[17] T. Bensby, A. R. Zenn, M. S. Oey, and S. Feltzing. Tracing the Galactic Thick Disk to Solar Metallicities. *ApJ*, 663:L13–L16, July 2007.

[18] J. Beringer et al. (Particle Data Group). PR D86. *010001*, 2012.

[19] M. S. Bessell. Alpha Centauri. *Proceedings of the Astronomical Society of Australia*, 4:212–214, 1981.

[20] A. M. Boesgaard and M. J. Tripicco. Lithium in the Hyades Cluster. *ApJ*, 302:L49–L53, March 1986.

[21] J. Bouvier. Lithium depletion and the rotational history of exoplanet host stars. *A&A*, 489:L53–L56, October 2008.

[22] H. Bruntt, T. R. Bedding, P.-O. Quirion, G. Lo Curto, F. Carrier, B. Smalley, T. H. Dall, T. Arentoft, M. Bazot, and R. P. Butler. Accurate fundamental parameters for 23 bright solar-type stars. *MNRAS*, 405:1907–1923, July 2010.

[23] M. Carlsson, R. J. Rutten, J. H. M. J. Bruls, and N. G. Shchukina. The non-LTE formation of Li I lines in cool stars. *A&A*, 288:860–882, August 1994.

[24] L. Casagrande, I. Ramírez, J. Meléndez, M. Bessell, and M. Asplund. An absolutely calibrated T_{eff} scale from the infrared flux method. Dwarfs and subgiants. *A&A*, 512:A54+, March 2010.

[25] L. Casagrande, R. Schoenrich, M. Asplund, S. Cassisi, I. Ramirez, J. Melendez, T. Bensby, and S. Feltzing. Geneva-Copenhagen survey re-analysis (Casagrande+, 2011). *VizieR Online Data Catalog*, 353:9138, April 2011.

[26] F. Castelli and R. L. Kurucz. New Grids of ATLAS9 Model Atmospheres. *ArXiv Astrophysics e-prints*, May 2004.

[27] M. Castro, S. Vauclair, O. Richard, and N. C. Santos. Lithium abundances in exoplanet-host stars. *Memorie della Societa Astronomica Italiana*, 79:679–+, 2008.

[28] M. Castro, S. Vauclair, O. Richard, and N. C. Santos. Lithium abundances in exoplanet-host stars: modelling. *A&A*, 494:663–668, February 2009.

[29] R. Cayrel, C. van't Veer-Menneret, N. F. Allard, and C. Stehlé. The Hα Balmer line as an effective temperature criterion. I. Calibration using 1D model stellar atmospheres. *A&A*, 531:A83, July 2011.

[30] B. Chaboyer, P. Demarque, and M. H. Pinsonneault. Stellar models with microscopic diffusion and rotational mixing. 1: Application to the Sun. *ApJ*, 441:865–875, March 1995.

[31] C. Charbonnel and S. Talon. Influence of Gravity Waves on the Internal Rotation and Li Abundance of Solar-Type Stars. *Science*, 309:2189–2191, September 2005.

[32] C. Charbonnel and S. Talon. Deep inside low-mass stars. In L. Deng and K. L. Chan, editors, *IAU Symposium*, volume 252 of *IAU Symposium*, pages 163–174, October 2008.

[33] Y. Q. Chen, P. E. Nissen, T. Benoni, and G. Zhao. Lithium abundances for 185 main-sequence stars: Galactic evolution and stellar depletion of lithium. *A&A*, 371:943–951, June 2001.

[34] Y. Q. Chen and G. Zhao. A Comparative Study on Lithium Abundances in Solar-Type Stars With and Without Planets. *AJ*, 131:1816–1821, March 2006.

[35] Y. Chmielewski, E. Friel, G. Cayrel de Strobel, and C. Bentolila. The 1992 detailed analyses of Alpha Centauri A and Alpha Centauri B. *A&A*, 263:219–231, September 1992.

[36] A. Coc, S. Goriely, Y. Xu, M. Saimpert, and E. Vangioni. Standard Big Bang Nucleosynthesis up to CNO with an Improved Extended Nuclear Network. *ApJ*, 744:158, January 2012.

[37] F. D'Antona and I. Mazzitelli. Evolution of low mass stars. *Mem. Soc. Astron. Italiana*, 68:807, 1997.

[38] F. D'Antona, P. Ventura, I. Mazzitelli, and A. Zeppieri. Lithium burning in solar like stars. *Mem. Soc. Astron. Italiana*, 69:575, 1998.

[39] E. F. del Peloso, L. da Silva, and G. F. Porto de Mello. The age of the Galactic thin disk from Th/Eu nucleocosmochronology. I. Determination of [Th/Eu] abundance ratios. *A&A*, 434:275–300, April 2005.

[40] P. Demarque, J.-H. Woo, Y.-C. Kim, and S. K. Yi. Y^2 Isochrones with an Improved Core Overshoot Treatment. *ApJS*, 155:667–674, December 2004.

[41] P. R. Demarque and R. B. Larson. The Age of Galactic Cluster NGC 188. *ApJ*, 140:544, August 1964.

[42] J. D. Do Nascimento, J. S. da Costa, and J. R. de Medeiros. Rotation and lithium abundance of solar-analog stars. Theoretical analysis of observations. *A&A*, 519:A101, September 2010.

[43] J. D. Do Nascimento, Jr., M. Castro, J. Meléndez, M. Bazot, S. Théado, G. F. Porto de Mello, and J. R. de Medeiros. Age and mass of solar twins constrained by lithium abundance. *A&A*, 501:687–694, July 2009.

[44] M. T. Doyle, B. J. O'Mara, J. E. Ross, and M. S. Bessell. The Chemical Composition of α Cen A: Strong Lines and the ABO Theory of Collisional Line Broadening. *PASA*, 22:6–12, 2005.

[45] D. Dravins, L. Lindegren, A. Nordlund, and D. A. Vandenberg. The distant future of solar activity: A case study of Beta Hydri. I - Stellar evolution, lithium abundance, and photospheric structure. *ApJ*, 403:385–395, January 1993.

[46] X. Dumusque, F. Pepe, C. Lovis, D. Ségransan, J. Sahlmann, W. Benz, F. Bouchy, M. Mayor, D. Queloz, N. Santos, and S. Udry. An Earth-mass planet orbiting α Centauri B. *Nature*, 491:207–211, November 2012.

[47] A. S. Eddington. *The Internal Constitution of the Stars*. 1926.

[48] B. Edvardsson. Spectroscopic surface gravities and chemical compositions for 8 nearby single sub-giants. *A&A*, 190:148–166, January 1988.

[49] B. Edvardsson, J. Andersen, B. Gustafsson, D. L. Lambert, P. E. Nissen, and J. Tomkin. The Chemical Evolution of the Galactic Disk - Part One - Analysis and Results. *A&A*, 275:101–+, August 1993.

[50] P. Eggenberger, C. Charbonnel, S. Talon, G. Meynet, A. Maeder, F. Carrier, and G. Bourban. Analysis of α Centauri AB including seismic constraints. *A&A*, 417:235–246, April 2004.

[51] P. Eggenberger, G. Meynet, A. Maeder, R. Hirschi, C. Charbonnel, S. Talon, and S. Ekström. The Geneva stellar evolution code. *Ap&SS*, 316:43–54, August 2008.

[52] M. N. England. A spectroscopic analysis of the Alpha Centauri system. *MNRAS*, 191:23–35, April 1980.

[53] B. D. Fields. The Primordial Lithium Problem. *Annual Review of Nuclear and Particle Science*, 61:47–68, November 2011.

[54] D. A. Fischer and J. Valenti. The Planet-Metallicity Correlation. *ApJ*, 622:1102–1117, April 2005.

[55] A. Ford, R. D. Jeffries, D. J. James, and J. R. Barnes. Lithium in the Coma Berenices open cluster. *A&A*, 369:871–881, April 2001.

[56] A. Ford, R. D. Jeffries, and B. Smalley. Elemental abundances in the Blanco 1 open cluster. *MNRAS*, 364:272–282, November 2005.

[57] V. A. French and A. L. T. Powell. An abundance analysis of alpha Centauri. *Royal Greenwich Observatory Bulletin*, 173:63–103, 1971.

[58] J. R. Fuhr and W. L. Wiese. A Critical Compilation of Atomic Transition Probabilities for Neutral and Singly Ionized Iron. *J. Phys. Chem. Ref.*, 35:1669, December 2006.

[59] I. Furenlid and T. Meylan. An abundance analysis of Alpha Centauri A. *ApJ*, 350:827–838, February 1990.

[60] E. J. Gaidos, G. W. Henry, and S. M. Henry. Spectroscopy and Photometry of Nearby Young Solar Analogs. *AJ*, 120:1006–1013, August 2000.

[61] L. Goldberg, E. A. Muller, and L. H. Aller. The Abundances of the Elements in the Solar Atmosphere. *ApJS*, 5:1, November 1960.

[62] V. M. Goldschmidt. Skrifter Norske Videnskaps-Akad. *"Oslo I Math.-Naturv. Klasse"*, 4, 1938.

[63] G. Gonzalez. The stellar metallicity-giant planet connection. *MNRAS*, 285:403–412, February 1997.

[64] G. Gonzalez. Spectroscopic analyses of the parent stars of extrasolar planetary system candidates. *A&A*, 334:221–238, June 1998.

[65] G. Gonzalez. Parent stars of extrasolar planets - IX. Lithium abundances. *MNRAS*, 386:928–934, May 2008.

[66] G. Gonzalez and C. Laws. Parent Stars of Extrasolar Planets. V. HD 75289. *AJ*, 119:390–396, January 2000.

[67] G. Gonzalez, C. Laws, S. Tyagi, and B. E. Reddy. Parent Stars of Extrasolar Planets. VI. Abundance Analyses of 20 New Systems. *AJ*, 121:432–452, January 2001.

[68] J. I. González Hernández, G. Israelian, N. C. Santos, S. Sousa, E. Delgado-Mena, V. Neves, and S. Udry. Searching for the Signatures of Terrestrial Planets in Solar Analogs. *ApJ*, 720:1592–1602, September 2010.

[69] R. G. Gratton and C. Sneden. Light element and NI abundance in field disk and halo stars. *A&A*, 178:179–193, May 1987.

[70] N. Grevesse and A. J. Sauval. Standard Solar Composition. *Space Sci. Rev.*, 85:161–174, May 1998.

[71] E. F. Guinan and S. G. Engle. The Sun in time: age, rotation, and magnetic activity of the Sun and solar-type stars and effects on hosted planets. In *IAU Symposium*, volume 258, pages 395–408, June 2009.

[72] B. Gustafsson, B. Edvardsson, K. Eriksson, U. G. Jørgensen, Å. Nordlund, and B. Plez. A grid of MARCS model atmospheres for late-type stars. I. Methods and general properties. *A&A*, 486:951–970, August 2008.

[73] U. Heiter and R. E. Luck. Abundance Analysis of Planetary Host Stars. I. Differential Iron Abundances. *AJ*, 126:2015–2036, October 2003.

[74] L. M. Hobbs, J. A. Thorburn, and L. M. Rebull. Lithium Isotope Ratios in Halo Stars. III. *ApJ*, 523:797–804, October 1999.

[75] A. Ibukiyama and N. Arimoto. HIPPARCOS age-metallicity relation of the solar neighbourhood disc stars. *A&A*, 394:927–941, November 2002.

[76] G. Israelian, E. Delgado Mena, N. C. Santos, S. G. Sousa, M. Mayor, S. Udry, C. Domínguez Cerdeña, R. Rebolo, and et al.,. Enhanced lithium depletion in Sun-like stars with orbiting planets. *Nature*, 462:189–191, November 2009.

[77] G. Israelian, N. C. Santos, M. Mayor, and R. Rebolo. Lithium in stars with exoplanets. *A&A*, 414:601–611, February 2004.

[78] B. F. Jones, D. Fischer, M. Shetrone, and D. R. Soderblom. The Evolution of the Lithium Abundances of Solar-Type Stars.VII.M34 (NGC 1039) and the Role of Rotation in Lithium Depletion. *AJ*, 114:352–362, July 1997.

[79] J. R. King, A. M. Boesgaard, and S. C. Schuler. Keck HIRES Spectroscopy of Four Candidate Solar Twins. *AJ*, 130:2318–2325, November 2005.

[80] C. Kobayashi, H. Umeda, K. Nomoto, N. Tominaga, and T. Ohkubo. Galactic Chemical Evolution: Carbon through Zinc. *ApJ*, 653:1145–1171, December 2006.

[81] R. L. Kurucz. Model atmospheres for G, F, A, B, and O stars. *ApJS*, 40:1–340, May 1979.

[82] R. L. Kurucz and E. Peytremann. A table of semiempirical gf values. Part 1: Wavelengths: 5.2682 NM to 272.3380 NM. *SAO Special Report*, 362, February 1975.

[83] N. Lagarde, T. Decressin, C. Charbonnel, P. Eggenberger, S. Ekström, and A. Palacios. Thermohaline instability and rotation-induced mixing. III. Grid of stellar models and asymptotic asteroseismic quantities from the pre-main sequence up to the AGB for low- and intermediate-mass stars of various metallicities. *A&A*, 543:A108, July 2012.

[84] D. L. Lambert, J. E. Heath, and B. Edvardsson. Lithium abundances for 81 F dwarfs. *MNRAS*, 253:610–618, December 1991.

[85] D. L. Lambert and B. E. Reddy. Lithium abundances of the local thin disc stars. *MNRAS*, 349:757–767, April 2004.

[86] D. W. Latham, J. F. Rowe, S. N. Quinn, N. M. Batalha, W. J. Borucki, T. M. Brown, S. T. Bryson, L. A. Buchhave, D. A. Caldwell, J. A. Carter, J. L. Christiansen, D. R. Ciardi, W. D. Cochran, E. W. Dunham, D. C. Fabrycky, E. B. Ford, T. N. Gautier, III, R. L. Gilliland, M. J. Holman, S. B. Howell, K. A. Ibrahim, H. Isaacson, J. M. Jenkins, D. G. Koch, J. J. Lissauer, G. W. Marcy, E. V. Quintana, D. Ragozzine, D. Sasselov, A. Shporer, J. H. Steffen, W. F. Welsh, and B. Wohler. A First Comparison of Kepler Planet Candidates in Single and Multiple Systems. *ApJ*, 732:L24, May 2011.

[87] K. Lind, M. Asplund, and P. S. Barklem. Departures from LTE for neutral Li in late-type stars. *A&A*, 503:541–544, August 2009.

[88] K. Lodders. Solar System Abundances and Condensation Temperatures of the Elements. *ApJ*, 591:1220–1247, July 2003.

[89] K. Lodders, H. Palme, and H.-P. Gail. Abundances of the Elements in the Solar System. *Landolt Börnstein*, page 44, 2009.

[90] R. E. Luck and U. Heiter. Dwarfs in the Local Region. *AJ*, 131:3069–3092, June 2006.

[91] A. Maeder and G. Meynet. Diffusive mixing by shears in rotating stars. *A&A*, 313:140–144, September 1996.

[92] A. Maeder and J.-P. Zahn. Stellar evolution with rotation. III. Meridional circulation with MU -gradients and non-stationarity. *A&A*, 334:1000–1006, June 1998.

[93] E. E. Mamajek and L. A. Hillenbrand. Improved Age Estimation for Solar-Type Dwarfs Using Activity-Rotation Diagnostics. *ApJ*, 687:1264–1293, November 2008.

[94] M. Mayor and D. Queloz. A Jupiter-mass companion to a solar-type star. *Nature*, 378:355–359, November 1995.

[95] A. McWilliam. Abundance Ratios and Galactic Chemical Evolution. *ARA&A*, 35:503–556, 1997.

[96] J. Meléndez, M. Asplund, B. Gustafsson, and D. Yong. The Peculiar Solar Composition and Its Possible Relation to Planet Formation. *ApJ*, 704:L66–L70, October 2009.

[97] J. Meléndez and B. Barbuy. Keck NIRSPEC Infrared OH Lines: Oxygen Abundances in Metal-poor Stars down to [Fe/H] = -2.9. *ApJ*, 575:474–483, August 2002.

[98] J. Meléndez and B. Barbuy. Both accurate and precise gf-values for Fe II lines. *A&A*, 497:611–617, April 2009.

[99] J. Meléndez, M. Bergemann, J. G. Cohen, M. Endl, A. I. Karakas, I. Ramírez, W. D. Cochran, D. Yong, P. J. MacQueen, C. Kobayashi, and M. Asplund. The remarkable solar twin HIP 56948: a prime target in the quest for other Earths. *A&A*, 543:A29, July 2012.

[100] J. Meléndez, K. Dodds-Eden, and J. A. Robles. HD 98618: A Star Closely Resembling Our Sun. *ApJ*, 641:L133–L136, April 2006.

[101] J. Meléndez and I. Ramírez. HIP 56948: A Solar Twin with a Low Lithium Abundance. *ApJ*, 669:L89–L92, November 2007.

[102] J. Meléndez, I. Ramírez, L. Casagrande, M. Asplund, B. Gustafsson, D. Yong, J. D. Do Nascimento, M. Castro, and M. Bazot. The solar, exoplanet and cosmological lithium problems. *Ap&SS*, 328:193–200, July 2010.

[103] G. Meynet and A. Maeder. Stellar evolution with rotation. I. The computational method and the inhibiting effect of the μ-gradient. *A&A*, 321:465–476, May 1997.

[104] G. Meynet, J.-C. Mermilliod, and A. Maeder. New dating of galactic open clusters. *A&AS*, 98:477–504, May 1993.

[105] G. Michaud. The lithium abundance gap in the Hyades F stars - The signature of diffusion. *ApJ*, 302:650–655, March 1986.

[106] A. Miglio and J. Montalbán. Constraining fundamental stellar parameters using seismology. Application to α Centauri AB. *A&A*, 441:615–629, October 2005.

[107] L. A. Milone and A. A. E. Milone. Log (gf) for singly-ionized elements of the iron group. *Ap&SS*, 107:303–312, December 1984.

[108] P. J. Mohr, Taylor, and D. B. B. N., Newell. . *Rev. Mod. Phys.*, pages 633–730, 2008.

[109] P. Molaro, A. Bressan, M. Barbieri, P. Marigo, and S. Zaggia. Pre-MS depletion, accretion and primordial ^{7}Li. *Memorie della Societa Astronomica Italiana Supplementi*, 22:233, 2012.

[110] J. Montalbán and E. Schatzman. Mixing by internal waves. III. Li and Be abundance dependence on spectral type, age and rotation. *A&A*, 354:943–959, February 2000.

[111] T. Montmerle, J.-C. Augereau, M. Chaussidon, M. Gounelle, B. Marty, and A. Morbidelli. From Suns to Life: A Chronological Approach to the History of Life on Earth 3. Solar System Formation and Early Evolution: the First 100 Million Years. *Earth Moon and Planets*, 98:39–95, June 2006.

[112] H. Nagaoka and T. Mishima. A Combination of a Concave Grating with a Lummer-Gehrcke Plate or an Echelon Grating for Examining Fine Structure of Spectral Lines. *ApJ*, 57:92, March 1923.

[113] C. Neuforge-Verheecke and P. Magain. Spectroscopic analysis of the Alpha Centauri system. *A&A*, 328:261–268, December 1997.

[114] V. Neves, N. C. Santos, S. G. Sousa, A. C. M. Correia, and G. Israelian. Chemical abundances of 451 stars (Neves+, 2009). *VizieR Online Data Catalog*, 349:70563–+, May 2009.

[115] P. E. Nissen. Chemical Evolution of the Galaxy. In C. Turon, K. S. O'Flaherty, and M. A. C. Perryman, editors, *The Three-Dimensional Universe with Gaia*, volume 576 of *ESA Special Publication*, page 121, January 2005.

[116] P. E. Nissen. Chemical abundances as population tracers. *ArXiv e-prints*, September 2011.

[117] P. E. Nissen and W. J. Schuster. Chemical composition of halo and disk stars with overlapping metallicities. *A&A*, 326:751–762, October 1997.

[118] K. Nomoto, T. Moriya, N. Tominaga, and T. Suzuki. Explosive Nucleosynthesis in Luminous Hypernovae and Faint Supernovae. In D. J. Whalen, V. Bromm, and N. Yoshida, editors, *American Institute of Physics Conference Series*, volume 1294 of *American Institute of Physics Conference Series*, pages 76–83, November 2010.

[119] B. Nordström, M. Mayor, J. Andersen, J. Holmberg, F. Pont, B. R. Jørgensen, E. H. Olsen, S. Udry, and et al.,. The Geneva-Copenhagen survey of the Solar

neighbourhood. Ages, metallicities, and kinematic properties of ~ 14 000 F and G dwarfs. *A&A*, 418:989–1019, May 2004.

[120] L. Pasquini, K. Biazzo, P. Bonifacio, S. Randich, and L. R. Bedin. Solar twins in M 67. *A&A*, 489:677–684, October 2008.

[121] M. Pinsonneault. Mixing in Stars. *ARA&A*, 35:557–605, 1997.

[122] N. Pizzolato, A. Maggio, G. Micela, S. Sciortino, and P. Ventura. The stellar activity-rotation relationship revisited: Dependence of saturated and non-saturated X-ray emission regimes on stellar mass for late-type dwarfs. *A&A*, 397:147–157, January 2003.

[123] G. F. Porto de Mello and L. da Silva. HR 6060: The Closest Ever Solar Twin? *ApJ*, 482:L89, June 1997.

[124] G. F. Porto de Mello, W. Lyra, and G. R. Keller. The Alpha Centauri binary system. Atmospheric parameters and element abundances. *A&A*, 488:653–666, September 2008.

[125] D. Pourbaix, D. Nidever, C. McCarthy, R. P. Butler, C. G. Tinney, G. W. Marcy, H. R. A. Jones, A. J. Penny, B. D. Carter, F. Bouchy, F. Pepe, J. B. Hearnshaw, J. Skuljan, D. Ramm, and D. Kent. Constraining the difference in convective blueshift between the components of alpha Centauri with precise radial velocities. *A&A*, 386:280–285, April 2002.

[126] N. Prantzos. Production and evolution of Li, Be, and B isotopes in the Galaxy. *A&A*, 542:A67, June 2012.

[127] William H. Press, Saul A. Teukolsky, William T. Vetterling, and Brian P. Flannery. *Numerical Recipes 3rd Edition: The Art of Scientific Computing*. Cambridge University Press, New York, NY, USA, 3 edition, 2007.

[128] A. J. J. Raassen and P. H. M. Uylings. On the determination of the solar iron abundance using Fe II lines. *A&A*, 340:300–304, December 1998.

[129] I. Ramírez, C. Allende Prieto, and D. L. Lambert. Oxygen abundances in nearby stars. Clues to the formation and evolution of the Galactic disk. *A&A*, 465:271–289, April 2007.

[130] I. Ramírez and J. Meléndez. The Effective Temperature Scale of FGK Stars. I. Determination of Temperatures and Angular Diameters with the Infrared Flux Method. *ApJ*, 626:446–464, June 2005.

[131] I. Ramírez, J. Meléndez, and M. Asplund. Accurate abundance patterns of solar twins and analogs. Does the anomalous solar chemical composition come from planet formation? *A&A*, 508:L17–L20, December 2009.

[132] I. Ramírez, J. Meléndez, D. Cornejo, I. U. Roederer, and J. R. Fish. Elemental Abundance Differences in the 16 Cygni Binary System: A Signature of Gas Giant Planet Formation? *ApJ*, 740:76, October 2011.

[133] S. Randich, R. Gratton, R. Pallavicini, L. Pasquini, and E. Carretta. Lithium in population I subgiants. *A&A*, 348:487–500, August 1999.

[134] S. Randich, R. Pallavicini, G. Meola, J. R. Stauffer, and S. C. Balachandran. Membership, lithium, and metallicity in the young open clusters ¡ASTROBJ¿IC 2602¡/ASTROBJ¿ and ¡ASTROBJ¿IC 2391¡/ASTROBJ¿: Enlarging the sample. *A&A*, 372:862–878, June 2001.

[135] R. Rebolo, J. E. Beckman, L. Crivellari, F. Castelli, and B. Foing. Lithium abundances and Li-7/Li-6 ratios in late-type population I field dwarfs. *A&A*, 166:195–203, September 1986.

[136] B. E. Reddy, D. L. Lambert, and C. Allende Prieto. Elemental abundances for 176 stars (Reddy+, 2006). *VizieR Online Data Catalog*, 736:71329, September 2006.

[137] B. E. Reddy, D. L. Lambert, C. Laws, G. Gonzalez, and K. Covey. A search for ^{6}Li in stars with planets. *MNRAS*, 335:1005–1016, October 2002.

[138] B. E. Reddy, J. Tomkin, D. L. Lambert, and C. Allende Prieto. The chemical compositions of Galactic disc F and G dwarfs. *MNRAS*, 340:304–340, March 2003.

[139] J. A. Robles, C. H. Lineweaver, D. Grether, C. Flynn, C. A. Egan, M. B. Pracy, J. Holmberg, and E. Gardner. A Comprehensive Comparison of the Sun to Other Stars: Searching for Self-Selection Effects. *ApJ*, 684:691–706, September 2008.

[140] H. J. Rocha-Pinto and W. J. Maciel. Metallicity effects on the chromospheric activity-age relation for late-type dwarfs. *MNRAS*, 298:332–346, August 1998.

[141] H. N. Russel. . *ApJ*, 70:11, 1929.

[142] S. G. Ryan. The host stars of extrasolar planets have normal lithium abundances. *MNRAS*, 316:L35–L39, August 2000.

[143] K. Sadakane, M. Ohkubo, Y. Takeda, B. Sato, E. Kambe, and W. Aoki. Abundance Analyses of 12 Parent Stars of Extrasolar Planets Observed with the SUBARU/HDS. *PASJ*, 54:911–931, December 2002.

[144] C. Saffe, M. Gómez, and C. Chavero. On the ages of exoplanet host stars. *A&A*, 443:609–626, November 2005.

[145] A. Sandage. The Ages of M67, NGC 188, M3, M5, and M13 According to Hoyle's 1959 Models. *ApJ*, 135:349, March 1962.

[146] N. C. Santos, G. Israelian, and M. Mayor. Spectroscopic [Fe/H] for 98 extrasolar planet-host stars. Exploring the probability of planet formation. *A&A*, 415:1153–1166, March 2004.

[147] N. C. Santos, G. Israelian, M. Mayor, J. P. Bento, P. C. Almeida, S. G. Sousa, and A. Ecuvillon. Spectroscopic metallicities for planet-host stars: Extending the samples. *A&A*, 437:1127–1133, July 2005.

[148] L. Sbordone. Kurucz's codes under GNU-Linux. *Memorie della Societa Astronomica Italiana Supplementi*, 8:61, 2005.

[149] L. Sbordone, P. Bonifacio, E. Caffau, H.-G. Ludwig, N. T. Behara, J. I. González Hernández, M. Steffen, R. Cayrel, B. Freytag, C. van't Veer, P. Molaro, B. Plez, T. Sivarani, M. Spite, F. Spite, T. C. Beers, N. Christlieb, P. François, and V. Hill. The metal-poor end of the Spite plateau. I. Stellar parameters, metallicities, and lithium abundances. *A&A*, 522:A26, November 2010.

[150] L. Sbordone, P. Bonifacio, and F. Castelli. ATLAS 9 and ATLAS 12 under GNU-Linux. In F. Kupka, I. Roxburgh, and K. Chan, editors, *IAU Symposium*, volume 239 of *IAU Symposium*, pages 71–73, May 2007.

[151] R. Schnabel, M. Schultz-Johanning, and M. Kock. Fe II lifetimes and transition probabilities. *A&A*, 414:1169–1176, February 2004.

[152] S. Seager. The search for extrasolar Earth-like planets. *Earth and Planetary Science Letters*, 208:113–124, March 2003.

[153] S. Seager. Exoplanet atmospheres: A theoretical outlook. In A. Sozzetti, M. G. Lattanzi, and A. P. Boss, editors, *IAU Symposium*, volume 276 of *IAU Symposium*, pages 198–207, November 2011.

[154] P. Sestito and S. Randich. Time scales of Li evolution: a homogeneous analysis of open clusters from ZAMS to late-MS. *A&A*, 442:615–627, November 2005.

[155] P. Sestito, S. Randich, and R. Pallavicini. Lithium evolution in intermediate age and old open clusters: NGC 752 revisited. *A&A*, 426:809–817, November 2004.

[156] A. Skumanich. Time Scales for CA II Emission Decay, Rotational Braking, and Lithium Depletion. *ApJ*, 171:565, February 1972.

[157] G. Smith, B. Edvardsson, and U. Frisk. Non-resonance lines of neutral calcium in the spectra of the Alpha Centauri binary system. *A&A*, 165:126–134, September 1986.

[158] C. A. Sneden. *Carbon and Nitrogen Abundances in Metal-Poor Stars.* PhD thesis, 1973.

[159] D. R. Soderblom. Rotational studies of late-type stars. II - Ages of solar-type stars and the rotational history of the sun. *ApJS*, 53:1–15, September 1983.

[160] D. R. Soderblom. The temperatures of Alpha Centauri A and B. *A&A*, 158:273–+, April 1986.

[161] D. R. Soderblom, S. B. Fedele, B. F. Jones, J. R. Stauffer, and C. F. Prosser. The evolution of the lithium abundances of solar-type stars. IV - Praesepe. *AJ*, 106:1080–1086, September 1993.

[162] D. R. Soderblom, J. R. King, L. Siess, B. F. Jones, and D. Fischer. Evolution Of The Lithium Abundances Of Solar-Type Stars. IX. High-Resolution Spectroscopy of Low-Mass Stars in NGC 2264. *AJ*, 118:1301–1314, September 1999.

[163] C. Soubiran and A. Triaud. The Top Ten solar analogs in the ELODIE library. *A&A*, 418:1089–1100, May 2004.

[164] S. G. Sousa. ARES: Automatic Routine for line Equivalent widths in stellar Spectra. *Astrophysics Source Code Library*, page 5009, May 2012.

[165] S. G. Sousa, N. C. Santos, M. Mayor, S. Udry, L. Casagrande, G. Israelian, F. Pepe, D. Queloz, and et al.,. Spectroscopic parameters for 451 stars in the HARPS GTO planet search program. Stellar [Fe/H] and the frequency of exo-Neptunes. *A&A*, 487:373–381, August 2008.

[166] F. Spite and M. Spite. Abundance of lithium in unevolved halo stars and old disk stars - Interpretation and consequences. *A&A*, 115:357–366, November 1982.

[167] M. Spite and F. Spite. Li isotopes in metal-poor halo dwarfs: a more and more complicated story. In C. Charbonnel, M. Tosi, F. Primas, and C. Chiappini, editors, *IAU Symposium*, volume 268 of *IAU Symposium*, pages 201–210, April 2010.

[168] M. Steffen. A model atmosphere analysis of the F5 IV-V subgiant Procyon. *A&AS*, 59:403–427, March 1985.

[169] G. Steigman. Primordial Nucleosynthesis in the Precision Cosmology Era. *Annual Review of Nuclear and Particle Science*, 57:463–491, November 2007.

[170] G. Steigman. Primordial Nucleosynthesis After WMAP. In K. Cunha, M. Spite, and B. Barbuy, editors, *IAU Symposium*, volume 265 of *IAU Symposium*, pages 15–22, March 2010.

[171] H. E. Suess and H. C. Urey. Abundances of the Elements. *Reviews of Modern Physics*, 28:53–74, January 1956.

[172] F. J. Swenson and J. Faulkner. Lithium dilution through main-sequence mass loss. *ApJ*, 395:654–674, August 1992.

[173] Y. Takeda, S. Honda, S. Kawanomoto, H. Ando, and T. Sakurai. Behavior of Li abundances in solar-analog stars II. Evidence of the connection with rotation and stellar activity. *ArXiv e-prints*, March 2010.

[174] Y. Takeda and S. Kawanomoto. Lithium Abundances of F-, G-, and K-Type Stars: Profile-Fitting Analysis of the Li I 6708 Doublet. *PASJ*, 57:45–63, February 2005.

[175] Y. Takeda, S. Kawanomoto, S. Honda, H. Ando, and T. Sakurai. Behavior of Li abundances in solar-analog stars. Evidence for line-width dependence. *A&A*, 468:663–677, June 2007.

[176] Y. Takeda and A. Tajitsu. High-Dispersion Spectroscopic Study of Solar Twins: HIP 56948, HIP 79672, and HIP 100963. *PASJ*, 61:471–, June 2009.

[177] S. Talon. Rotational Transport Processes (Invited Review). In A. Maeder and P. Eenens, editors, *Stellar Rotation*, volume 215 of *IAU Symposium*, page 336, June 2004.

[178] S. Talon and C. Charbonnel. Angular momentum transport by internal gravity waves. I - Pop I main sequence stars. *A&A*, 405:1025–1032, July 2003.

[179] S. Talon and C. Charbonnel. Hydrodynamical stellar models including rotation, internal gravity waves, and atomic diffusion. I. Formalism and tests on Pop I dwarfs. *A&A*, 440:981–994, September 2005.

[180] S. Talon, P. Kumar, and J.-P. Zahn. Angular Momentum Extraction by Gravity Waves in the Sun. *ApJ*, 574:L175–L178, August 2002.

[181] F. X. Timmes, S. E. Woosley, and T. A. Weaver. Galactic chemical evolution: Hydrogen through zinc. *ApJS*, 98:617–658, June 1995.

[182] G. Torres, J. Andersen, and A. Giménez. Accurate masses and radii of normal stars: modern results and applications. *A&A Rev.*, 18:67–126, February 2010.

[183] C. Travaglio, S. Randich, D. Galli, J. Lattanzio, L. M. Elliott, M. Forestini, and F. Ferrini. Galactic Chemical Evolution of Lithium: Interplay between Stellar Sources. *ApJ*, 559:909–924, October 2001.

[184] J. A. Valenti and D. A. Fischer. Spectroscopic Properties of Cool Stars (SPOCS). I. 1040 F, G, and K Dwarfs from Keck, Lick, and AAT Planet Search Programs. *ApJS*, 159:141–166, July 2005.

[185] I. M. Vardavas. The dependence of the Rossby number and XUV-Lyα emission flux with age for solar-like G-type stars. *MNRAS*, 363:L51–L55, October 2005.

[186] G. Wallerstein, G. H. Herbig, and P. S. Conti. Observations of the Lithium Content of Main-Sequence Stars in the Hyades. *ApJ*, 141:610, February 1965.

[187] B. Warner. Absolute oscillator strengths for once-ionized elements of the iron group. *MmRAS*, 70:165, 1967.

[188] M. M. Woolfson. The Solar - Origin and Evolution. *QJRAS*, 34:1–20, March 1993.

[189] J. T. Wright, G. W. Marcy, R. P. Butler, and S. S. Vogt. Chromospheric Ca II Emission in Nearby F, G, K, and M Stars. *ApJS*, 152:261–295, June 2004.

[190] S. Yi, P. Demarque, Y.-C. Kim, Y.-W. Lee, C. H. Ree, T. Lejeune, and S. Barnes. Toward Better Age Estimates for Stellar Populations: The Y^2 Isochrones for Solar Mixture. *ApJS*, 136:417–437, October 2001.

[191] J.-P. Zahn. Circulation and turbulence in rotating stars. *A&A*, 265:115–132, November 1992.

[192] J.-P. Zahn. Modeling Stellar Interiors with Rotational Mixing. In C. W. Straka, Y. Lebreton, and M. J. P. F. G. Monteiro, editors, *EAS Publications Series*, volume 26 of *EAS Publications Series*, pages 49–64, 2007.